Quantitative experimental modeling of fragmentation during phreatomagmatic and phreatic eruptions

by

Øystein Thordén Haug

THESIS

for the degree of

MASTER OF SCIENCE

(Physics of geological processes, Department of Physics)

Faculty of Mathematics and Natural Sciences
University of Oslo

February 2012

0.1 Acknowledgment

A great thank you to my supervisors, Olivier Galland and Galen Gisler. Thank you for the inspiration and the frustration, the structure and the break down. Thank you very much for not slamming the door of your offices in my face when I, for the 11th time that day, knocked on it. Thank you for giving me the room to think and the suggestions to think in the correct direction.

I owe a great thanks to many people at PGP, thank you Olav for helping me with the experiments, thank you Luiza for helping me with the statistics, thank you Karen for answering questions of frustration, thank you Jacqueline, Ole Ivar, Kristin and Even for helping me write and thank you Jørgen for helping me with Latex.

Without the help and support from my girlfriend, Elvira, I am certain I would still be without a word to write. Your annoying questions forces me to understand, and for that I am grateful. Thank you for pushing me when I need it, and helping me to relax when I need that.

On the social arena there are many people I have to thank, all the master student at PGP (Kristin, Kristin, Håkon, Even, Liene, Håvard, Celine, Kerstin, Derya, Kristin and Hedda). Thank you for making my studies a fun experience and for making me look forward to each day. Finally, I have to thank my friends Olav, Stefan, Kjetil, Jon Kjetil, Sindre, Hans Kjetil, Halvor and Marie. Thank you for dragging me from my studies and showing me the world outside of science.

Contents

Chapter 1

Introduction - Geological setting

Volcanic eruptions can be explosive or non-explosive. Where the non-explosive are more calm and not that damaging (less abrupt) the explosive are violent and can cause great damage. The focus in this work is on the explosive volcanic eruptions.

There are different types of volcanic eruptions; magmatic, phreatomagmatic and phreatic eruptions. Magmatic eruptions can be both explosive and non-explosive whereas phreatic and phreatomagmatic eruptions are always explosive.

Explosive volcanic eruptions create distinct geological structures. Examples of these are piercement structures and craters. In this study I take a closer look at maars and diatremes. A maar is a crater caused by a phreatomagmatic eruption. The crater are usually wide compared to the depth [Browne and Lawless, 2001]. A diatreme is a piercement structure that is filled with brecciated rock. Diatremes are found under maars [Browne and Lawless, 2001]. In figure 1.1 a sketch of the relationship between maars and diatremes is shown.

Magmatic eruptions are volcanic eruptions where magma rises to the surface. The behavior of a magmatic eruption depends on the chemical composition of the magma. In particular, the explosivity of magmatic eruptions is mainly determined by the amount of volatiles within the magma and the viscosity of the magma. The reason for this is that an explosive magmatic eruption is caused by rapid nucleation and growth of bubbles within the magma. At high pressure, i.e. far below the surface, the volatiles are dis-

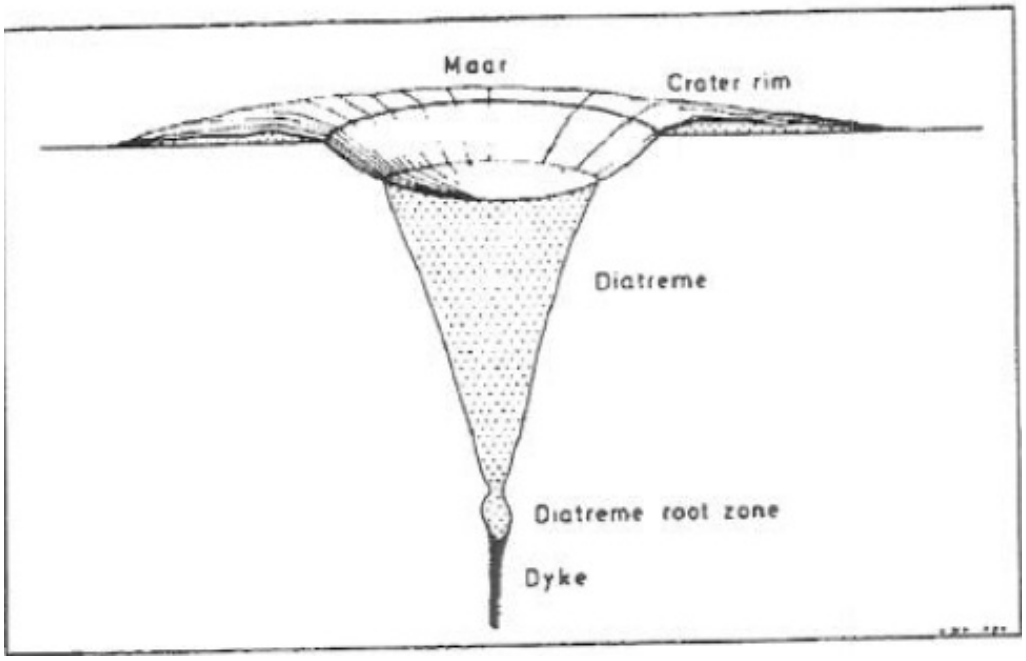

Figure 1.1: *Schematic representation of the relationship between maars and diatremes [Lorenz, 1985]*

solved within the magma. As the magma rises to the surface, the pressure decreases. The decrease in pressure causes the volatiles to be released from the magma and nucleate gas bubbles. The bubbles continue to grow as the pressure decreases. At a certain pressure the bubbles cause fragmentation and ejection of the magma [Winter, 2001]. An illustration from Kaminski and Jaupart [1998] of this process is given in figure 1.2

Phreatomagmatic eruptions are explosive eruptions due to violent interaction between magma and water, where the water can for example be ground water or a shallow lake. This violent interaction causes fragmentation of both the magma and the host rock. Unlike magmatic eruptions, phreatomagmatic eruptions are observed for many different types of chemical composition of magma. This means that a phreatomagmatic eruption is independent of the chemical composition of the magma [Lorenz, 1985]. A phreatomagmatic eruption is a result of the thermal energy of the magma being transformed into mechanical energy by rapid water vaporization [Lorenz, 1985, Zimanowski et al., 1997b].

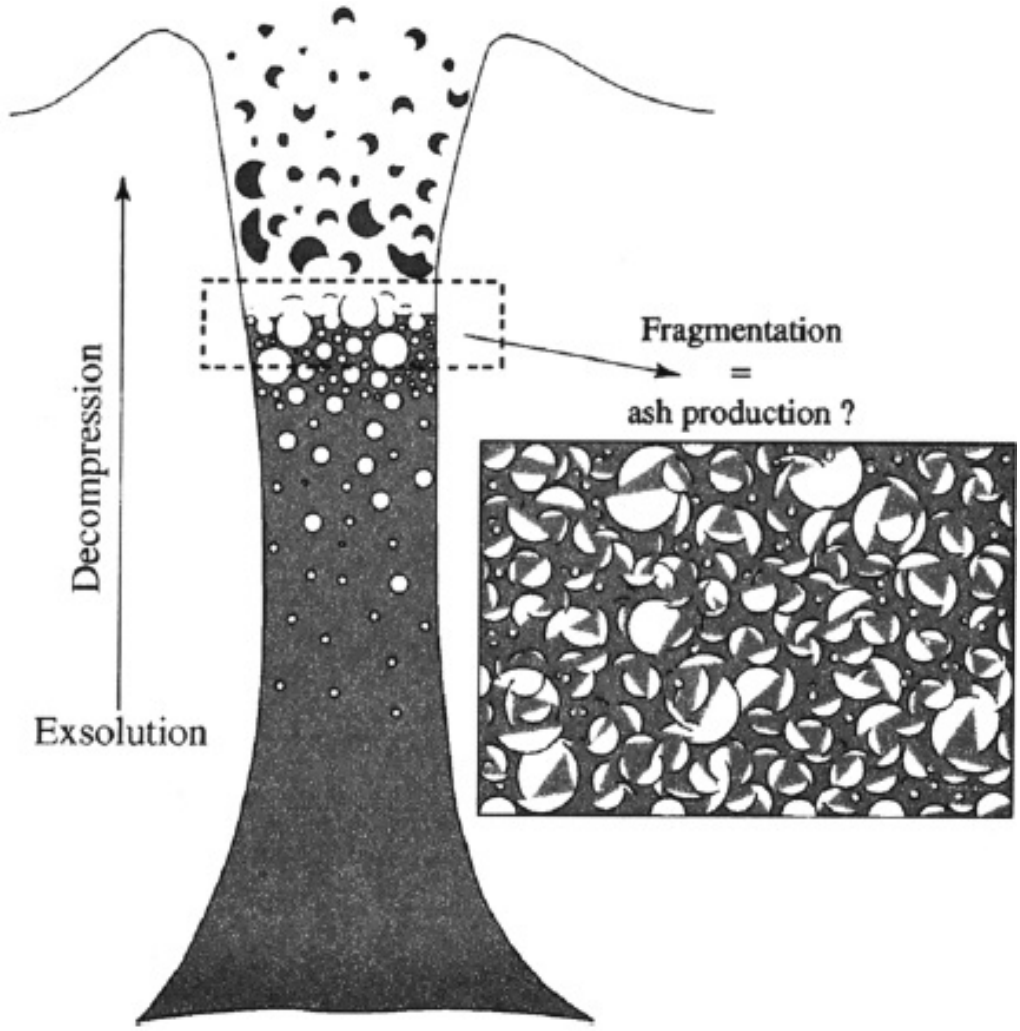

Figure 1.2: *Schematic representation of the main processes of fragmenting magma. The pressure decreases as the magma rises, causing the volatiles in the magma to be released and nucleate bubbles. The bubbles continue to grow until they eventually fragment the magma. [Kaminski and Jaupart, 1998]*

A phreatic eruption is due to a temperature anomaly in a water rich environment. For example, in a phreatic eruption there can be thermal contact between magma and water, causing an explosion. It can be difficult to distinguish between a phreatic and a phreatomagmatic eruption. The difference is that in a phreatic eruption only the host rock or the overburden is fragmented and ejected and not any juvenile material. [Browne and Lawless, 2001]. Phreatic eruptions are sometimes called hydrothermal eruptions.

Explosive volcanoes are in general known to produce large amount of very fine particles ($< 64\mu m$), i.e fine ash particles. The production of fine ash requires a lot of energy and is therefore seen as a fingerprint of explosive volcanoes [Zimanowski et al., 2003].

The fact that ash is produced means that the magma and/or the host rock has been fragmented. Fragmentation is the process where an entity is separated into smaller pieces. This is a very common process in nature and in our daily lives. Fragmentation occurs on all length scales, from fission of atoms, to a glass dropped on the floor, to supernovas in space [Åström, 2006]. Since fragmentation is such a common process it has been studied in several scientific communities, such as physics and geology, and a rich literature exists. However, there are still unanswered questions, for example, what are the physics that govern fragmentation processes? And how does fragmentation occur through time?

Fragmentation occurs when a material is exposed to an external loading exceeding the strength of the material. The loading causes fractures to propagate that separate the material into fragments.

A general feature of fragmentation is that the different pieces are not of equal size, and often the sizes of the fragments span over several orders of magnitude. Statistics is therefore a helpful tool to study processes that involve fragmentation. Statistics help us to quantify and interpret the process of fragmentation.

There are two types of fragmentation; hydrodynamic fragmentation (ductile-like) and brittle fragmentation (solid-like). Zimanowski et al. [2003] considered the amount of energy needed to fragment magma both by hydrodynamic fragmentation and brittle fragmentation. They showed that the production of fine ash would require an infinite amount of energy if the fragmentation is hydrodynamic. The production of fine ash therefore requires that the fragmentation in explosive volcanism is, at least partly, a brittle process.

The main focus in this master thesis is on brittle materials. A brittle material is, as defined by Åström [2006], a material that is linearly elastic up to a certain strain. If the material is exposed to strain above this level, failure occurs. The break up is then rapid and irreversible.

In a study of explosive volcanism there are several observables that can be considered. I focus on the morphologies and on the fragmentation products, and the physical laws by which they are governed. To be able to study this I need to know how fragmentation in explosive volcanism occurs.

Volcanoes are complex phenomena, with for instance multiple phases. To study them it is necessary to do simplifications, which make experiments a suitable approach for studying volcanoes.

In this thesis I first give a review of the literature about explosive volcanism and fragmentation. Then I present an experimental setup that models fragmentation during explosive volcanism. Afterwards, the results from the experiments are presented and discussed.

Chapter 2

Former work

When investigating a phenomenon a desirable way to study it is to directly measure and monitor the process when it occurs. For explosive volcanism, however, direct observation is difficult. There are two reasons for this. First of all, the processes are so violent that it is practically impossible observe them directly. The second reason is that most of the processes occur under the surface and are therefore not possible to observe.

Since we cannot observe the processes of explosive volcanism directly we need to use other approaches. To study explosive volcanism one can do field work, experiments, simulations or theoretical work.

2.1 Field work

One approach to study fragmentation in explosive volcanism is to observe and measure the craters, piercement structures and the volcanic deposits, i.e. the products of fragmentation. In this section I present field observations of some features of volcanic explosions, such as maars, diatremes and volcanic deposits.

Maars and diatrems

Maars are collapse craters that are wide compared to their depth, i.e. wide and shallow [Browne and Lawless, 2001]. The pyroclastic ejecta surrounding maars consist of a mixture of juvenile origin with low vesicularity and a large part of host rock material with a large amount of fine fragment size. These

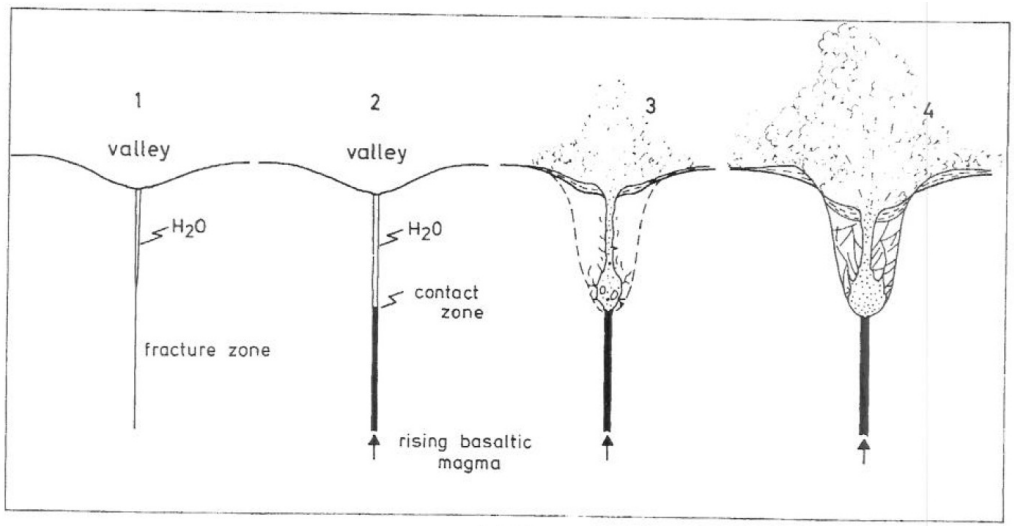

Figure 2.1: *Sketch of a model of the formation of a maar. 1. A zone of structural weakness is hydraulically active in near surface levels. 2. Rising magma enters the structural weakness and comes in contact with the water. 3. A violent interaction between the magma and water causes a phreatomagmatic eruption. This fragments both the magma and the host rock and some is ejected to the surface. 4. The excavation of the explosion has left the side-walls unstable and they collapse into the crater. This leaves a wide and shallow crater at the top. (Figure and explanation from Lorenz [1985])*

observations suggest that maars are of phreatomagmatic origin [Lorenz, 1985]. This means that they are created due to an explosion caused by an interaction between magma and external water. A sketch of a model by Lorenz [1985] of the formation of a maar is shown in figure 2.1.

Diatremes are cone-shaped piercement structures underlying a maar. This indicate that diatreme are of phreatomagmatic origin. They are filled with breccia. A schematic drawing of a maar-diatreme volcano is shown in figure 2.2.

Other eruptions may also create piercement structures. In figure 2.3a a sketch of the piercement structure from a phreatic eruption, called a hydrothermal vent, is shown. In figure 2.3b a sketch of a kimberlite pipe (which is magmatic) is shown. Even though the processes that lead to the piercement structures in figure 2.2 and figure 2.3 are created by different

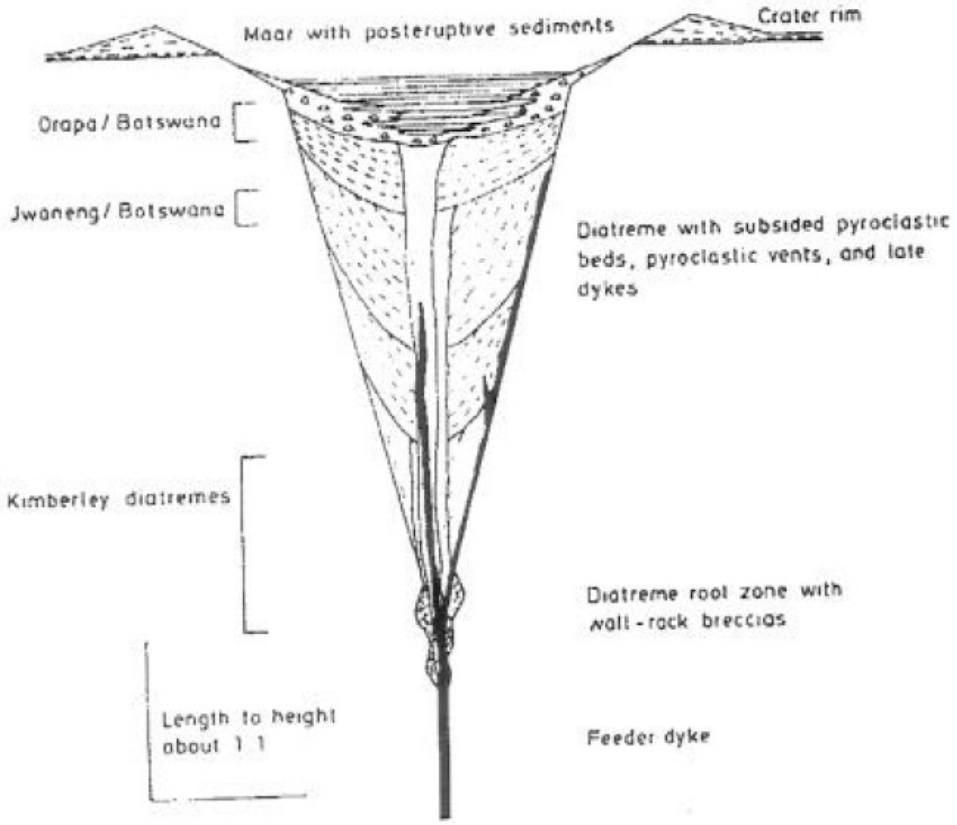

Figure 2.2: *Schematic drawing of a characteristic maar-diatreme volcano. This drawing is pieced together from observations at different localities where the respective pieces of the diatreme are visible. Figure from Lorenz [1985].*

processes, they are remarkably similar in shape.

Fragment size distributions

The volcanic deposits are the fragments ejected from a volcanic eruption. A common way to study the volcanic deposits is to measure the distribution of sizes of the fragments. The fragment sizes from volcanic deposits are usually found by the method of sieving and are given in ϕ units where

$$\phi = -\frac{log(d)}{log(2)} \tag{2.1}$$

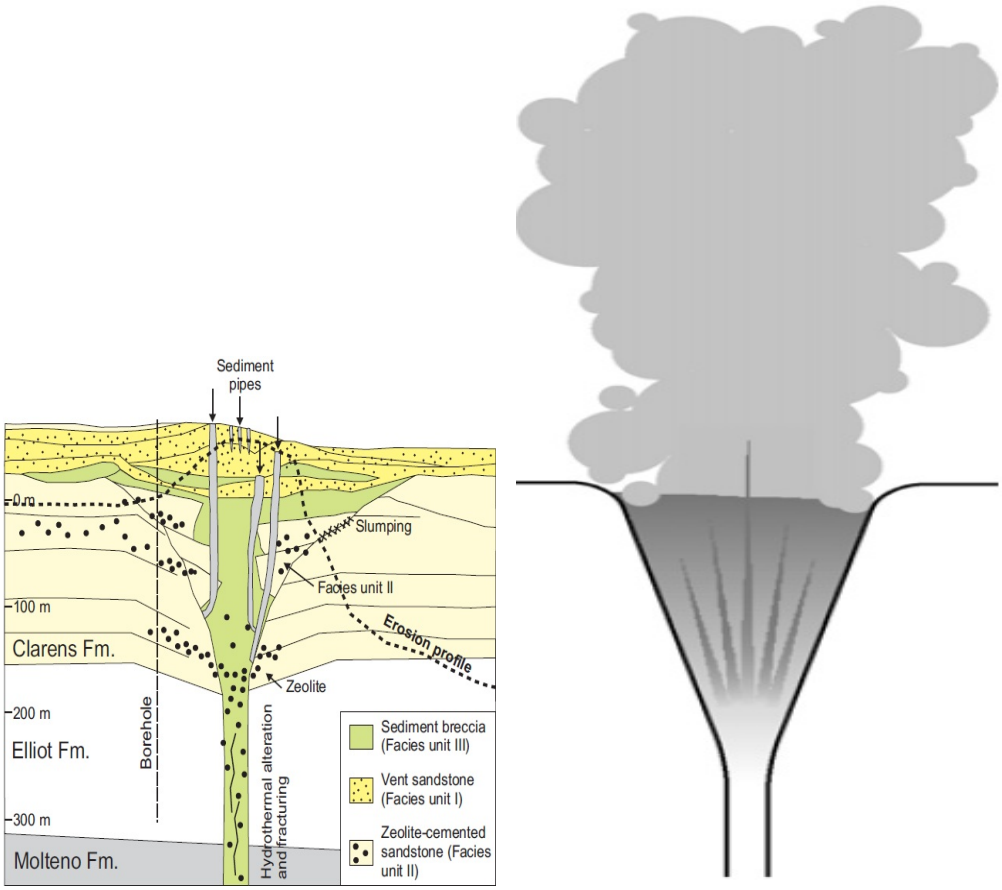

(a) Hydrothermal vent **(b)** Kimberlite pipe

Figure 2.3: *(a) Sketch of hydrothermal vent. Figure from Svensen et al. [2006]. (b) Sketch of a kimberlite pipe. Figure from Sparks et al. [2006].*

where d is the maximum length of the fragments in millimeter, [Kaminski and Jaupart, 1998]. This means that ϕ represents the maximum size of fragments found in one sieve. The fragment sizes are often presented in a fragment size distribution. A fragment size distribution is the cumulative frequency of the sizes of the fragments. Some examples of fragment size distributions for volcanic deposits are given in figure 2.4.

The advantage of displaying the sizes of fragments in a cumulative plot is that it conveniently displays the data within one figure. It also makes it possible to compare the number of small fragments with the number of large ones.

It is common to fit some function to the data points in the fragment size distribution. This makes it easier to compare different fragment size distributions. In the fragment size distributions given in figure 2.4 the data points are plotted in a log-log plot and a line is fitted to the log-log data points, i.e. a power-law distribution is fitted to the data. For power-law distributions the parameter of interest is the slope of the line, D. This is because D contains information about the ratio between small fragments and large fragments. That is, if there are many small fragments compared to large fragments D has a higher value than for data-sets that consists of many large fragments compared to small fragments.

In general there are three distributions that are commonly used for fragmentation processes. These are power-law, log-normal and exponential distributions. Explosive volcanism generally have fragment size distributions that show close similarity with power-law distributions [Kaminski and Jaupart, 1998], however, all three distributions have been used to study volcanic deposits [Wohletz et al., 1989].

A list of D-values for different volcanic eruptions is given in Kaminski and Jaupart [1998]. These values are almost always above 3. A D-value above 3 was for many years seen as a surprise since it was believed that a 3-dimensional fragmentation process should produce a D-value less than 3, [Turcotte, 1986]. Kaminski and Jaupart suggest that D-value above 3 is possible if there is more than one sequence of fragmentation. They suggest that there is a "primary" fragmentation with a $D \approx 2.6$ and then a secondary fragmentation (similar to grinding) that causes the D-value to increase.

It is important to notice that the fragment size distributions presented in figure 2.4 are from magmatic eruptions.

A study of hydrothermal breccias in veins or ores was performed by

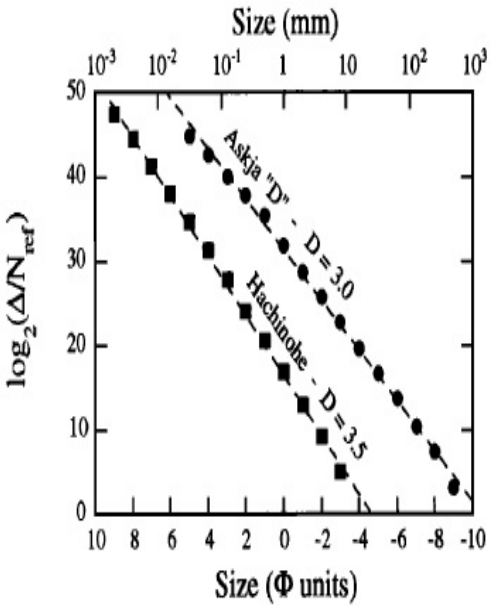

(a) Askja, Iceland and Hachinohe, Japan

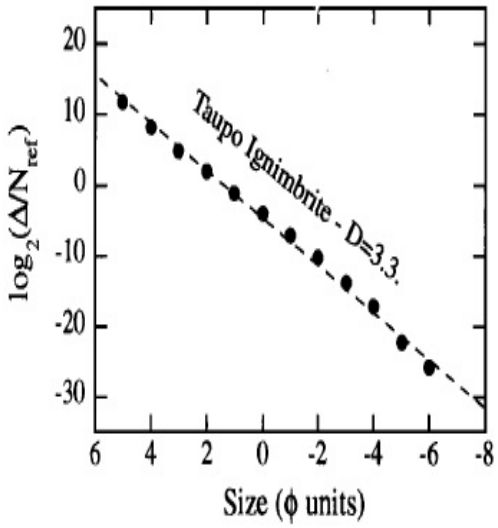

(b) Taupo Ignimbrite, New Zealand

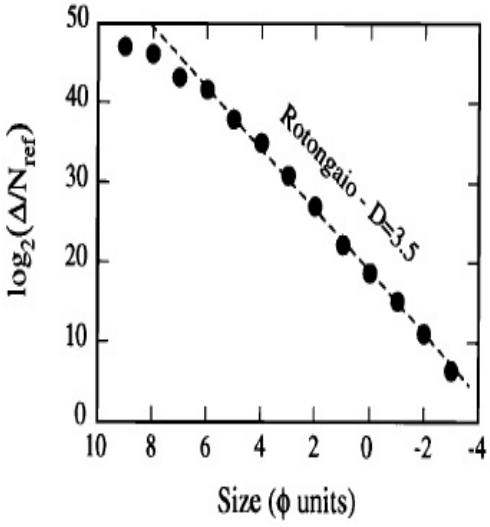

(c) Rotongaio

Figure 2.4: *Fragment size distributions from volcanic deposits from different volcanoes (magmatic). Data collected by sieving. Figure from Kaminski and Jaupart [1998].*

Jébrak [1997]. He studied a whole range of different hydrothermal systems (From less to highly explosive), and pointed at the fragment size distribution as one of four parameters (morphology, fragments size distribution, fabric and dilatation ratios) for describing breccia. It was shown that the D-value can be observed to have higher value for higher energy brecciation than for lower energy. Where phreatic, which is highly energetic, have a very high D-value (between 4 and 6), and lower energy brecciation have a D-value closer to 1.

The spread in D-values, pointed out by Jébrak [1997], shows that what controls it is far from understood. It is suggested that the value depends on the amount of energy, and that it varies from system to system. This might also suggest that it depends on the processes involved, but what are these processes?

What do field observations tell us?

Field observations are purely descriptive and only the final products are available for observation. This means that field observations are not able to tell us anything about the mechanisms and dynamics during an eruption. Field observations can, however, tell us that:

- Maars and diatremes are structures related to phreatomagmatic eruptions.
- There is a remarkable resemblance between hydrothermal vents, kimberlite pipes and maars and diatremes.
- Fragment size distributions for volcanic deposits show a close resemblance to power law distributions.
- The D-value of the power law distributions depends on the system and on the amount of energy released by the system.

2.2 Experiments

Experiments are natural processes and do therefore not give unphysical results. However, there are two major sources of errors with an experimental approach. (i) Since experiments are natural processes they also contain

all the complexities of nature and can make interpretation difficult. (ii) Experiments are often a representation of a more complex system (analogue experiments). Even though what happens in an experiment is undoubtedly true and represents nature as is given by the experiment, we can never be certain that the experiments really represent the system that we want to study.

In this section I start by presenting the Molten Fuel Coolant Interaction model, which is a model for the explosion of a phreatomagmatic eruption, and some experiments done to study this model. Afterwards, some experiments on the general features of fragmentation are presented.

Molten Fuel Coolant Interaction experiments

Molten Fuel Coolant Interaction (MFCI) has been suggested as an explanation for the violent interaction of magma and water in a phreatomagmatic eruption. The best way to explain the model of MFCI is by considering MFCI-experiments. There has been several studies where MFCI has been studied experimentally, [Zimanowski et al., 1991, 1997a,b, Grunewald et al., 2007]. The experimental setup used in these studies is very similar. A schematic drawing of the experiments is shown in figure 2.5.

The experiments are performed by melting volcanic rock in a steel crucible. An injection tube is lowered into the melt. Water is injected into the melt and the water and the melt mix. As soon as the water has been injected an insulating vapor layer is established between the melt and the water. The production of such an insulating layer is known as "Leidenfrost phenomenon" [Zimanowski et al., 1991]. This is the same phenomenon that can be observed when a droplet of water is dropped on top of a hot cooking plate. Then the droplet runs around on the plate due to a vapor layer that is produced and removes friction between the water and the plate.

In the MFCI-experiments such an insulating layer separates the water and the melt, and hinders a fast transfer of heat. To create an explosion this layer needs to be removed. This is done by firing an air gun bullet on top of the melt. The impact of the bullet causes a shock wave (of intensity $\sim 8J$) that travels downward in the melt. The impact of the shock wave on the insulating layer causes it to be removed. Shock waves of these intensities are abundant at active volcanic sites, due to pressure pulses of the rising magma or other seismic events. [Zimanowski et al., 1991].

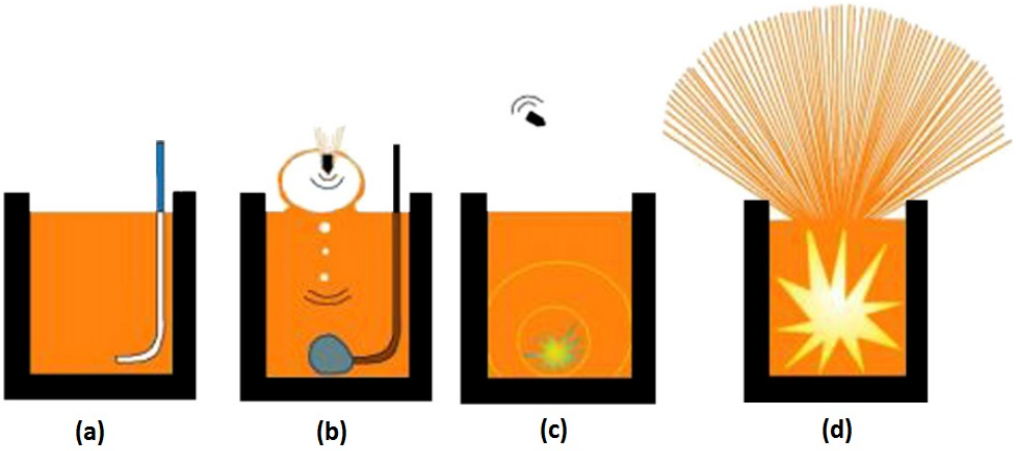

Figure 2.5: *Schematic drawing of a MFCI experiment. (a) A steel crucible is filled with molten volcanic rock. An injection tube is lowered into the melt. (b) Water is injected into the melt and the water and the melt mixes. The injected water is immediately enveloped by an insulating vapor layer that hinders a direct contact between the melt and the water so that no fast heat transfer occurs. An air gun bullet is fired on the top of the melt. When the bullet hits the melt it sends shock waves through the melt. The insulating layer between the melt and the water is destroyed when the shock wave hits it. (c) The destruction of the insulating layer results in direct contact between the melt and the water. This causes a mechanical and thermal coupling between the melt and the water. The melt rapidly cools and contracts and the water rapidly heats and expands. This deformation causes the melt that is coupled with the water to fragment. (d) The superheated water evaporates and therefore expands. This expansion causes the melt in the crucible to be ejected and fragmented. (Explanation and figures from Grunewald et al. [2007])*

With the insulating layer removed, the magma and water couple mechanically and thermally. This causes a rapid cooling and contraction of the melt and a rapid heating and expansion of the water.

The water is now superheated, i.e. water in liquid form with temperature above 373K. Superheated water is not stable under these conditions. The superheated water will therefore suddenly transform into steam. This causes a huge volume change and pressure increase, and material is ejected from the crucible.

Zimanowski et al. [1997b] suggest that there are two events of fragmentation in the MFCI-experiments. The first event is caused by the deformation when the magma cools and contracts and the water heats and expands. The second is when the water is transformed to steam and the melt is ejected from the crucible (see figure 2.5).

After an experimental run the fragments created in the explosion can be collected and presented in a fragment size distribution. The fragment size distribution given in Zimanowski et al. [1991] and Zimanowski et al. [1997b] display two regimes with different slopes of the fitted lines. Zimanowski et al. [1997b] suggest that the two slopes represents the two fragmentation events. A fragment size distribution from Zimanowski et al. [1997b] is given in figure 2.6. The different slopes are suggested to be the result of two different fragmentation processes.

A more detailed description of the physics of MFCI can be found in Büttner and Zimanowski [1998].

The MFCI-model serves as a plausible model for the violent interaction between magma and water. That is, it is able to show that the thermal energy of a melt can cause an explosion and fragmentation of the melt by rapid water vaporization. The processes are, however, very complex and the physics of the experiments are not controlled, so the processes of fragmentation are not trivial to interpret.

Fragmentation experiments

One of the classical studies of fragmentation was performed by Rosin and Rammler [1933] (as described by Åström [2006]). Rosin and Rammler experimented on the crushing of coal, they observed that there were approximately equal masses distributed in equal size intervals. Based on this observation they proposed an empirical size distribution, later defined as the Rosin-Rammler distribution. Their empirical distribution made a huge

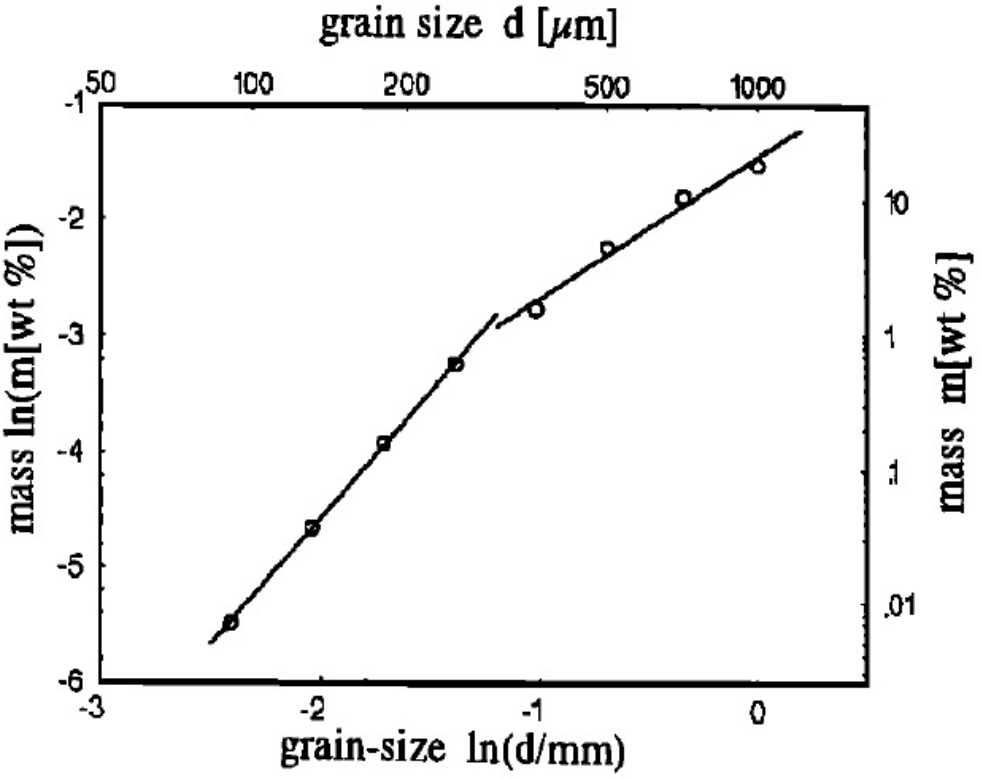

Figure 2.6: *Fragment size distribution from MFCI-experiment Zimanowski et al. [1997b]. Two different slopes is observed for the fragments.*

impact, and has been applied in various fields. Many theoretical works have been performed to explain the distribution [Brown and Wohletz, 1995].

Fragmentation of a material occurs when propagating fractures merge and divide the material into different pieces. To understand the nucleation and propagation of fractures is therefore of great importance in the study of fragmentation. This was highlighted by the experimental and theoretical work by Gilvarry and Bergstrom [1961], Gilvarry [1961]. They studied instantaneous fragmentation, i.e. fragmentation occurring in one or a few events. Their hypothesis was that fractures nucleate from flaws within the volume, on the surface and on the edges of fragments. Their experiments were performed by crushing glass spheres with an applied load. The glass spheres were contained in gelatin to avoid secondary fragmentation. The

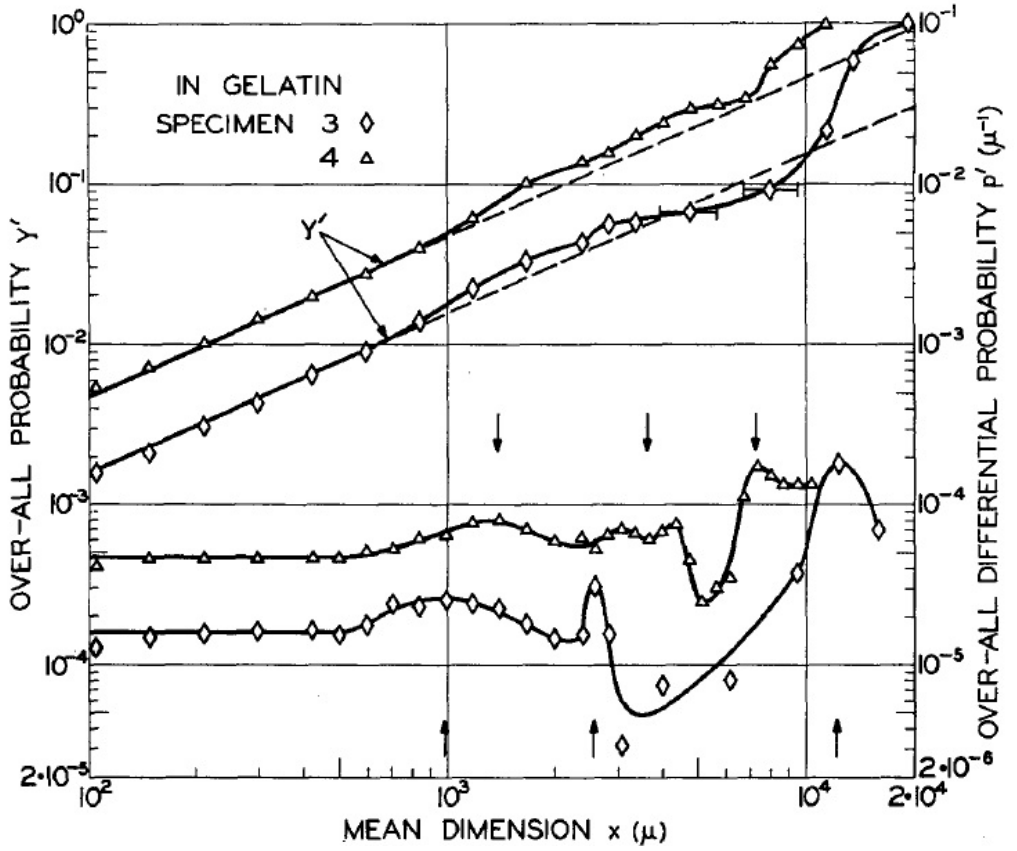

Figure 2.7: *Plot of the probability y′ (left scale) and differential probability p′ (right scale) for instantaneous fragmentation as a function of the mean dimension x for two experiments. There is observed bumps in the probability for certain sizes (marked by arrows). Figure from Gilvarry and Bergstrom [1961]*

experiments showed that there is a higher probability of finding fragments within certain size intervals, i.e. jumps in the probability function at certain sizes (see figure 2.7). They inferred this to be because of the already existing flaws in the material. The jumps in probability were found only for the larger fragments. For smaller fragments they found that the fragment sizes follow a power-law distribution.

Gilvarry and Bergstrom [1961] experiments show that the existence of flaws within a material may control the fragment size distribution and

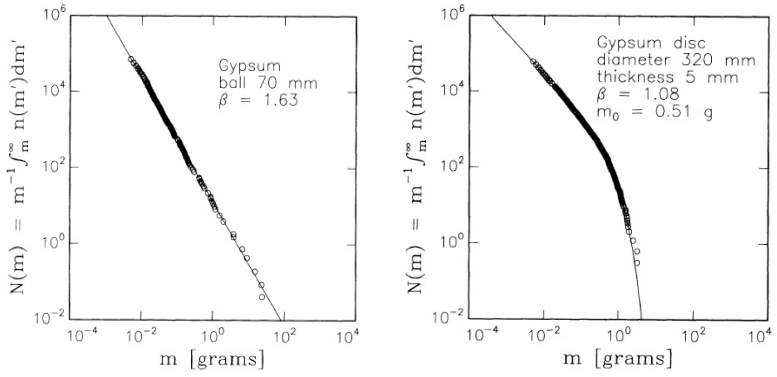

(a) Ball **(b)** Disc

Figure 2.8: *Fragment size distribution from Oddershede et al. [1993] for two different shapes. The exponent β of the power law differ for the different shapes. Power law is achieved only for the smallest fragments for a disc.*

thereby the importance of understanding how the structure of a realistic material affects the fragmentation process.

The observation that the fragment size distribution often displays a line in a plot with logarithmic axes, i.e. power-laws, has led many to believe that fragmentation processes are subject to some scaling laws. A study of scaling laws in fragmentation processes was performed by Oddershede et al. [1993]. They wanted to find out if there exists a power β such that for an arbitrary length scale, a, there is a relation

$$n(am) = a^{-\beta} n(m) \tag{2.2}$$

where n(m) is the probability distribution and m is the mass. This β is the same as the slope D that was used in section 2.1. This gives the cumulative distribution

$$N(m) = \frac{1}{m} \int_m^\infty n(m')dm' \tag{2.3}$$

To study the scaling relations Oddershede et al. fragmented various shapes of gypsum by dropping them on the floor. In figure 2.8 the fragment size distributions for a ball and a disc is shown. The experiments indicated that there exist scaling relations , i.e. power laws, for all shapes. The power law exponent, β, however differed for different shapes. In particular they found that for flat disks scaling was only achieved for the smallest fragments.

The size at which the scaling ended, called the cutoff mass, suggested that scaling was only achieved for fragments with sizes and mass less than the thickness of the disk. The observation that the size distributions show a different scaling for fragments which are of the same size as the thickness of the system has been noted also by other authors, [Gilvarry and Bergstrom, 1961]. To test wether material properties play any role on the exponent, β, they fragmented cubes of frozen potatoes, soap and stearic paraffin. They found no dependence of the exponent on the material.

The experiments by Oddershede et al. [1993] show that the geometry of the fragmenting system is of great importance for the fragment size distribution. The type of material which is fragmented does not, however, affect the fragment size distributions.

In all of the experiments mentioned above only the final product is available for analysis. This means that interpretation of the mechanisms of fragmentation is more or less impossible. Kadono and Arakawa [2002] did experiments where they studied the power-law exponent, D, through time. They studied the fragmentation of a glass plate that was fragmented by a high velocity impact on the uper side of the plate (see figure 2.9 for a schematic view of their experimental system). They monitored the fragmentation process with a high speed camera. By analyzing the images from the high speed camera they were able to calculate the exponent of the power law of the fragment size distribution through time. The experiments showed that the power-law exponent, D, increases with time.

The experiments by Kadono and Arakawa [2002] indicate that fragmentation is a transient process.

What do the experiments tell us

The experiments mentioned above, except the ones performed by Kadono and Arakawa [2002], only analyze the final product and are therefore not able to tell us anything about the dynamics of fragmentation. The advantage of experiments, however, is the opportunity to systematically vary parameters. The experiments tell us that:

- The MFCI-model provides a plausible explanation for the violent interaction between magma and water. However, the experiments are too complex to offer substantial understanding of the fragmentation process.

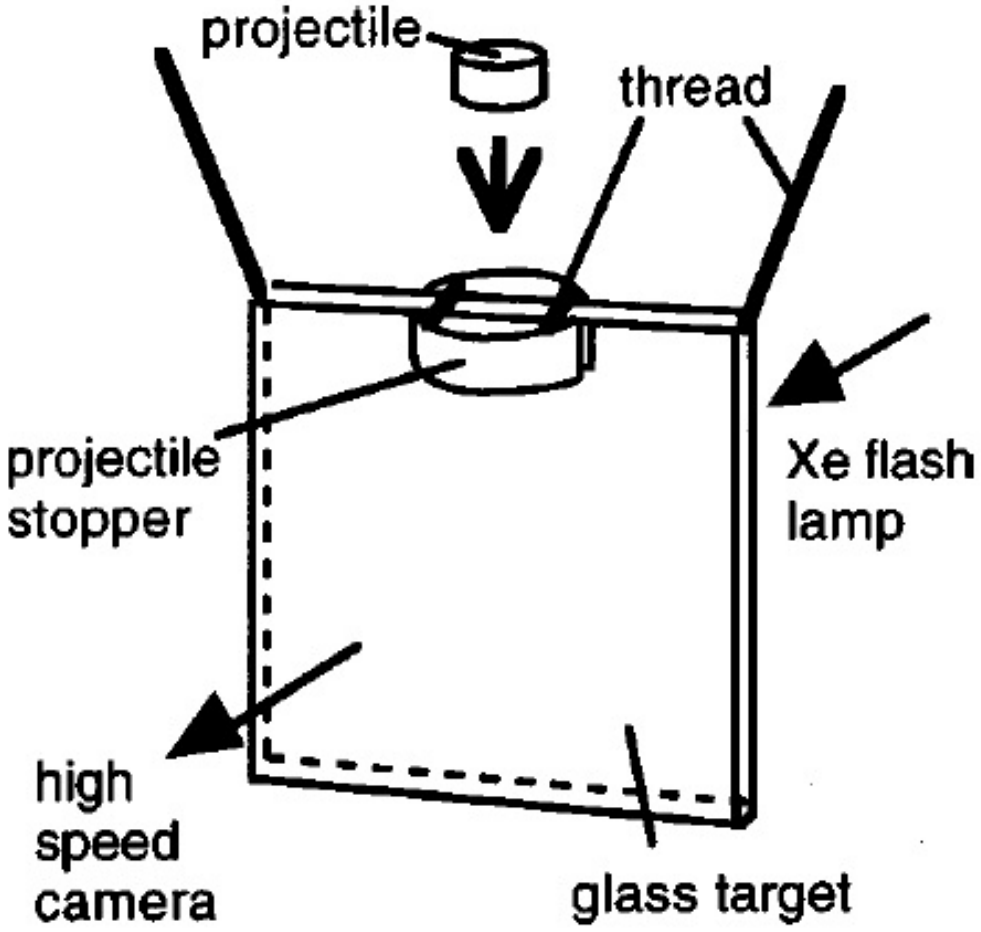

Figure 2.9: *Schematic view of the experimental system of fragmenting glass with high velocity impact by Kadono and Arakawa. Figure from Kadono and Arakawa [2002]*

- The flaws within realistic materials have consequences for the fragment size distribution.

- The fragment size distribution can vary for different shapes but not for different materials.

- The exponent of the power law distribution, D, increase through time during the process of fragmentation.

- All the fragment size distributions from the presented experiments are given as power laws, however, there are several experiments that report other types of size distributions, for more information see Åström [2006]

2.3 Theory and simulations

Fragmentation processes can be studied by either theory, numerical simulations, experiments or field work. The different disciplines have different approaches, but a common ground for all is the use of fragment size distributions. While experiments and field work can give insight into the conditions and nature of the process, the theoretical approach serves as a tool for interpretation, understanding and prediction.

How the process of fragmentation works is not yet fully understood. No single satisfactory theory of fragmentation has been established, and a number of different models are in use, [Grady and Kipp, 1985].

From a theoretical point of view, the models serve as explanations to the process of fragmentation. The assumptions that go into the theory have consequences for the predicted form of the fragment size distribution. From an empirical point of view one would already have data points in a fragment size distribution, and the model would be used to fit to these points in order to interpret the data. If a given model predicts the same fragment size distributions as is given by the points, it is assumed that the theory is capable of explaining the process. A review of different statistical models is given by Åström [2006], Wohletz et al. [1989], Grady and Kipp [1985]. Some of these models are presented in the following sections.

Earlier models

Processes of fragmentation have been studied for over a century and different scientific and engineering fields have shown interest in the process.

Three years after the experiments by Rosin and Rammler (see section 2.2), Lienau [1936] discussed a 1-dimensional fragmentation problem. Lienau experimented on thin brittle rods and discussed the similarities between the experiments and a line separated by randomly distributed points. Lienau pointed out that the distribution of the fragment lengths created by this random partitioning brings forth the relevance of a Poisson distribution.

Mott [Mott and Linfoot, 1943, Mott, 1943a,b] (as described by Åström [2006]) derived a model similar to that of Lienau with a 1D Poisson process, and he extended the model of Lienau to the random fragmentation of an area separated by vertical and horizontal lines. The 1D model results in a fragment size distribution of the form $N(l) \propto exp(-\sqrt{l})$, where l is the length of the fragment. For the 2D case Mott arrived at a fragment size distribution of a similar form with $N(a) \propto \sqrt{a}K_1(\sqrt{a})$, where a is the area of the fragment and K_1 is a modified Bessel function.

A different model was proposed by Gilvarry [1961] who assumed that materials have *a priori* uncorrelated flaws within the volume, on the surface and on the edges of fragments. So that when a material experiences loading, the fractures are activated from these flaws. He assumed that the fractures are activated according to Poisson statistics. Under these assumptions Gilvarry derived a fragment size distribution for instantaneous fragmentation. The expression of this fragment size distribution is given as

$$n(v) = q(v)v^{-(S-1)/S}exp(\frac{-v}{V_0}), \tag{2.4}$$

where S is the spacial dimension, v_0 is related to the frequency of the Poisson process and $q(v)$ is the density of fragments, prior to the fragmentation event, of size v. This was set to $q(v) = V_0/v$, where V_0 is the volume of unbroken object. This hypothesis was tested in the experiments discussed in section 2.2 where it was found that certain fragment sizes had a larger probability than others to be produced.

All the models presented above are based on Poisson statistics, this means that fractures are nucleated at random. The models predict an exponential fragment size distributions.

Geometric fragmentation theory

The idea that fragmentation can be simulated as a domain being separated by points, lines or surfaces, in 1, 2 or 3 dimensions respectively (see Lienau and Mott above), has persisted. This model is known as *geometric fragmentation* and is discussed in detail by Grady and Kipp [1985] and Grady [2006]. In figure 2.10 some examples from simulations of geometric statistical fragmentation are shown.

In geometric fragmentation one assumes that the fragmentation process is random and that no material response or physical conditions are necessary to consider. This is based on the assumption that if a satisfactory theory of geometrical statistical fragmentation is found, the deviation from an observed fragment distribution would be expected to result from the material properties or the physical conditions. That is, geometric fragmentation assumes that fragmentation is a statistical problem.

In the models by Lienau [1936] and by Mott and Linfoot [1943], Mott [1943a,b] the fragments were produced by points or lines placed within a domain as a Poisson process. Grady and Kipp [1985] suggested that this way of partitioning the domain might not be the most realistic since it requires the system to be statistically homogeneous. Statistical homogeneity means that the probability of finding a fragment of a particular size is independent of position. In natural systems this is seldom the case, since the loading conditions are almost always such that some part of the material is more fragmented than others. This can for instance be seen when a small rock fractures the windscreen of a car: the damage is greater near the impact zone and less radially outwards. To avoid this problem Grady and Kipp suggested that a more appropriate random variable is the fragment mass rather than the fragment size. The mass of the fragment is then distributed over the fragment number by a Poisson process, i.e. the mass of the fragment is viewed as a random scalar variable.

This also transforms the 2D or 3D fragmentation problem into a 1D problem since the mass can be regarded as a scalar independent to what type of dimension it is distributed in. Fragmentation is determined by breaks distributed randomly over the scalar measure of mass. The breaks determine the Poisson variate and lead to the following fragment size distribution

$$F(m) = 1 - e^{-m/\mu}, \tag{2.5}$$

where m is the mass of the fragment and μ the average mass [Grady, 2006].

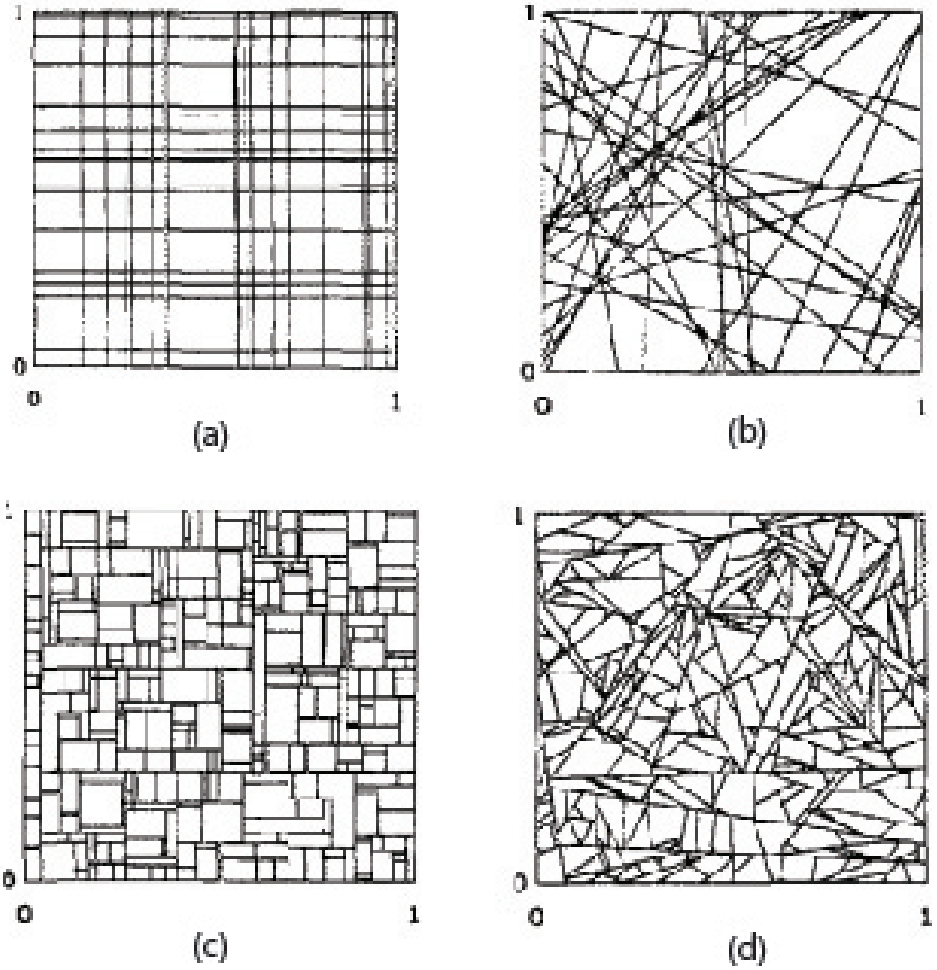

Figure 2.10: *Plots from numerical simulations of geometric statistic fragmentation model as described by Grady and Kipp. a) Random fragmentation with infinite vertical and horizontal lines. b) Random fragmentation with randomly oriented lines. c) Random fragmentation with finite vertical and horizontal lines. d) Random fragmentation with finite randomly oriented lines. Figures from Grady and Kipp [1985]*

Grady and Kipp [1985], did numerical simulations in order to support their model. In their simulations they divided a 2D domain by sequentially placing random lines using different algorithms, see figure 2.10 for illustrations. It was shown that the algorithm chosen to fragment the domain controls the fragment size distribution. It was also shown that by sequentially dividing the area into smaller and smaller fragments the fragment size distribution converges to the linear-exponential distribution of equation 2.5.

The geometric fragmentation model has the advantage of being a simple model because the assumption that fragmentation is a statistical problem leads to a simple mathematical expression. The derivation is based on Poisson statistics, and predicts an exponential fragment size distribution. The simulation by Grady and Kipp [1985] shows that the process by which the fragmentation occurs, i.e. the algorithm for dividing the area, changes the outcome of the fragment size distribution for the first sequences of fragmentation. Only after a certain amount of sequences of fragmentation does the fragment size distribution resemble equation 2.5.

Sequential Fragmentation theory

Wohletz et al. [1989] and Wohletz and Brown [1995] suggested a model based on the observation that fragmentation processes generally follow a sequence of events involving crack nucleation, growth and branching, during repetitive stress and strain. They named the model *Sequential fragmentation theory*. An illustration of sequential fragmentation is shown in figure 2.11

Due to the sequential nature of fragmentation they proposed to model fragmentation as an integral where a parental mass produces an ensemble of daughter fragments which in turn become parental mass giving rise to further daughter fragments and so on. Conservation of mass leads to the integral

$$n(m) = c \int_m^\infty n(m') f(m' \to m) dm', \tag{2.6}$$

where $n(m)$ is the number distribution in units fragments per unit mass m between m and $m + dm$, c is a constant, $n(m')$ is the number distribution of the parental mass m' and $f(m' \to m)$ is the single-event distribution function and expresses the distribution of mass m arising from m'.

Equation 2.6 can seem rather complicated. A way to understanding this expression is by thinking of $f(m' \to m)$ as the probability that the

fragment of size m' produces a fragment of size m. The number distribution $n(m')$ is the number of fragments of size m'. In this view the product $n(m')f(m' \rightarrow m)$ is the probability of all fragments of size m' to produce particles of size m. So equation 2.6 is the integral over these probabilities for all sizes.

Assuming that fragmentation mechanisms always show a mass dependency, the single-event distribution function is set to

$$f(m \rightarrow m') = \Big(\frac{m}{m_1}\Big)^{\gamma}, \tag{2.7}$$

i.e. a power-law. The parameter γ is a free parameter and m_1 is related to the average size.

By inserting equation 2.7 into equation 2.6 and solving it for $n(m)$ yields a fragment size distribution,

$$n(m) = \frac{N_T}{m_1}\big(\frac{m}{m_1}\big)^{\gamma} exp\Big(-\frac{(m/m_1)^{\gamma+1}}{\gamma+1}\Big),. \tag{2.8}$$

where N_T is the total number of fragments.

The free parameter γ models the maturity of the fragmentation process, i.e. how many sequences of fragmentation occur in the process, see figure 2.11. With a γ close to -1, equation 2.8 models an instantaneous fragmentation process with only one or a few sequences of fragmentation. This leads to a broad, poorly defined distribution of fragment sizes. With increasing γ, equation 2.8 models a process of a culmination of many individual breakage events thus creating a greater central tendency and finer average size. Brown and Wohletz [1995], showed that by dividing equation 2.7 and equation 2.8 the Rosin-Rammler distribution is obtained [Rosin and Rammler, 1933]. They also showed that equation 2.8 is identical with the Weibull distribution (not discussed here, see Wohletz et al. [1989] for more information)

Sequential fragmentation theory views the fragmentation processes as sequential events. This assumptions leads to the important results that also Kaminski and Jaupart [1998] found (see section 2.1), namely that the fragment size distribution can vary when the degree of fragmentation is increasing. The derivation of the mathematical expression using this assumption leads to a power law distribution with an exponential correction (see equation 2.8).

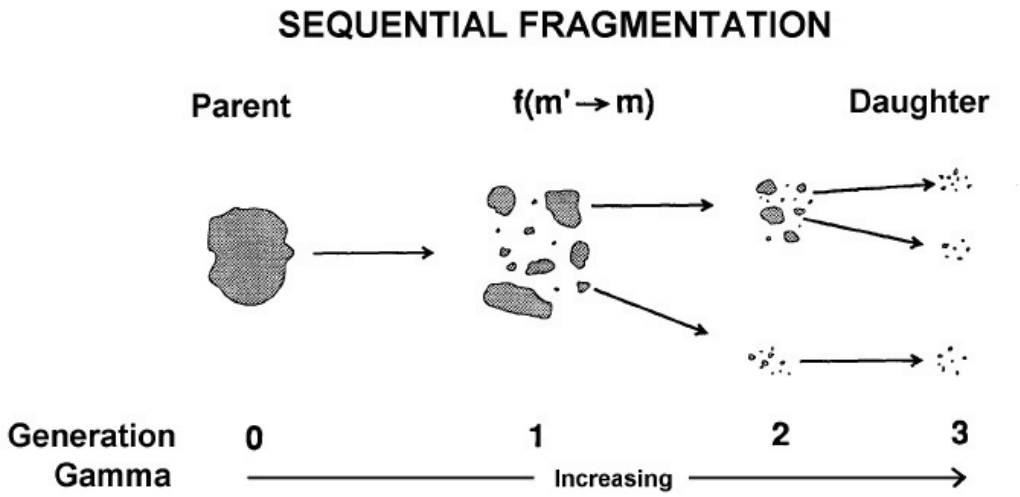

Figure 2.11: *Schematic illustration of sequential fragmentation, figure from Wohletz and Brown [1995]*

Åström model

This section is based on the article of Åström [2006]. In some of the models above the fractures were approximated as simple lines or surfaces, see section 2.3. However, Fineberg and Marder [1999], showed that fast propagating fractures are unstable and will branch and split. This shows that lines and surfaces are not an appropriate approximation for rapid fragmentation.

Flaws in the material play a crucial part for the material strength. The experimentally measured stress level needed to fracture a material is 10-1000 times lower than the theoretical estimates [Åström, 2006]. This is because theory predicts that a material will break apart if the stress level is higher than the potential between the atoms that constitutes the material. Since the theory does not account for weaknesses in the material it overestimates the strength of the material.

A brittle material will, in general, never be perfectly uniform and will always contain some flaws. Assuming that the flaws are microcracks, it is reasonable to assume that there is a higher probability of nucleation of fractures from such a flaw, due to the fact that stress is increased at crack tips. This model starts out with the assumption that brittle materials have an *a priori* density of micro cracks within its domain and that fractures

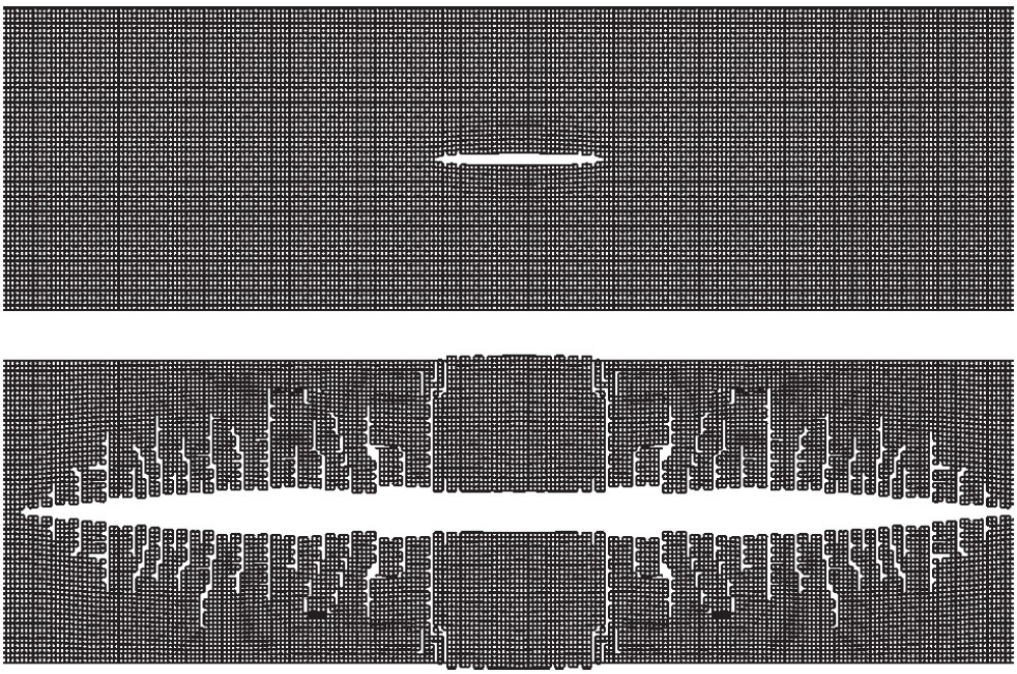

Figure 2.12: *Snapshots of simulations from Åström [2006]. Top: the propagation of a fracture that was nucleated at a microcrack in the center. Bottom: the fracture velocity is sufficiently high to produce side branching.*

nucleate from the micro cracks as a Poisson process.

As the fractures open up the propagation velocity increases. Theoretically the crack should accelerate up to the sound speed of the material, however, before the sound speed is reached the crack becomes unstable and starts to split and branch, see figure 2.12. The side branches may be caused by shear stress that builds up behind the crack tip. Since the creation of a side branch causes the shear stress to decrease again, a periodic effect might be expected, see figure 2.12.

Due to stress enhancement the side branches will turn toward the nearest free surface, thus creating fragments. The fragments created by side branches will typically be small fragments due to the relative short penetration depth of the branches. As a branch merges with the free surface a junction is created. At this junction the fastest propagating fracture can continue to grow. This leads to first generation and second generation fractures. Due to the periodic fashion of the branching the first generation

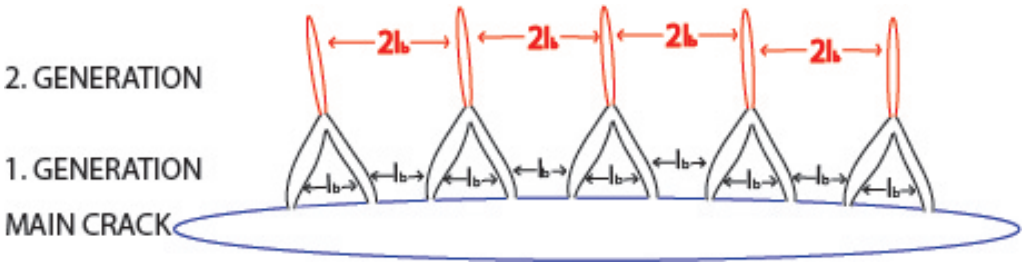

Figure 2.13: *Simplified sketch of 1. and 2. fractures. Length of branches are exaggerated for visual effect.*

fracture will have well-defined mutual distance l_b. In a similar fashion the 2. generation will have a mutual distance of $2l_b$. A simplified sketch of first and secondary fractures is shown in figure 2.13. It is possible to set up a size distribution for these fragments,

$$n(v) \propto v^{-\alpha} f(v/v_1), \tag{2.9}$$

[Fineberg and Marder, 1999], where v is the volume of the fragments, $\alpha = (2S-1)/S$, S is the dimension, $f(v/v_1)$ is a scaling function that is unknown, but is likely to be similar to an exponential, and v_1 is associated with the penetration depth of the fractures. Equation 2.9 is derived with consideration of dissipation of branching and bifurcation processes, and elastic relaxation of existing fragments. There are some requirements that need to be met in order for equation 2.9 to be true. (i) Branches need to appear at intervals that can be characterized by a typical length scale, thus no scale invariant distribution is allowed. (ii) Fragments need to have an aspect ratio that is independent of size, (iii) and the process needs to be heterogeneous enough to produce a continuous distribution.

Grady [1982] found that for a fragment to form, the elastic energy needs to be larger than the surface energy of the fragment. If a fragment of size L is created in a system where the elastic energy is increasing with time, t, as $L^S \tau t$ where τ is the strain rate, there is a lower limit for the time at which the fragment can be formed. This time is $t = L/v_{sound}$. It is thus more energetically favorable to produce large fragments, but at high strain rates there is not enough time to form them. This leads to the scaling relation

$$v_{uncorr} \equiv L^S \propto \tau^{-2S/3} \tag{2.10}$$

This scaling relation is derived for equilibrium conditions and is therefore not always satisfied. Also it does not take into account that microcracks, that govern the fracture initiations, have different orientations and length distributions for different materials. Even so, the relation in equation 2.10 has been confirmed several times, [Grady, 1982, 1990, Åström, 2006]

In Åströms model the large fragments are assumed to be made by the main fractures (fractures nucleated from the microcracks). The side branches are assumed to create the small fragments. This leads to the total fragment size distribution

$$n(v) = (1 - \beta_r)v^{-\alpha}exp(-(2/\lambda)^S v) + \beta_r exp(-v_{uncorr}(v^{1/S} + \lambda)^S). \quad (2.11)$$

Where λ is the penetration depth, $v^{1/S}+\lambda$ is the reduced size of the Poisson-process fragments, β_r determines the relative normalization of the two parts of the distribution and v_{uncorr} is the volume of fragments created from the nucleated fractures.

Åström's model is a sophisticated model that accounts for many observations of realistic materials. What the model gains in sophistication is, however, lost in the complexity. This is due to the difficulties of measuring the penetration depth, λ, and v_{uncorr} from a sample of fragmented material. In addition, part of the derivation is based on equilibrium conditions, e.g. equation 2.10, a condition which is seldom satisfied for fragmentation processes.

Åström's model distinguishes between the small and the large fragments, where the small fragments are represented by a power law distribution (first term in equation 2.11) and the large are represented by an exponential distribution (second term in equation 2.11). The reason for the different distributions for small and large fragments is that they are produced by different mechanisms: small fragments are created due to merging of branches (leading to a power law distribution) and the large fragments are created from the main fractures (that are nucleated in a Poisson process and therefore have to an exponential distribution).

What do the theory and the simulations tell us?

Theories and simulations have the advantage of stating the mechanisms behind the processes and are able to predict and not only describe. Their disadvantage, however, is that in order to derive an mathematical expression

it is necessary to simplify the problem. This can in some cases lead to too simple expressions. Simulations have additional problems associated with numerical uncertainty. To sum up, the models presented above can tell us that

- Fragment size distributions can be described by power laws and/or exponentials
- The theoretically predicted fragment size distributions are controlled by how the fragmentation occurs, i.e. the algorithm.
- The fragment size distributions are controlled by the degree of fragmentation
- The fracturing process is controlled by the microstructure of the material.

2.4 What is missing?

In this chapter the different approaches for studying fragmentation and explosive volcanism have been presented. To study complicated systems such as these, all the approaches mentioned above are needed. There are, however, some limitations.

Field work has the advantage that the fragments in volcanic deposits can be studied. This gives us the first order observations of the processes. The limitation of field work is that the volcanic deposits are likely the product of a number of different processes and the volcanic deposits are only the final product of a very complicated system. This makes it difficult to interpret what processes lead to the final product.

The MFCI experiments give us a plausible explanation of how water and magma can interact and cause explosions, but also in this approach only the final product can be studied. A MFCI experiment is a very complicated system and there are a lot of uncontrolled physics in the experiments. There are also limitations with the scaling of an actual phreatomagmatic eruption.

The theoretical models serve as explanations for the processes of fragmentation and fragment size distributions. However, even though several experiments and simulations have been done to verify the models, no final consensus has been reached explaining fragmentation. This is because the

theoretical models are hard to test. Another problem is that the models are often too simplistic so that they are far from reality.

One of the challenges in studies of fragmentation in explosive volcanism is related to the fragment size distribution of the volcanic deposits obtained by different studies. Field work in general shows a power law distribution, whereas the mathematical models predict exponential, lognormal or power laws with an exponential correction distribution. This gap between the field observations and the mathematical description highlights the importance of an interdisciplinary approach to solve problems in geoscience.

In addition to these points there is also a more subtle problem in the literature mentioned above. This problem is related to the interpretation of the exponent value D in the fragment size distribution. The problem can be illustrated by the views of Kaminski and Jaupart [1998] and Zimanowski et al. [1991]. Kaminski and Jaupart argue that the volcanic deposits are first fragmented in the volcanic eruption, giving a D-value of 2.6. Afterwards, the deposits experience further fragmentation in processes similar to grinding. This leads to a D value above 3. On the other hand, Zimanowski et al. interpret the different values of D as a consequence of different types of fragmentation processes by which the material has fragmented. So, the problem is that the value of D can be interpreted as a consequence of different factors, either the degree of fragmentation or the process.

To be able to address the problems mentioned above we need a controlled system that can produce fragment size distributions that are comparable with the data sets from field studies. The system has to allow for monitoring of the transient behavior of the fragmentation processes, so that we can observe and quantify the processes through time. We need to be able to vary parameters in the system in order to to derive scaling laws. With a system like this we can better understand the mechanics and physics behind the fragmentation processes.

Chapter 3

Experiments and Results

3.1 Experimental setup

The experiments were performed in a vertically oriented Hele-Shaw cell as seen in figure 3.1. A 490mm long tube with an inner diameter of 4mm connects the cell to a 5 liter pressure tank. The tube is connected to the cell via an inlet which is placed 25mm into the cell, the inner diameter of the inlet is 2mm.

A pressure gage is fitted to the tank to be able to monitor the pressure in the tank. Air can be released into the cell by opening a fast valve (Actuator, solenoid valve, opening time of 0.1second to fully open).

A high speed camera (Photron Fastcam SA5) is placed in front of the cell to monitor the experiments. The distance between the camera and the cell was either 1.5 meters or 2 meters, giving a $pixel/cm^2$ ratio of $(0.038cm)^2$ and $(0.056cm)^2$, respectively[1]. During experiments the high speed camera takes pictures at a rate of 4000 frames per second. The high speed camera takes pictures at such a high rate that common lighting using alternating current will cause periodic changes in light conditions. Therefore a special lamp (Highlight 440) that produce constant light conditions is placed above the camera.

[1]This is measure from a 10 cm scale that is taped on the cell

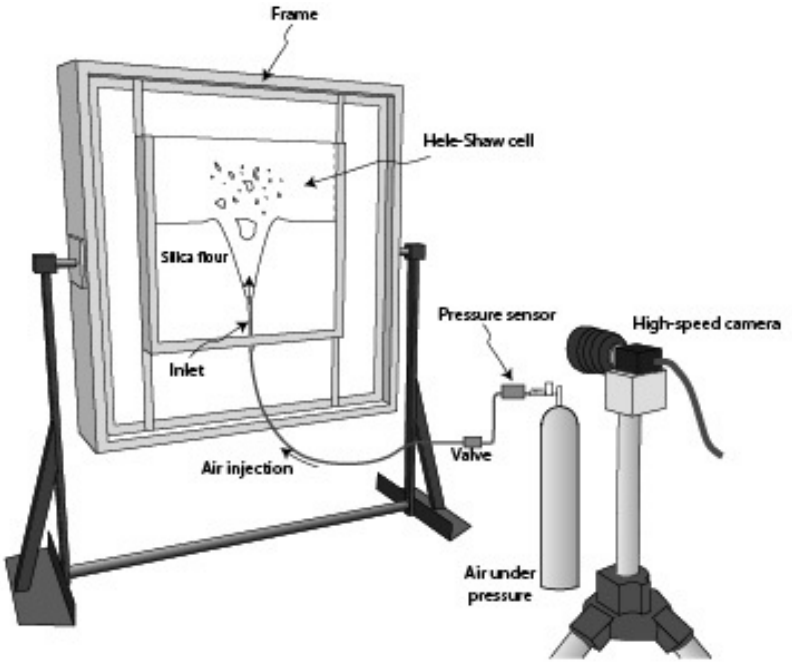

Figure 3.1: *Experimental setup*

The material

The material used to represent a solid is a crystalline silica powder. The material properties of the silica powder have been determined by Galland et al. [2006] and Galland et al. [2009]. The silica powder has a grain size of $10-20\mu m$ and fails according to a Mohr-Coulomb criterion. The grains are angular, see figure 3.2, so that when compacted they interlock. The silica powder is therefore cohesive on a macroscopic scale.

Cohesion, internal friction and tensile strength of the silica powder was determined by Galland et al. [2006] and Galland et al. [2009] using a Hubbert shear box. Their tests showed that the cohesion and tensile strength of the silica powder are dependent on the compaction. It is therefore necessary to control the compaction of the silica powder. For compacted silica powder the cohesion was measured to be $369 \pm 44Pa$ and the friction coefficient is 0.81 ± 0.06 which yields an angle of internal friction of $\Phi = 39°$. The tensile strength was measured to be $\approx 100Pa$.

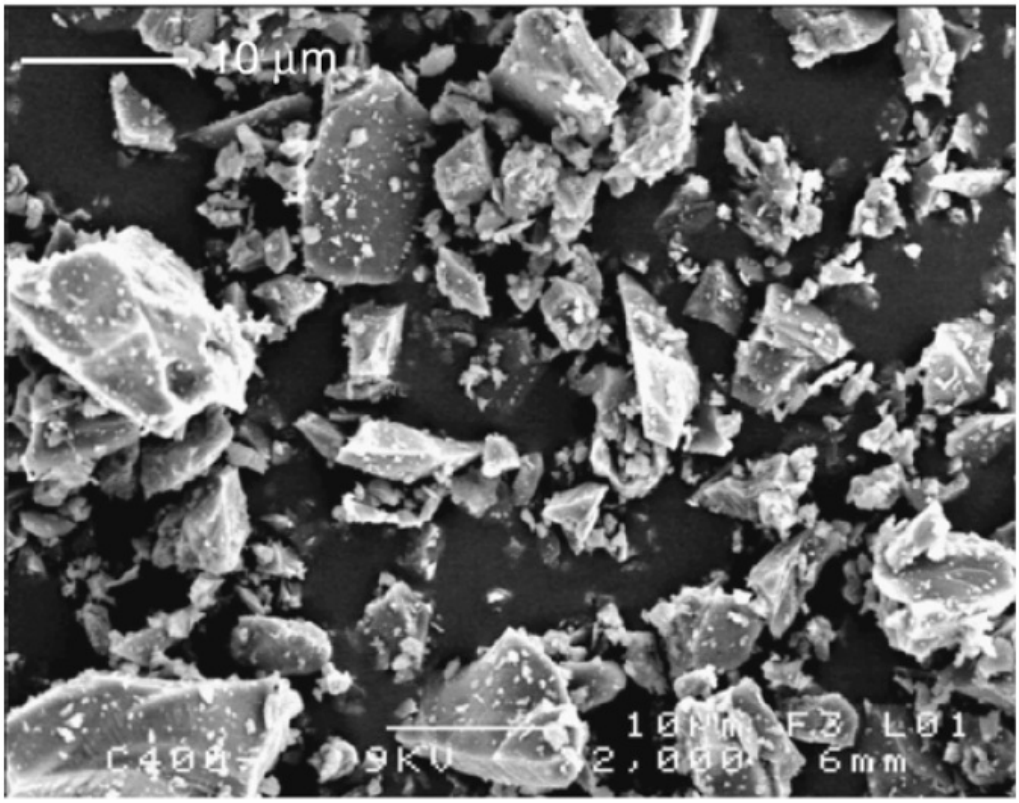

Figure 3.2: *Scanning electron micrographs of crystalline silica powder. Image from Galland et al. [2006]*

Compaction

Since the compaction is a critical parameter for the material properties the silica powder is compacted before each experimental run. The compaction is performed by placing the cell on top of a table that is connected to a high frequency vibrator (Houston Vibrator model GT-25). The vibration causes fluidization of the powder. An aluminum plate is placed on top of the powder during vibration to make sure the surface of the powder is flat. During vibration the volume of the material decreases, i.e. the powder compacts, until it reaches a steady state. The compaction is therefore a function of the time of vibration. This means that we can control the amount of compaction to a desired value.

Before each experiment the powder is compacted until it reaches a de-

sired density of $1.05 g/cm^3$, which is the density used by Galland et al. [2009]. The density is measured by controlling the height of the compacting powder. That is, the cell is filled with a known mass of powder. The width and thickness of the cell is known, and the only geometrical parameter that vary during compaction is the height. This means that before an experiment the powder needs to be compacted to a height determined by

$$h = \frac{m}{\rho w b}, \tag{3.1}$$

where m is the mass of the powder, ρ is the desired density and w and b is the breadth and thickness of the cell, respectively.

3.2 Performing the experiment

The cell is filled with a known mass of silica powder and mounted on the vibrating table. A plate is placed on top of the powder inside the cell to keep the surface of the powder flat during vibration. The vibration is started by connecting the vibrator to pressurized air (from the air supply in the lab) of $4 \cdot 10^5$ Pa. As the cell vibrates, the height of the powder is monitored. The vibration is stopped when the desired height, i.e density (see equation 3.1), of the powder has been reached.

After compaction the cell is mounted in a frame as is seen in figure 3.1 and connected to the pressure tank. The pressure tank is filled with air to a specified pressure. A black background is placed behind the cell to improve the contrast of the images. A ventilation cap is placed on top of the cell, the cap is connected to a ventilation tube that uses a fan to suck air and dust from the cell and blows it outside the window to prevent the dust from the powder to be ejected into the lab.

The high speed camera is placed in front of the cell and starts to record. The experiments are started by opening the valve connecting the pressure tank and the cell. After the experiments, the images from the high-speed camera are stored.

Three series of experiments were conducted. One where the height of the layer was held constant while varying the pressure in the pressure tank (P-series) and two where the pressure was held constant and the height of the layer was varied (H1-series and H2-series). Since no statistics from the experiment is reliable after fragments start to leave the image frame,

the camera was placed as far back as possible (2 meters) in the P-series and the H1-series to be able to captures as much of the experiments as possible. However, this causes loss of resolution, so in H2-series the camera was placed closer to the cell (1.5 meters).

3.3 Observational results

In this section results from observations during experiments and of the experimental images will be presented. In general, it can be observed that fragments of different sizes are produced, from very fine dust particles to large blocks (see figure 3.11).

Two regimes

After several experiments had been conducted it was observed that the damage on the silica powder showed two types of patterns, see figure 3.3. One was a V-shaped pattern, caused by fractures originating from the inlet and propagating towards the surface at an oblique angle, which caused a part of the layer to be lifted up, see figure 3.3a and 3.3c. I call this pattern "lift off". The other pattern looks like a pipe, which is created by the air carving straight through the layer, see figure 3.3b and 3.3d. I call this pattern "channeling".

An illustration of how lift off works is given in figure 3.4. This shows an experiment with a pressure of $8 \cdot 10^4$Pa and a height of 10cm at five different time steps. In the upper left image the two lower red arrows point at laterally propagating fractures and the upper red arrow points at a tensional fracture propagating due to the doming of the surface. In the following image (upper middle) two new laterally propagating fractures can be observed. As the system evolves further (upper right image) two more laterally propagating fractures have formed. These fractures, however, have now an angle towards the surface (blue arrows). They will merge with tensional fractures in the layer and eventually reach the surface. Once this has happened a part of the layer is lifted up (lower left image) and eventually ejected into the air (lower right image). It can be observed that fragments and dust are ejected into the air.

In figure 3.5 four images showing the time evolution of an experiment where channeling is occurring is given. Image (a) shows that as the air

(a) Low pressure, medium height

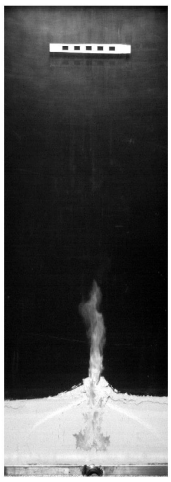

(b) high pressure, medium height

(c) Low pressure, large hight

(d) Low pressure, small height

Figure 3.3: *Examples of different patterns displayed for different parameter setups. It is seen that (a) and (c) show a similar pattern and (b) and (d) show a similar different pattern. The parameters for the different picture are; (a) ($P = 2 \cdot 10^4 Pa$, $h = 5cm$), (b) ($P = 12 \cdot 10^4 Pa$, $h = 5cm$), (c) ($P = 2 \cdot 10^4 Pa$, $h = 10cm$), (d) ($P = 2 \cdot 10^4 Pa$, $h = 2cm$)*

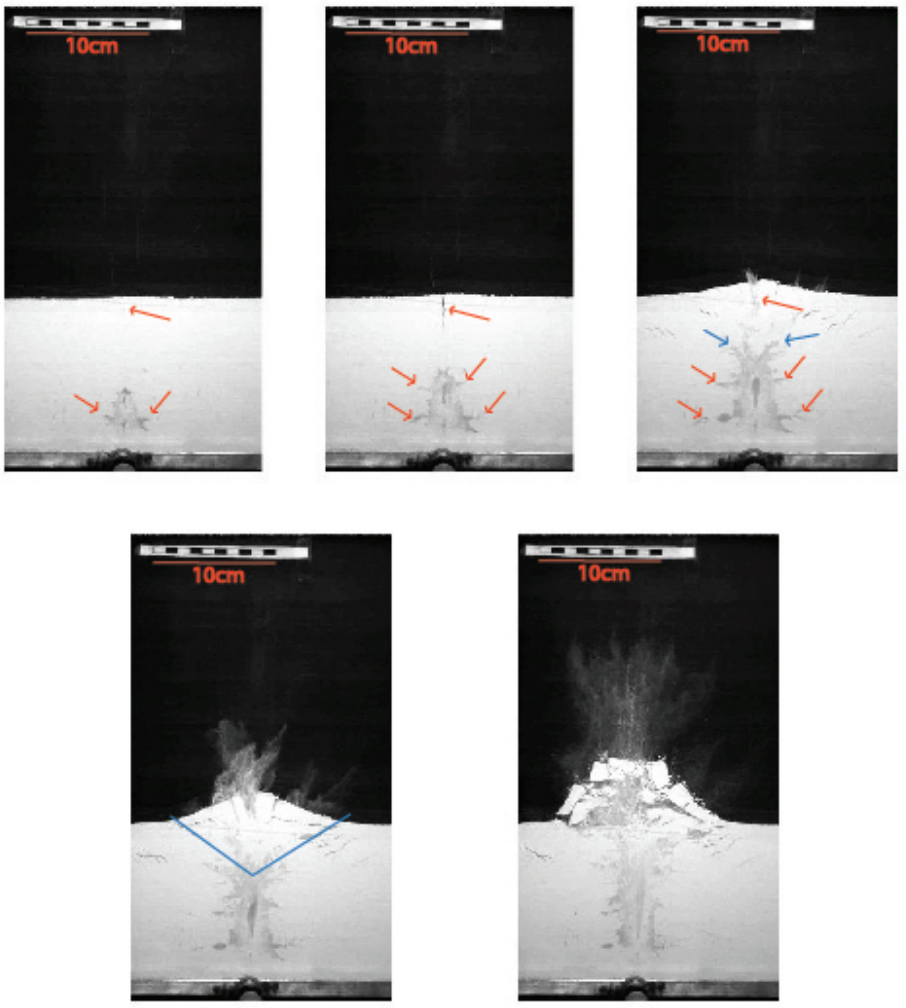

Figure 3.4: *Images showing the time evolution of an experiment ($P = 8 \cdot 10^4 Pa$, $h = 10cm$). The red arrows point at propagating fractures, the blue arrows point at the propagating fractures that have an angle towards the surface. The blue lines show the part of the layer that is lifted up.*

starts to be released into the layer a pocket of air opens up above the inlet. In (b) this pocket has increased in volume and a tensional crack can be seen on top of the layer. In (c) it can be seen that the air eventually pierces through the layer. From image (d) it can be seen that fragments and dust are produced and ejected from the channel.

In figure 3.6 a phase diagram has been set up to show how the pattern depends on the pressure and the height. By first considering only points from the P-series in the diagram (vertical points), it can be observed that for low pressures lift off is attained. For a pressure between $5 \cdot 10^4$Pa and $6 \cdot 10^4$Pa there is a change in regime, and for pressure $\geq 6 \cdot 10^4$Pa channeling is attained. This shows that the morphology is controlled by the pressure. Also, by considering the H1-series (lower horizontal points) it can be observed that channeling is attained for low heights, even though the pressure is the same as resulted in lift off in the P-series ($2 \cdot 10^4$Pa). There is a change in regime from channeling to lift off between 3.0cm and 4.0cm and for heights $\geq$ 4.0cm lift off is attained. This shows that in addition to the pressure the morphology is controlled by the height. By considering the H2-series (upper horizontal line) the same behavior as in H1 can be seen, but this time the change in regime occurs at a height between 9.0cm and 10.0cm.

In some experiments it was observed that fragments were sequentially fragmented after ejection. An example of this is given in figure 3.7. From this figure it can be observed that a large fragment is ejected from the eruption (figure 3.7a), after some time it can be seen that the fragment separates into two fragments (figure 3.7b). In figure 3.7c one of these are fragmented once more.

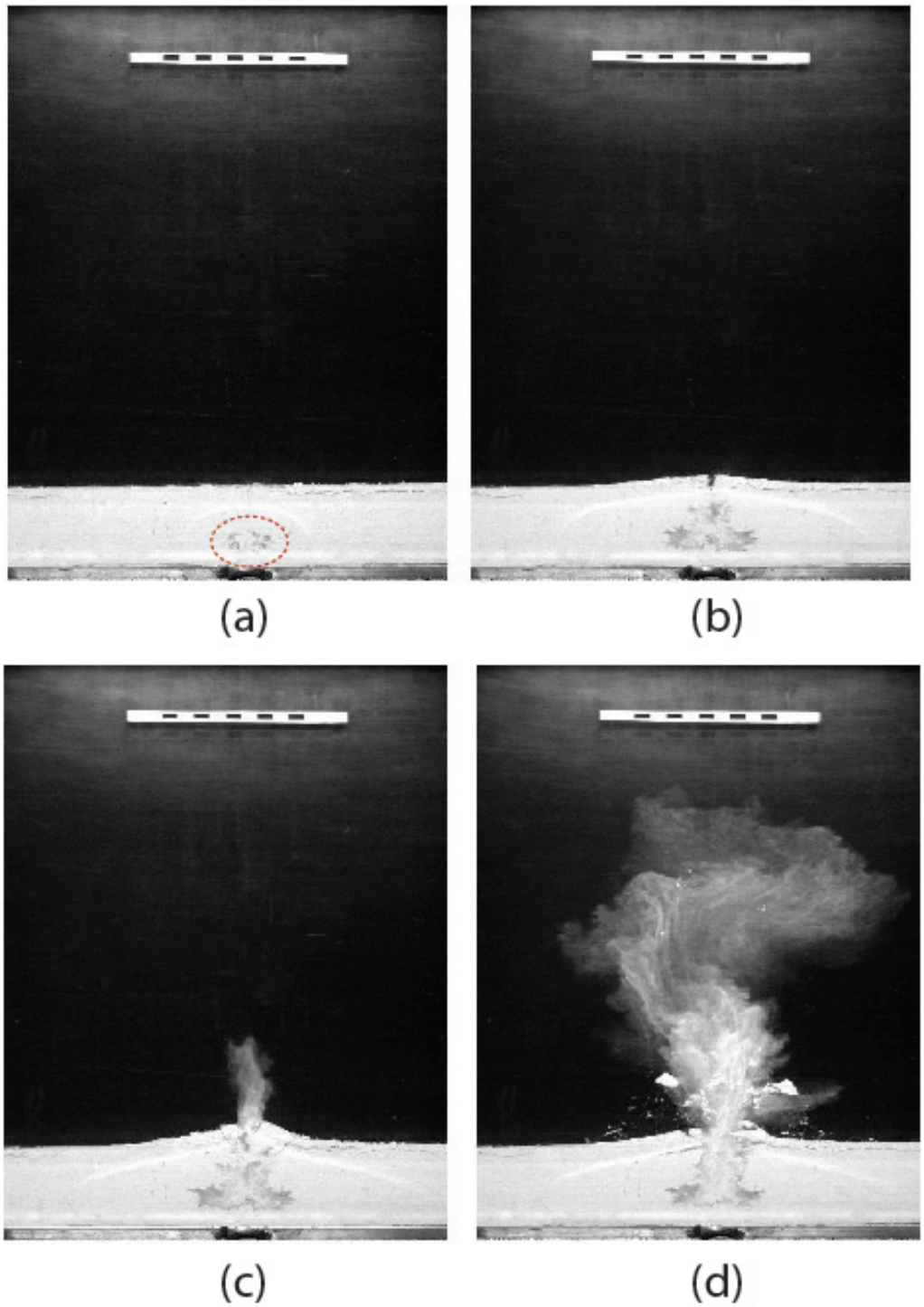

Figure 3.5: *Images showing the time evolution of a channeling-experiment. The images show the experiment at 4 different time steps from (a) to (d)*

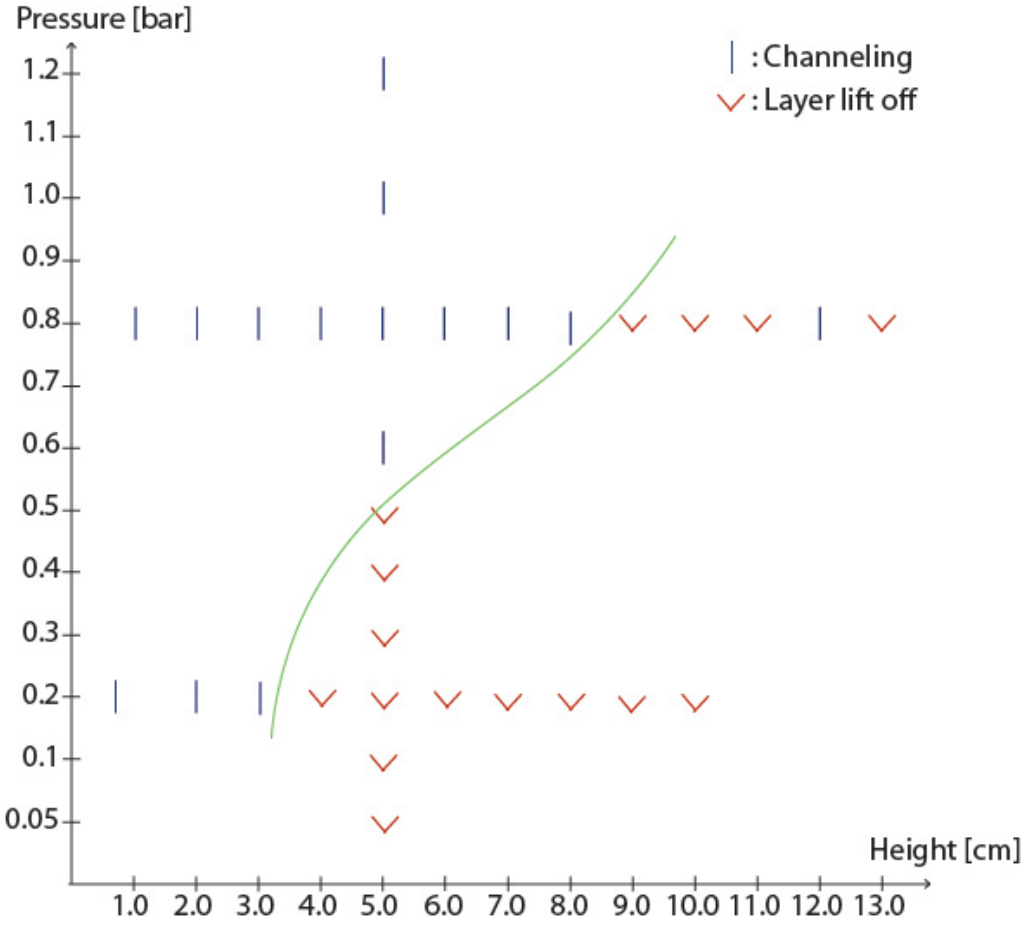

Figure 3.6: *Phase diagram*

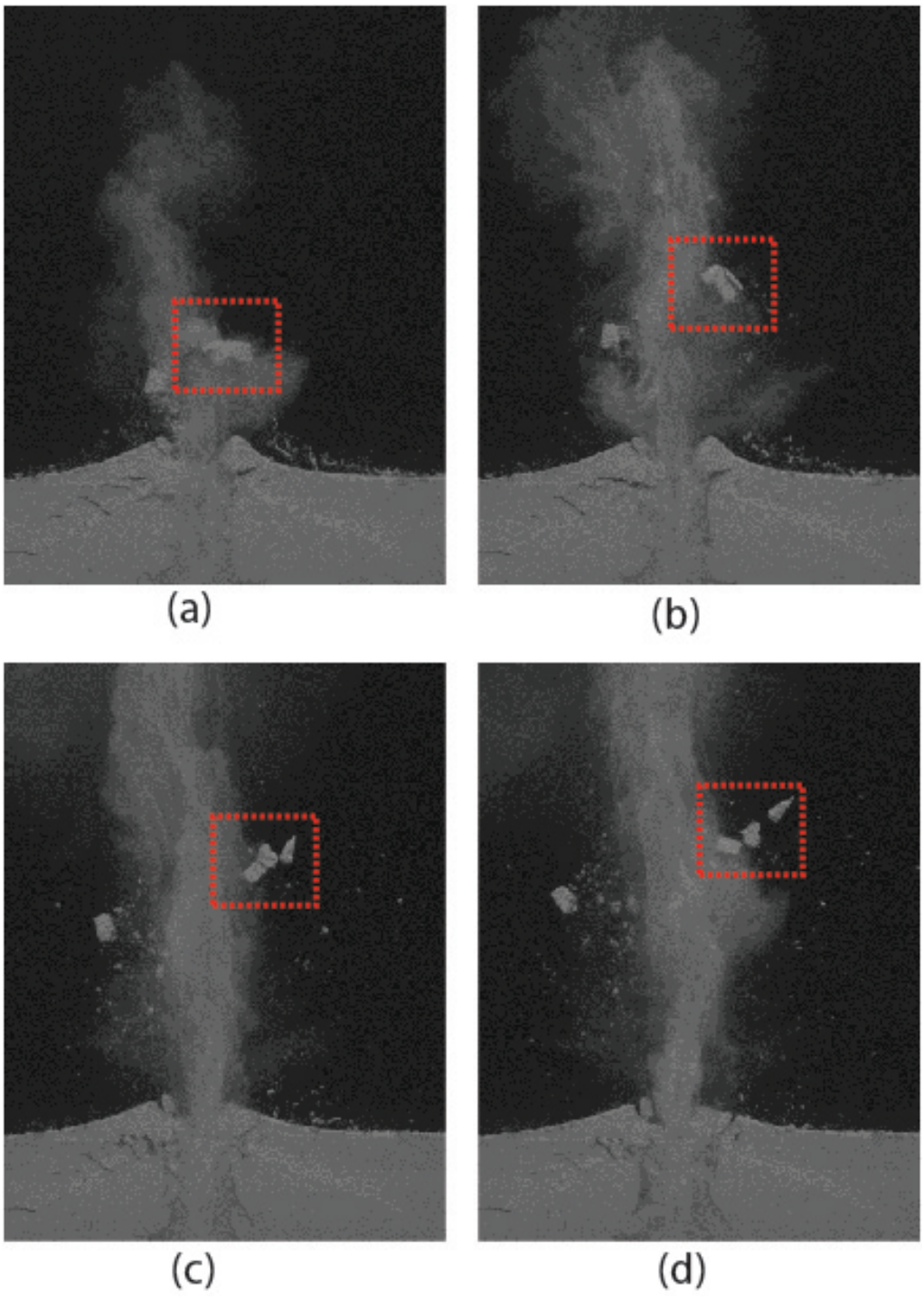

Figure 3.7: *Images showing an experiment at 4 different time steps. The time is increasing from (a) to (d). In the red box it can be observed that the fragment which is whole in (a) is sequentially separated into three different fragments.*

Compaction wave

In some of the experiments a compaction wave was observed starting from the inlet and propagating outwards. The compaction wave was possible to observe due to the damage it caused as it propagated through the layer, an example of this damage can be seen in figure 3.8. A more detailed analysis of the experimental images showed that compaction waves only occurred if the pressure was above $2 \cdot 10^4 - 3 \cdot 10^4$Pa. The position of the wave was measured through time. Some examples of the position through time for the P-series and the H1-series are given in figure 3.9.

The average velocity of the compaction waves was calculated from the starting point to the final positions. The velocities of the compaction waves as a function of pressure and height is given in figure 3.10.

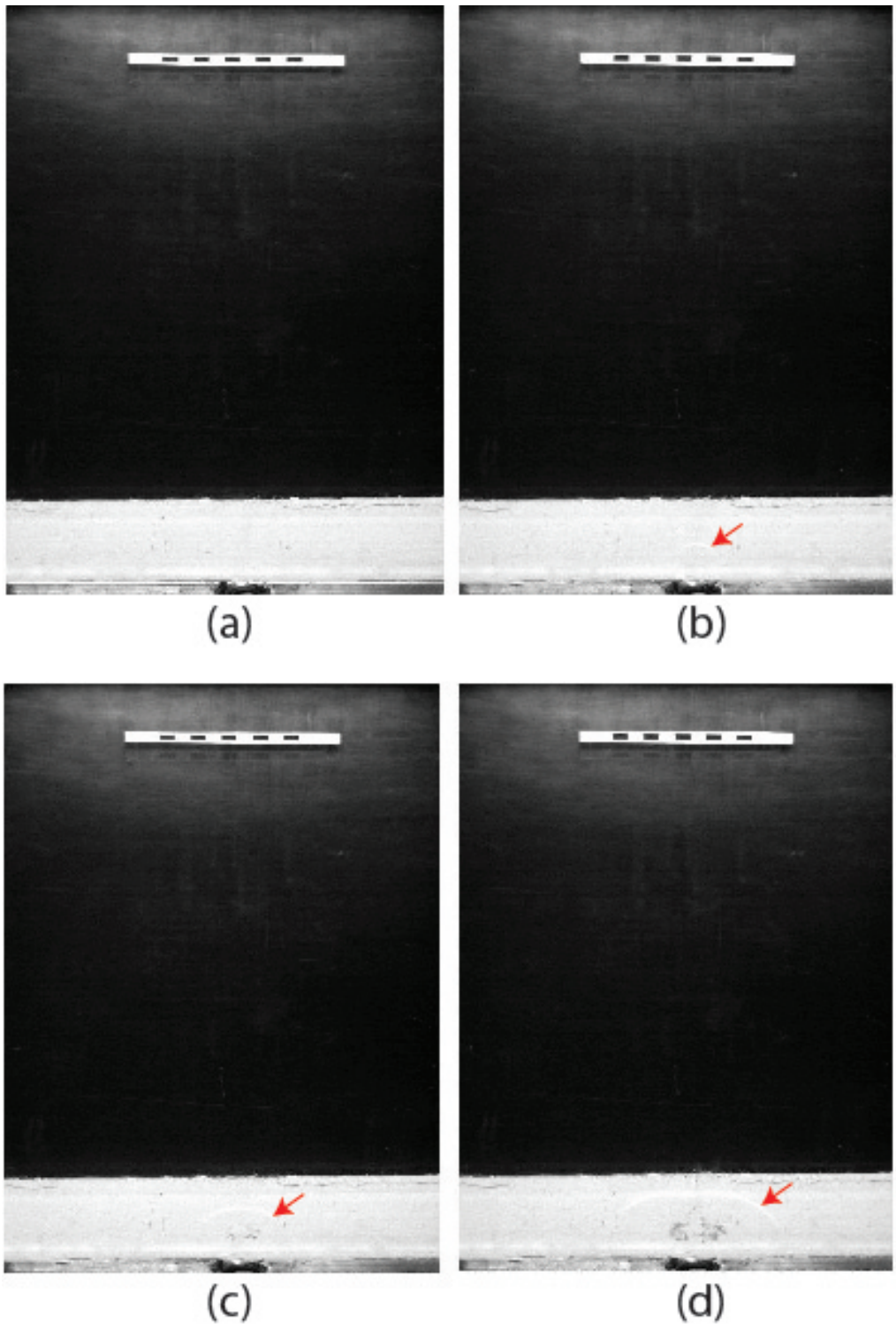

Figure 3.8: *Images of an experiments at 4 different time steps, the time increases from (a) to (d). A compaction wave is observe to propagate in the layer (indicated by the red arrow.)*

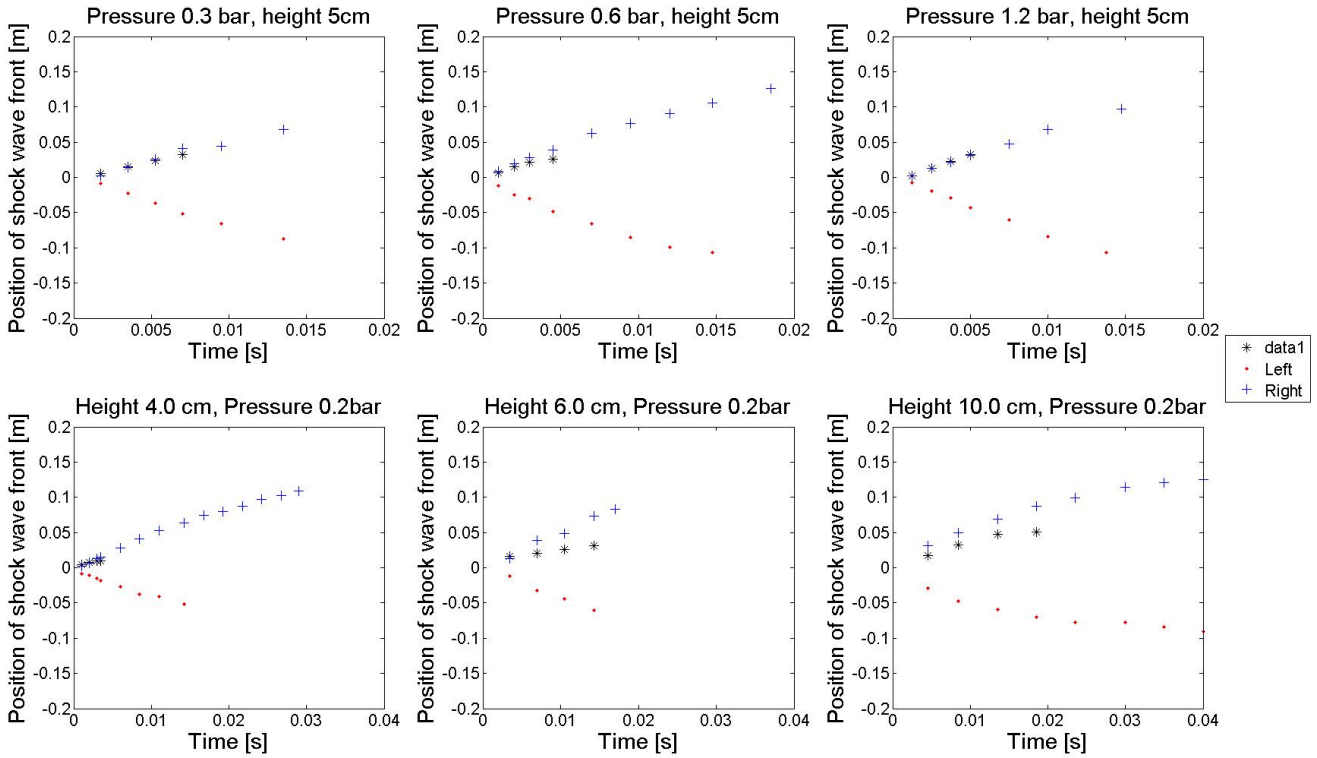

Figure 3.9: *Position of compaction wave through time. The three upper plots are from the P-series, while the three lower plots are from the H1-series.*

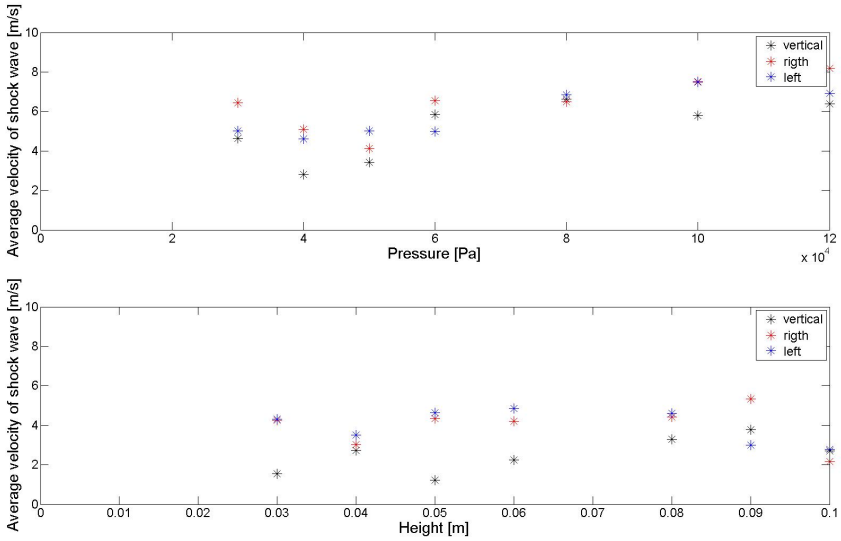

Figure 3.10: *Average velocity for compaction waves for P-series (upper) and H-series (lower)*

3.4 Image analysis

The goal of the image analysis is to be able to get the number and the sizes of the fragments through time. Using this information, it is possible to get the fragments size distribution through time for each experiment.

In figure 3.11, an example of the images from the high speed camera is given. To get the desired information, the image analysis needs to separate the fragments from the background and the dust in the images. There are several methods to do this, a classical approach is thresholding.

Thresholding

First, the images are cropped so that they only contain information that is of interest, see figure 3.12a. This is done to improve the speed of the image analysis. After the cropping, the contrast of the images is adjusted using the Matlab-function *imadjust*, which makes the bright parts of the image brighter and the dark parts darker, thus making it easier to separate the fragments from the background and the dust, see figure 3.12.

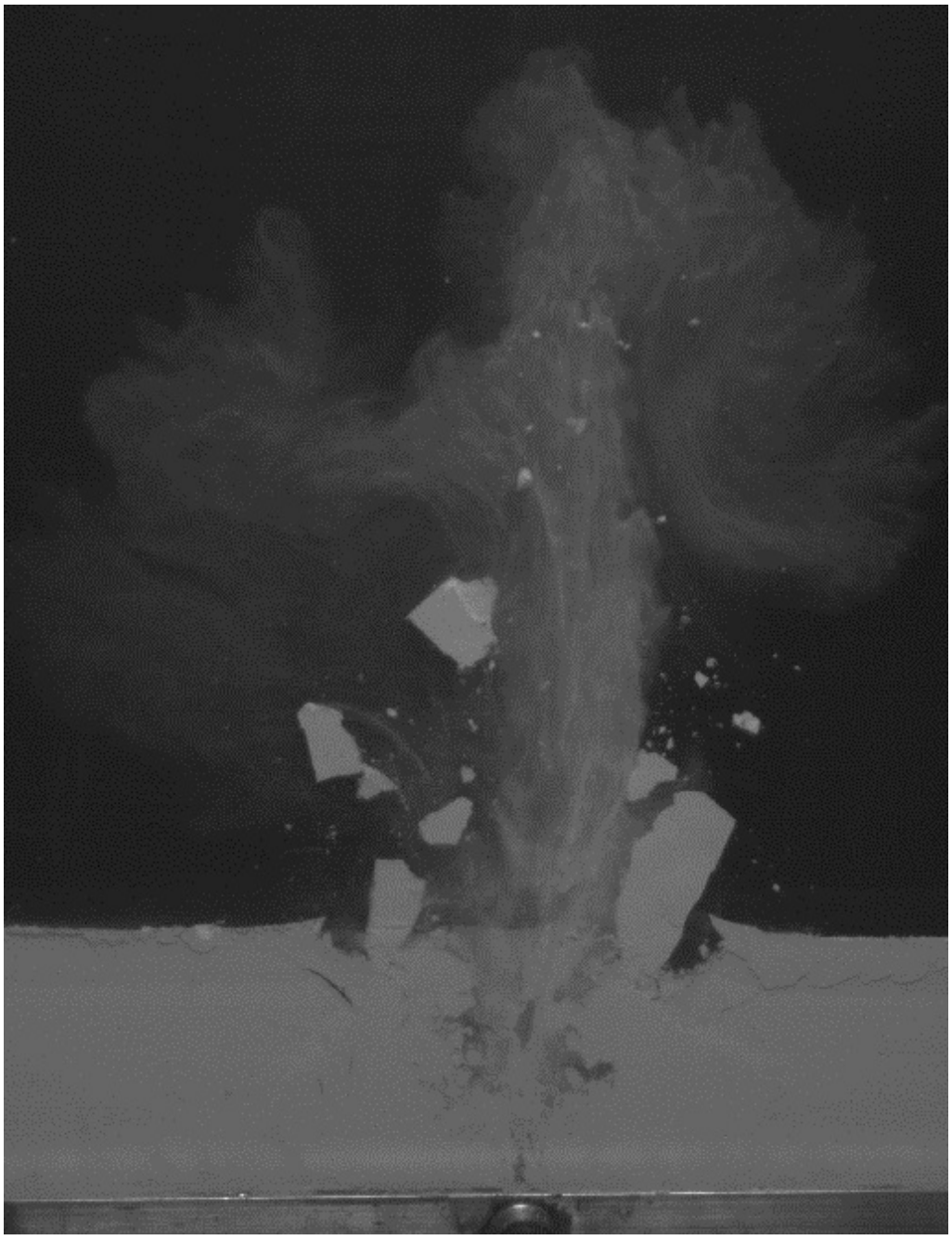

Figure 3.11: *Image from experiment*

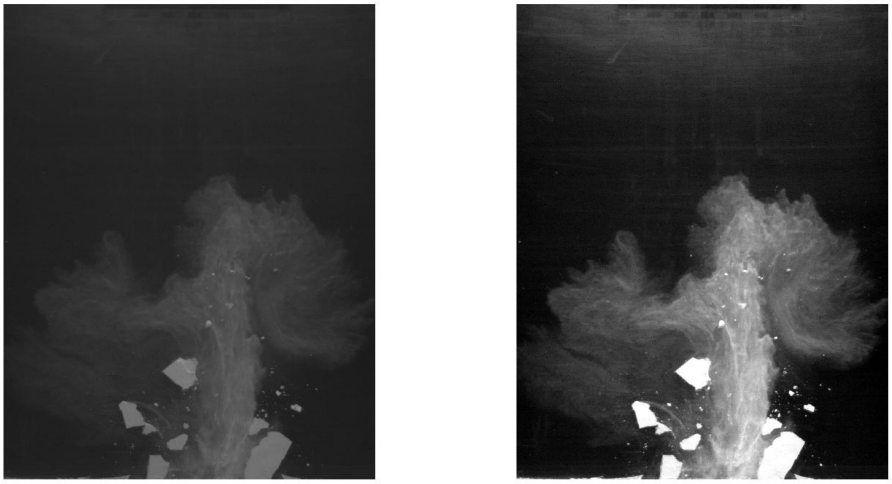

(a) Original Image **(b)** Light adjusted image

Figure 3.12: *Boost the contrast of the image by using the function imadjust in Matlab*

A greyscale image, such as figure 3.12b, is a matrix where each element in the matrix corresponds to a pixel and the value of the element gives the brightness of that pixel. The brightness in the experimental images are given by a number between 0 and 255 where 0 is totally black and 255 is totally white. In figure 3.13 the histogram of the values of the elements in the matrix of figure 3.12b is given. The histogram shows a large amount of pixels with low values, these values correspond to pixels of the dark background, the intermediate values correspond to the dust and the highest values correspond to the fragments.

Thresholding is a method where all pixels with a value higher than a specified limit is set to 1, and all pixels below this limit is set to 0. This converts the greyscale image to a binary image, i.e. only containing 0's and 1's. The idea of this method is to place the limit of thresholding so that the pixels of the fragments become 1's and the background becomes 0's. In figure 3.14 three levels of thresholding (low, medium and high) have been chosen.

The images in figure 3.14 show the consequences of choosing the wrong thresholding limit. In figure 3.14b, it can be seen that even though the

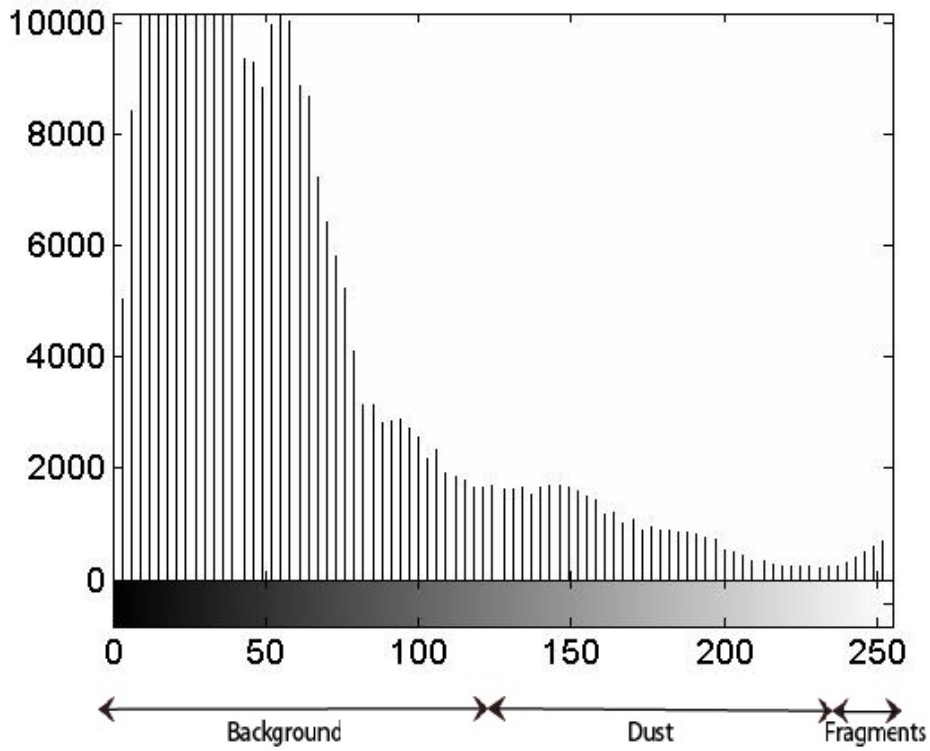

Figure 3.13: *Histogram of image*

image contains a lot of details, the thresholding limit is too low and part of the dust cloud is made white. Using a higher value for the limit, as in figure 3.14c, will make this better so that less of the dust cloud is made white, but still the thresholding is not able to fully separate the dust from the fragments. The dust and fragments can only be separated by using a very high value for the thresholding limit, as in figure 3.14d, however, the binary image from this high thresholding limit causes a high loss of details, and many small fragments are eliminated.

It becomes clear that thresholding is not a method able to separate the fragments from the background and dust and still keep the level of detail needed for a good quantitative analysis of the small fragments. Another method is needed.

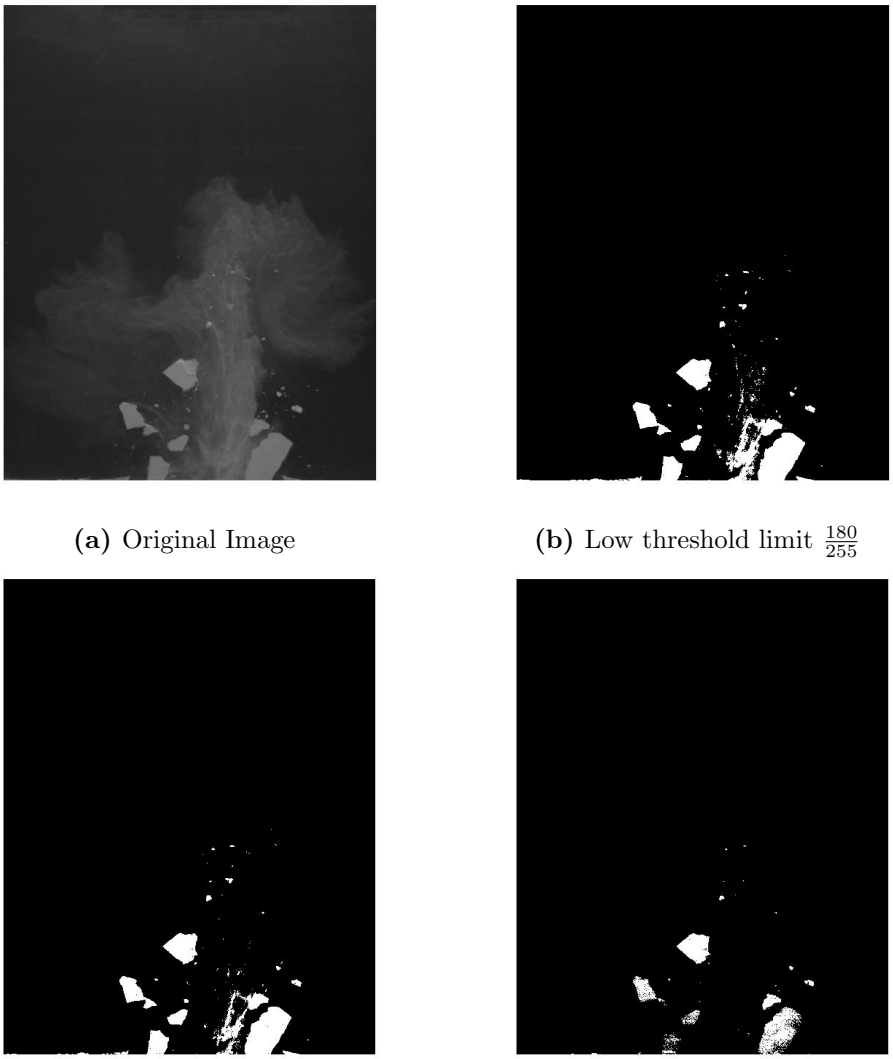

(a) Original Image

(b) Low threshold limit $\frac{180}{255}$

(c) Medium threshold limit $\frac{200}{255}$

(d) High threshold limit $\frac{250}{255}$

Figure 3.14: *Thresholding the image with different levels of thresholding*

Smoothing

Another method for separating the fragments from the background and dust is what I call smoothing. The idea of the method is shown in figure 3.15

The method utilizes a smoothing function (Smooth2.m by Hilands [2004]) to smooth out the intensity values in the image matrix. Then, by subtracting the smoothed image from the original, the fragments can be displayed as high peaks in an intensity-plot (see figure 3.15d). The final image is easy to threshold since the fragments will be shown as individual high peaks.

In figure 3.16 the resulting image from the smoothing method is given. As is seen in this figure the problem with the smoothing method is that even though it finds very small fragments, only the edges of the large fragments are recognized as fragments. This means that the smoothing method is not suited for a proper quantitative analysis for large fragments.

Combining thresholding and smoothing

Above, two methods for separating the fragments from the background and dust has been presented. It has been shown that thresholding is not a suitable method for image analysis, since it needs a thresholding limit so high that all the details from the images are lost. It has also been shown that the smoothing method is not suitable for image analysis since it is not able to detect the largest fragments.

However, the two methods can be combined, so that the thresholding gives information of the large fragments and the smoothing gives information of the small ones. From the combination of the two methods, by adding the the binary images from each method, we get the image shown in figure 3.17

Getting data from the images

Using the binary images from figure 3.17, it is possible to use the Matlab function *bwlabel* to label the different fragments. This means that each area with connected 1's will be labeled as a domain. After the image has been labeled the areas of the different domains, i.e. fragments, can be found by using the function *regionprops*.

By using *regionprops* all the data required for the quantitative analysis can be found. This means that it is possible to get the number of fragments

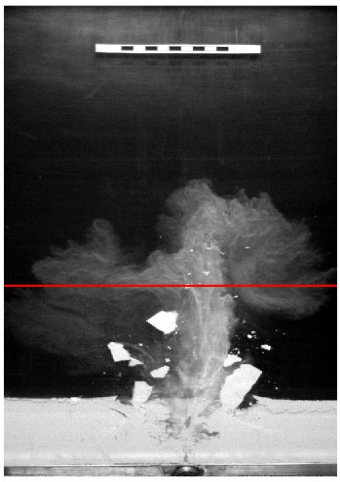

(a) Original, red line give cross section

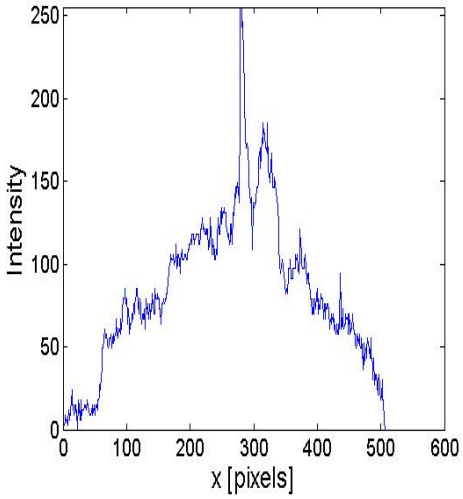

(b) Intensities for original image

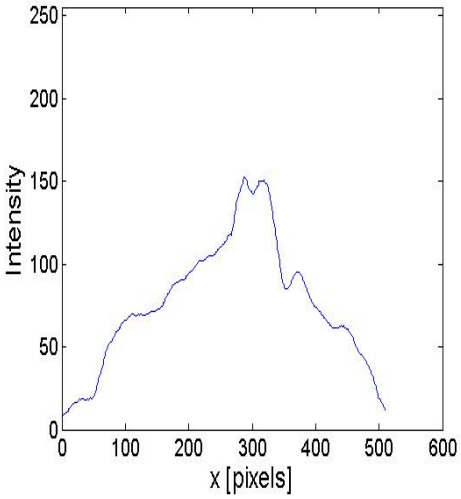

(c) Intensities for smoothed image

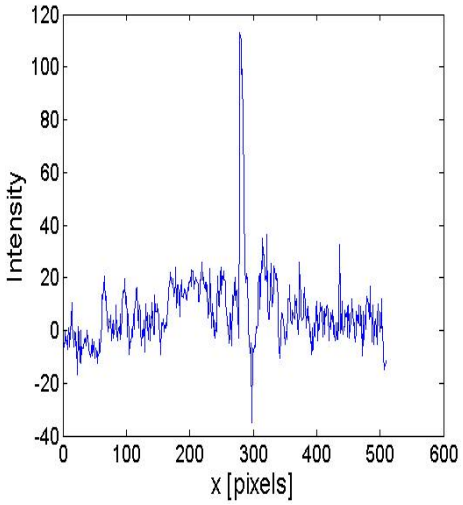

(d) Original + smoothed

Figure 3.15: *This figure shows the idea behind the smoothing method. (a) The original picture, the red line is a cross section of the image. (b) The intensities from the cross section of the red line in (a). The peak in intensity corresponds to the small fragment in the middle of the red line. (c) The intensities are smoothed using a smoothing function (Smooth2.m by Hilands [2004]). (d) The smoothed values are subtracted from the original intensities. The results is a high single peak corresponding to the fragment. Using this final plot it is easy to threshold the image in order to separate the fragments from the background and dust.*

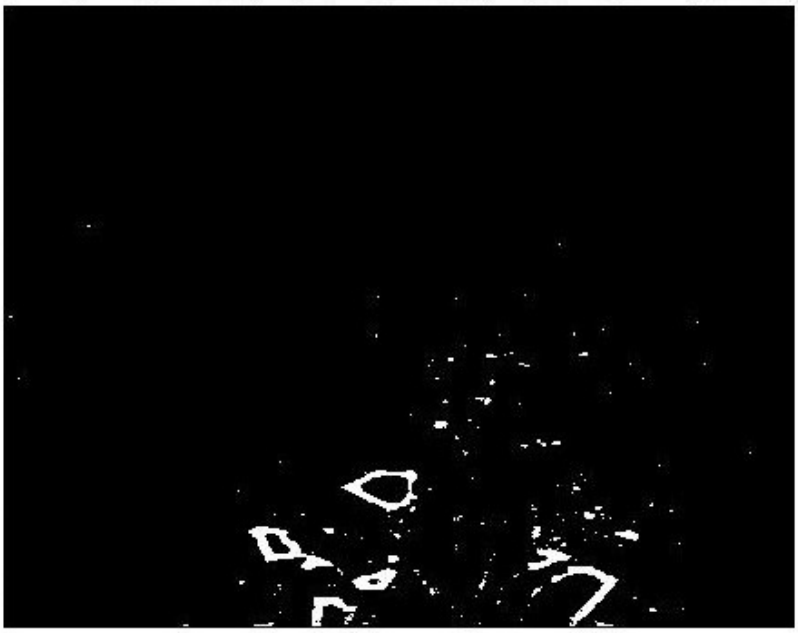

Figure 3.16: *Binary image obtained by the smoothing method. The image shows many of the small fragments, however, the function is not able to identify the large fragments.*

and the size of each fragment for each image during the experiment. The sizes of the fragments obtained from the image analysis are given in pixels, which are converted into cm^2 by multiplying the area of a pixel. The area of a pixel is found by measuring how many pixels there are along the 10cm scale which is placed on the cell (see section 3.1).

From this information I can calculate how the average size of fragments evolve through time, and find the fragment size distribution for each time step. The fragment size distribution is found by calculating the number of fragments that are larger than a given size. The fragment size distribution of the image in figure 3.11 is given in figure 3.18. The data has been plotted in a log-log plot. As is seen in this figure the data points can be well approximated by a power law distribution, which is in general true

Figure 3.17: *Black and white image obtained by adding thresholding and smoothing*

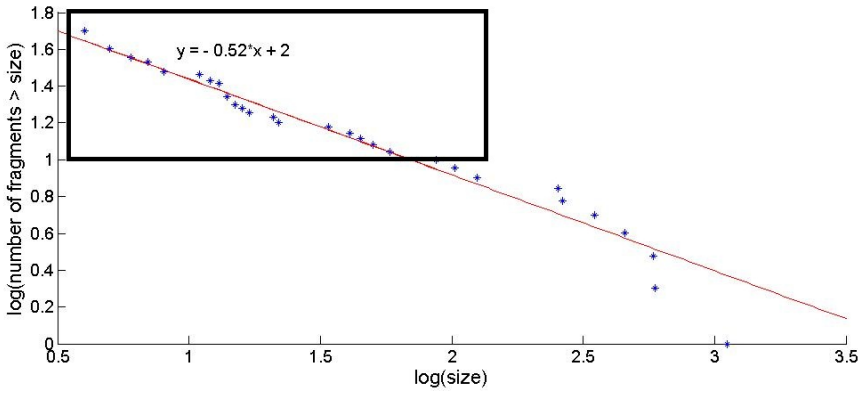

Figure 3.18: *log-log plot of the fragment size distribution of figure 3.11, a line is fitted to the data points inside the black box. The slope of the line is the exponent, D, of the power law distribution.*

for all my experiments. It is therefore possible to fit a line to the data points, where the slope of the line is the exponent, D, of the power law (see section 2.1). When fitting the line to the data points, all fragments of an area smaller than 4 pixels are ignored since these may be caused by noise in the image. Also all data points with a cumulative value less than 10 are ignored, since they mainly correspond to the large fragments which are not approximated by a power law (see figure 3.18).

Since I approximate the fragment size distributions with a power law, I can store the value of the exponent, D, for each time step, and use this to study the time evolution of the fragments size distribution for each experiment.

3.5 Quantitative results

In this section, results from the image analysis are given. The pressures and the heights referred to in this section are the initial pressure in the pressure tank and the height of the powder in the cell, respectively. The image analysis is stopped when a fragment leaves the frame. The reason for this can be seen in figure 3.19. As is seen in this figure, the image analysis will only count the fragments which are in the field of vision. This means that when a fragment leaves the frame it is no longer counted, even though

it is still in the air. This leads to a bias in the results.

P-series

In the P-series the height of the powder was held constant at 5cm while the pressure was systematically varied between $0.5 \cdot 10^4$ Pa and $12 \cdot 10^4$ Pa. From the image analysis presented in section 3.4 the number of fragments through time can be found. In figure 3.20 this is plotted for each experiment in P-series. In all of these experiments, except for the first one ($0.5 \cdot 10^4$ Pa), the number of fragments can be seen to increase with time. For the experiments with $1 \cdot 10^4$ Pa and $2 \cdot 10^4$ Pa the number of fragments first increases, and after a maximum is reached the number of fragments drops. The drop corresponds to fragments falling down onto the surface of the layer. For the experiments in the P-series with a pressure above and equal to $3 \cdot 10^4$ Pa it can be observed that the number of fragments saturates after some time.

In figure 3.21 the average size of the fragments through time for the different experiments of the P-series is given. For all the experiments, except for the first one ($5 \cdot 10^3$ Pa), the average size can be seen to decrease with time. For the experiments with a pressure above or equal to $1 \cdot 10^4$ Pa, the average size can be observed to saturate after some time.

Figure 3.22 shows the absolute value of D through time for each experiment in the P-series. In general it can be seen that the D-value increases with time. It can be observed that the D-values for pressure higher than or equal to $1 \cdot 10^5$ Pa saturate in time.

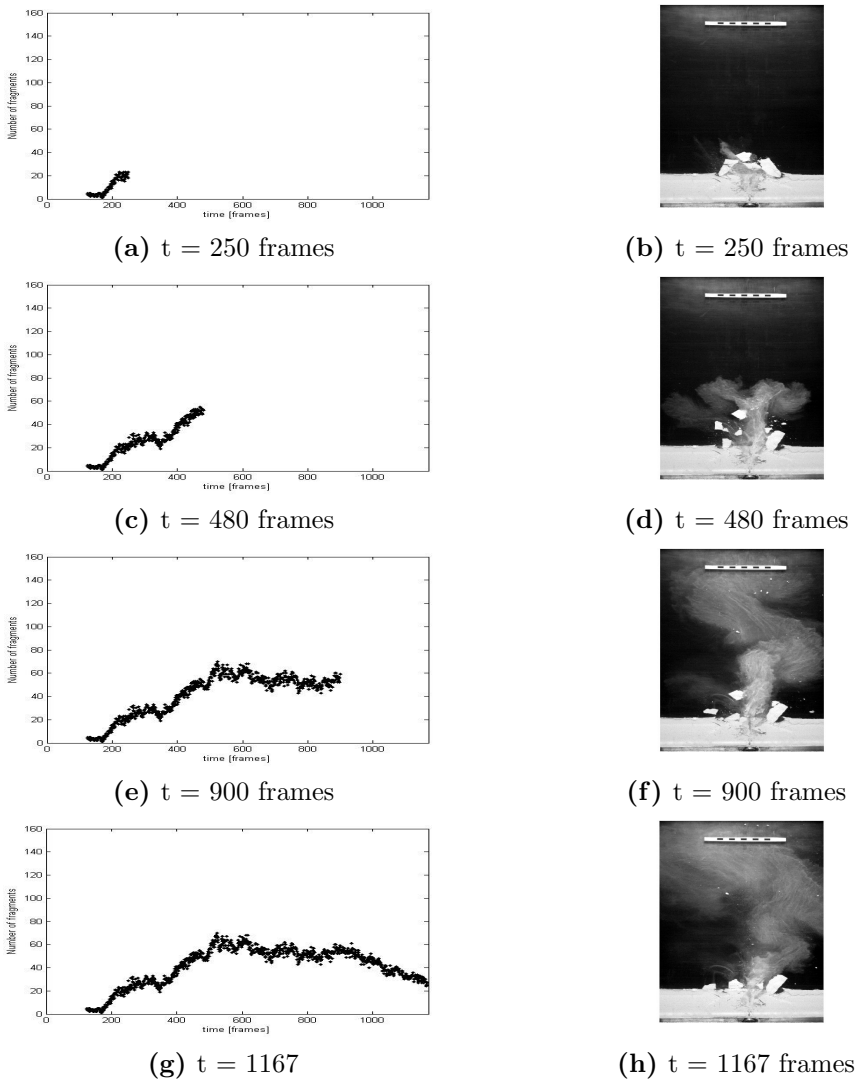

(a) t = 250 frames **(b)** t = 250 frames

(c) t = 480 frames **(d)** t = 480 frames

(e) t = 900 frames **(f)** t = 900 frames

(g) t = 1167 **(h)** t = 1167 frames

Figure 3.19: *The left column shows the number of fragments in the experiment through time. The right column shows the image from the experiment corresponding to the last time step in the plot to its left. This figure shows why it is important that the image analysis is stopped at the point where fragments start to leave the frame since this causes the number of fragments to appear to decrease even though they have only left the field of vision.*

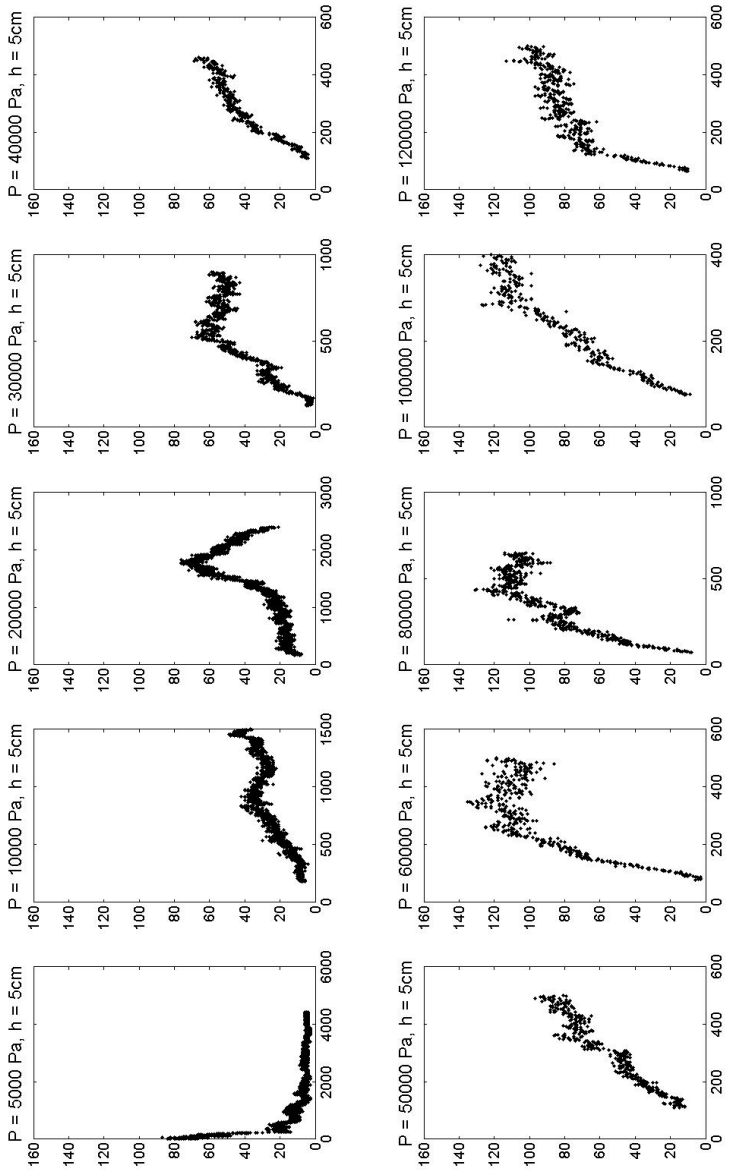

Figure 3.20: *Number of fragments for P-series. In all the experiments, except for* $5 \cdot 10^3$ *Pa, the number of fragments increases with time. For pressures above and equal to* $1 \cdot 10^4$ *Pa the number of fragments can be observed to saturate after some time.*

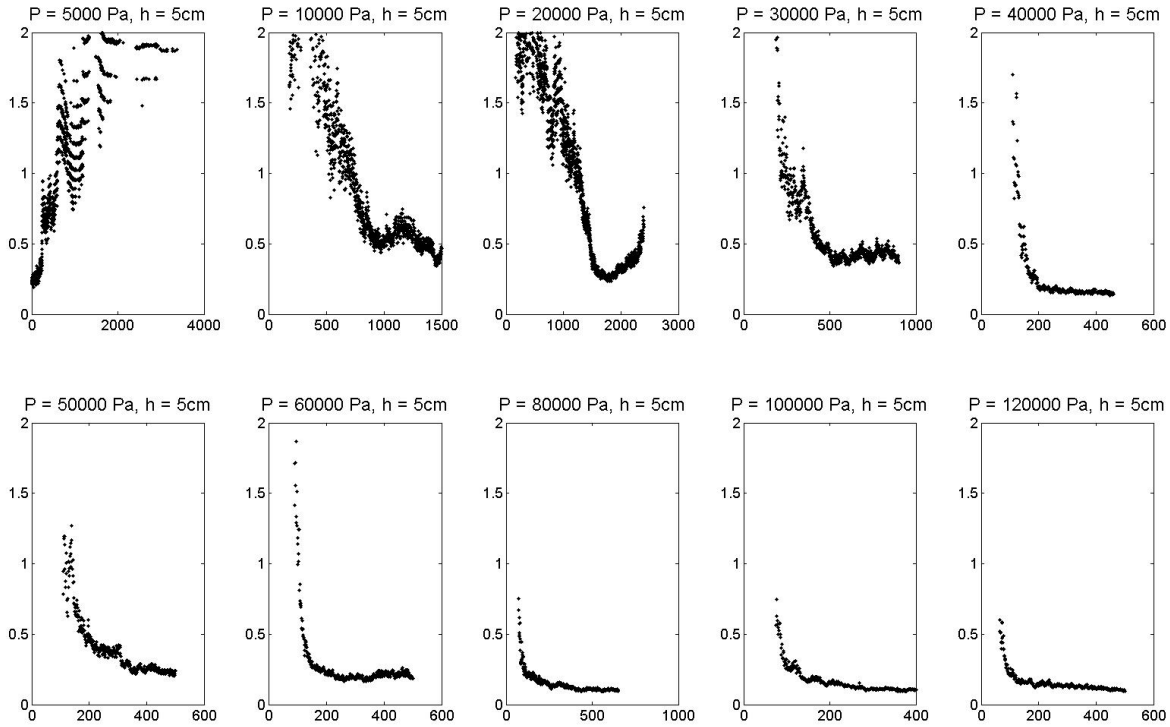

Figure 3.21: *Average size of fragments for P-series*

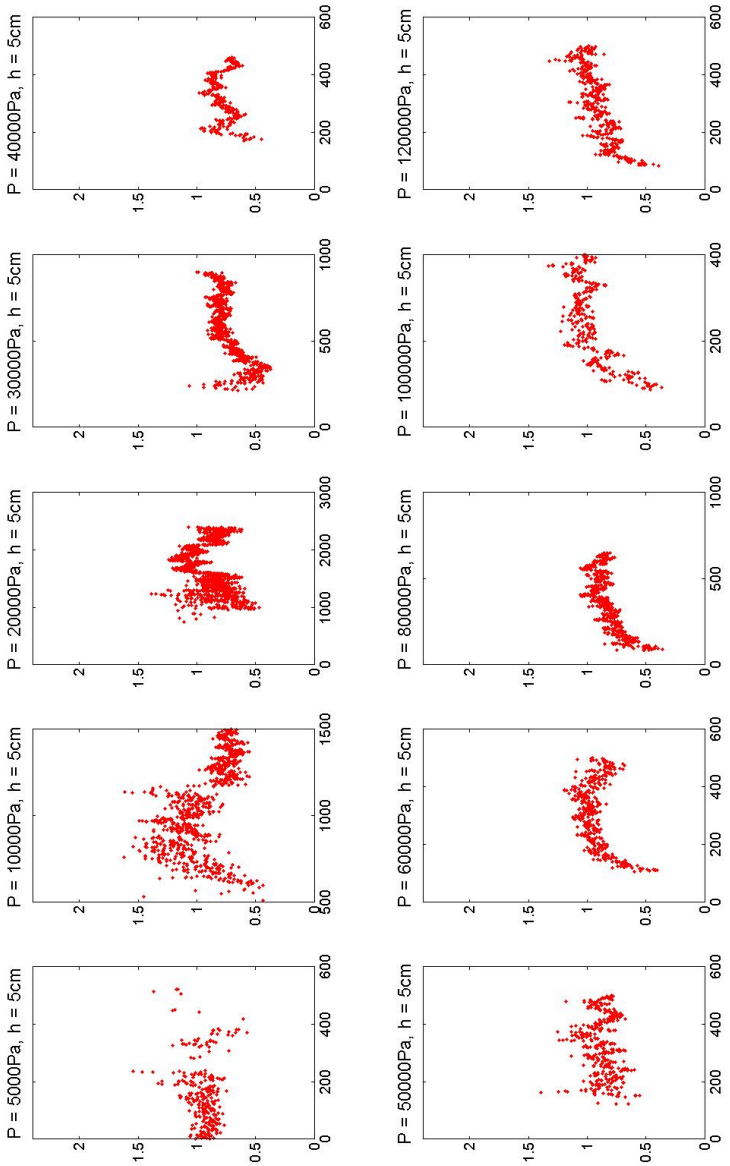

Figure 3.22: *D-values for P-series*

H1 and H2 series

In the H1 and the H2 series the pressure in the pressure tank was held constant at $0.2 \cdot 10^5$ Pa and $0.8 \cdot 10^5$ Pa, while the height of the powder was systematically varied between $1 - 10$ cm and $1 - 13$ cm, respectively.

In figure 3.23 and 3.24, the number of fragments through time is plotted for these series. For both plots the number of fragments can be seen to increase with time, but in contrast to the number of fragments plots for the P-series, the plots for the H1 and the H2-series do not show any systematic saturation after some time.

The average size of fragments in the H1 and the H2 series are presented in figures 3.25 and 3.26, respectively. In contrast to the P-series, the average size of fragments in the H1-series does not show any systematic saturation. This is, however, seen for the H2-series.

The D-values through time in series H1 and H2 are given in figure 3.27 and 3.28, respectively. In general it can be seen that the D-values increase with time. However, the D-values for these series of experiments do not show any systematic behavior as was seen for the P-series.

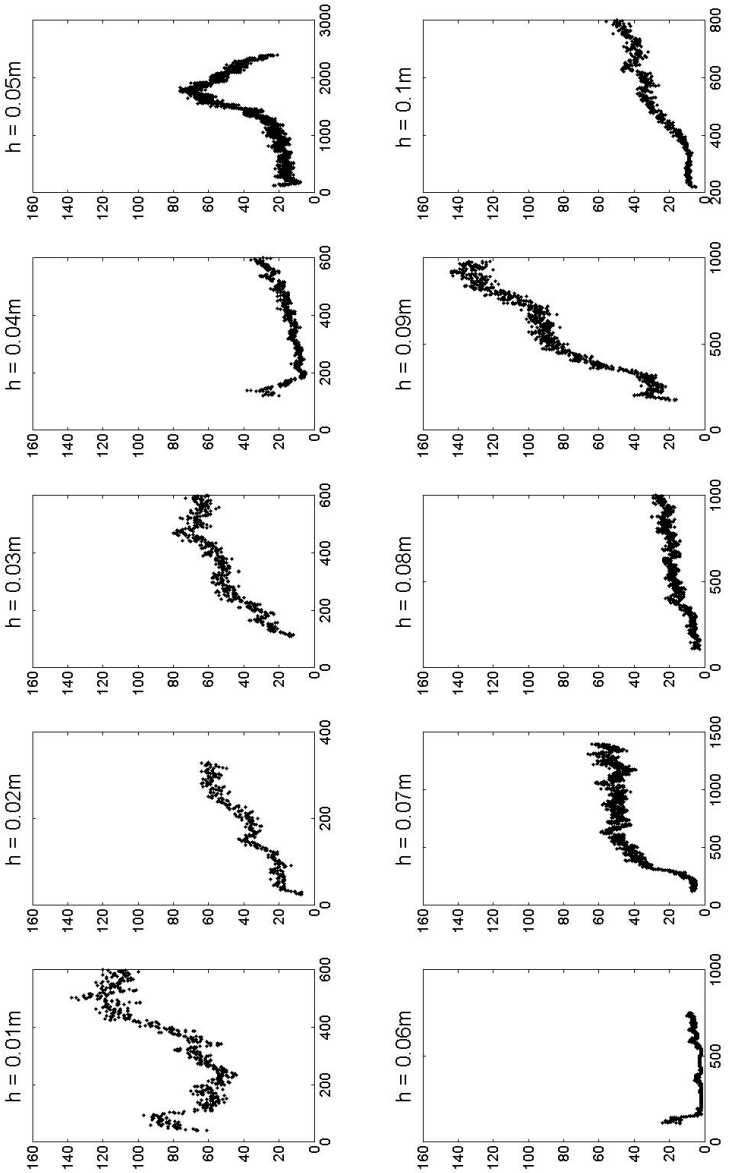

Figure 3.23: *Number of fragments for H-series, constant pressure of* $2 * 10^4 Pa$

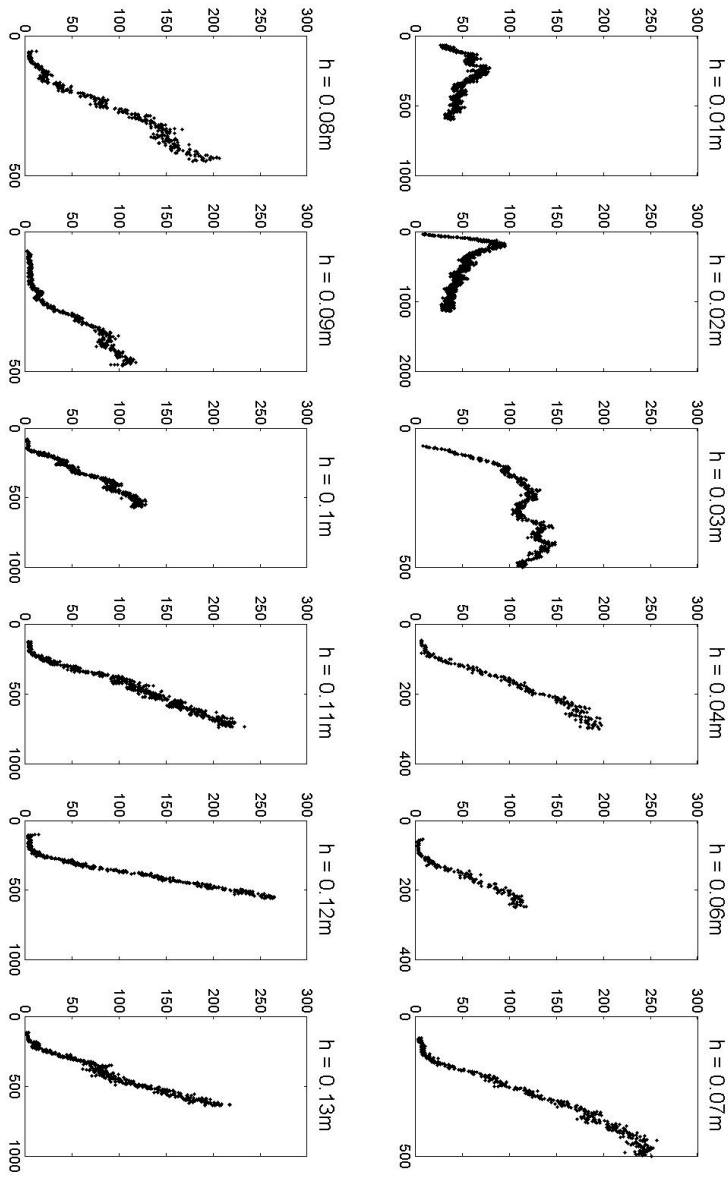

Figure 3.24: *Number of fragments for H2-series, constant pressure of* $8 * 10^4 Pa$

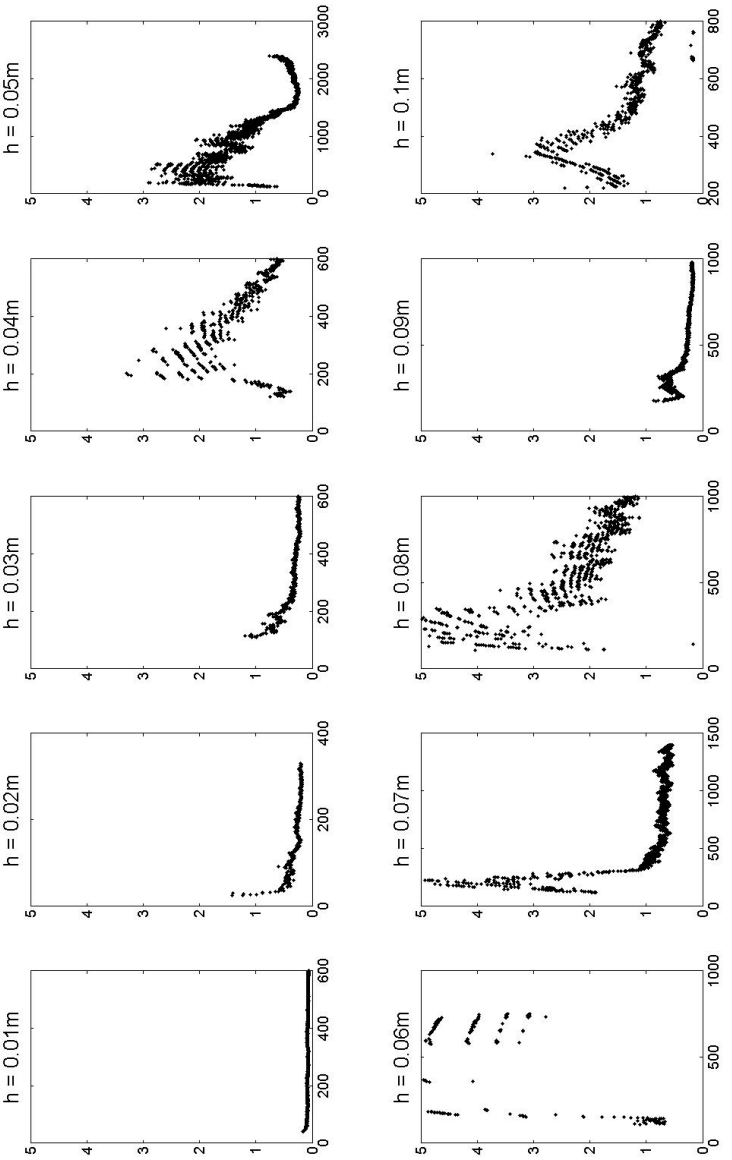

Figure 3.25: *Average size of fragments for H-series. Pressure* $= 0.2 \cdot 10^5$ *Pa*

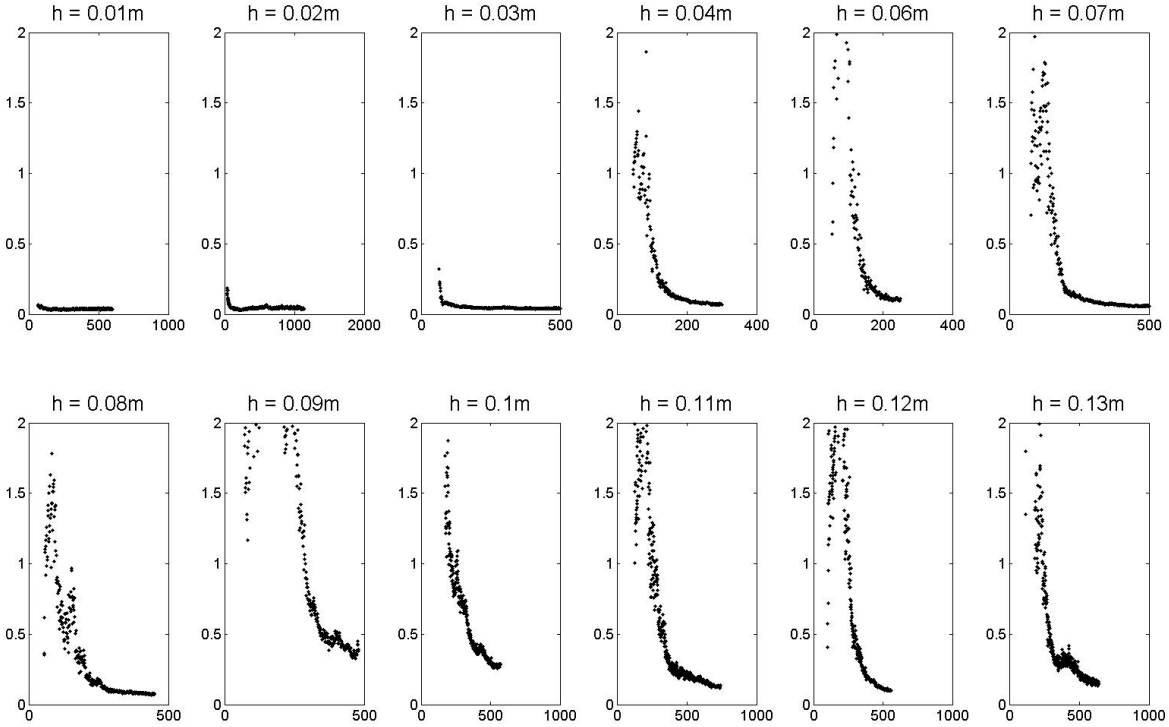

Figure 3.26: *Average size of fragments for H2-series. Pressure* $= 0.8 \cdot 10^5$ *Pa*

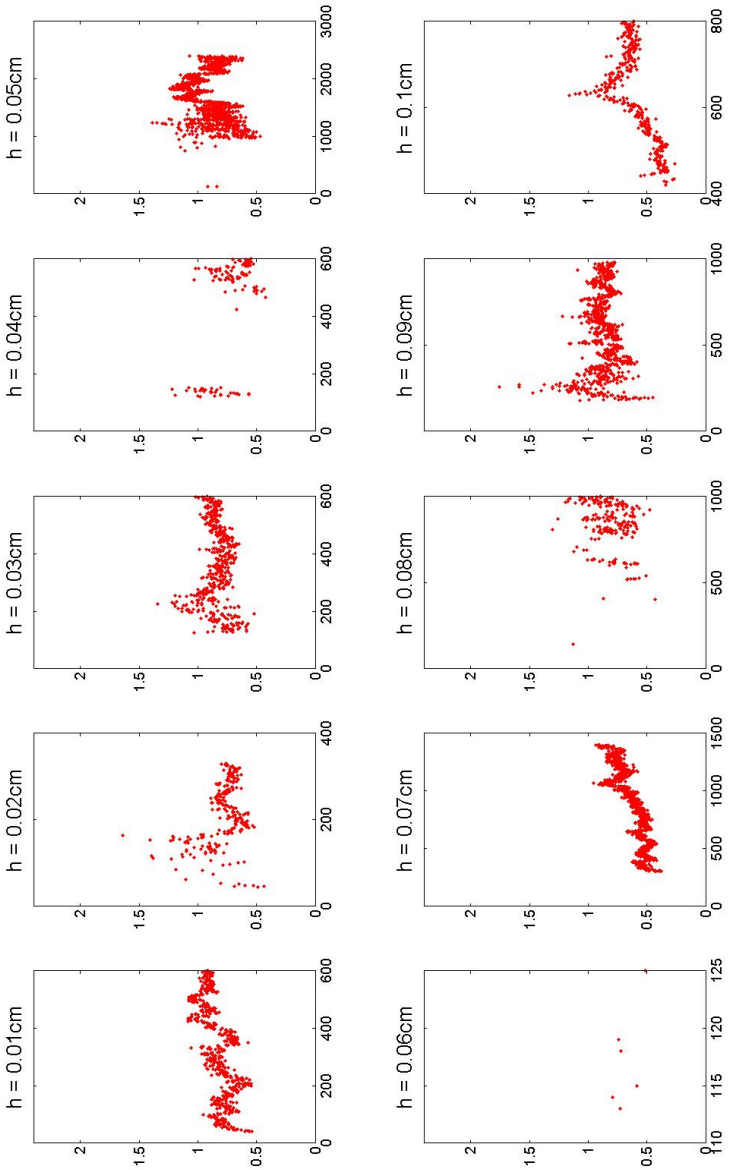

Figure 3.27: *D-values for H1-series. Pressure* $= 0.2 \cdot 10^5$ *Pa*

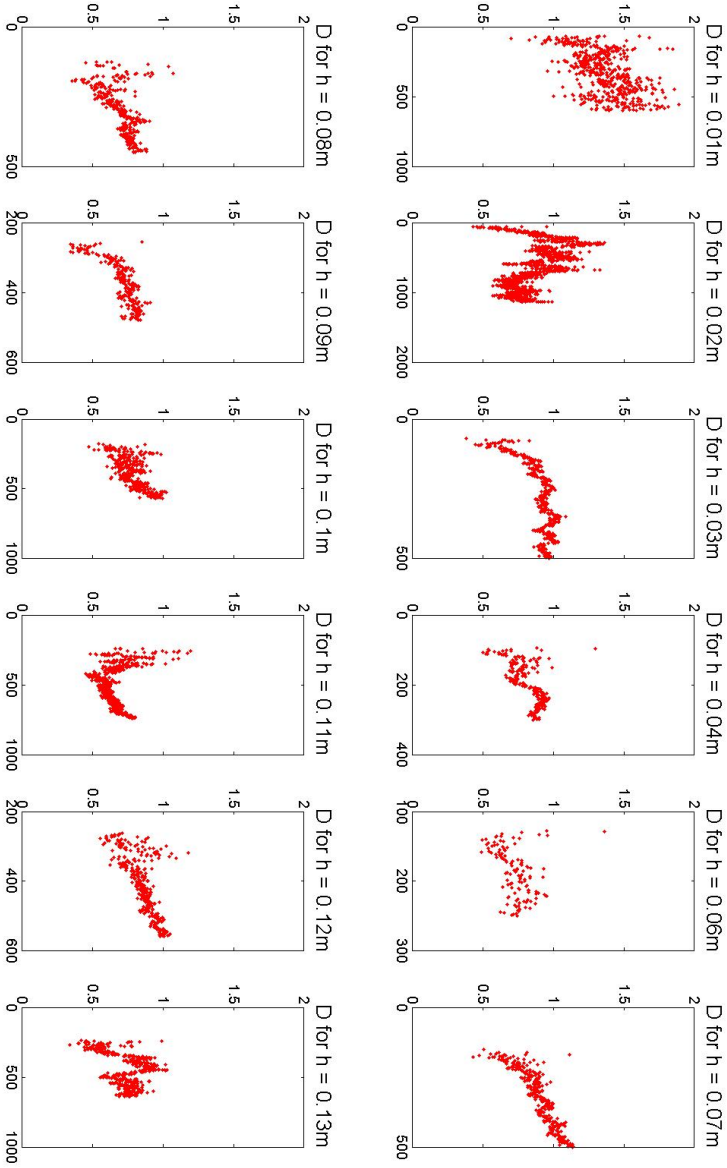

Figure 3.28: *D-values for H2-series. Pressure* $= 0.8 \cdot 10^5$ *Pa*

Chapter 4

Interpretation and discussion

4.1 Observational results

Two regimes

In section 3.3 it was observed that the morphologies of the experiments are dependent on the pressure (P) and the height (h) of the layer. It seems, therefore, reasonable to claim that the morphology is controlled by the ratio of these two parameters,

$$a = \frac{Pressure}{height} = \frac{P}{h}. \tag{4.1}$$

This would mean that the boundary between the domains (see figure 3.6) follow a line of constant slope given by a. By dividing by the gravitational acceleration, g, and the density of the powder, ρ, this ratio is made dimensionless. This will not change anything else than the value of the ratio, since g and ρ are constant in my experiments.

$$a = \frac{Pressure}{density * gravity * height} = \frac{P}{\rho g h} \tag{4.2}$$

To test this hypothesis I calculated the ratio given in equation 4.2 using the values of the parameters used in my experiments. The results are given in table 4.1

The results show that for large ratios ($a > 110$) we get channeling and for low ratios ($a < 60$) we get lift off. For ratios in between ($65 < a < 97$) we can get both, so this is likely a transitional phase.

The fact that there is a finite interval for the transition between the phases, i.e. that there is not a sudden change but an interval of values giving both phases, suggests that my representation in the phase diagram, figure 3.6, is too simplistic. There is not an abrupt change in regime, but a more continuous change. Another reason might be due to preparation of the experiments. Even though the density of the layer is controlled (see section 3.1), it was observed that during compaction some of the powder was not compacted. This might lead to a lower density than the desired value. In a critical point, between the two regimes, such an instability might contribute to the randomness seen for a-values between 65 and 97.

That the system is controlled by the ratio between P and ρgh is no surprise, since ρgh is the lithostatic pressure of the powder. That is, the system ends up being controlled by the excess of pressure above lithostatic pressure.

This means that for high enough pressures, compared to the weight of the layer, the momentum of the gas hitting the powder is so high that the gas effectively does not feel much resistance and blows straight through the layer. For lower pressures, however, the resistance caused by the weight of the layer is high enough so that the air really feels resistance from the layer and is not able to blow straight through. Instead, it opens fractures propagating towards the surface at an oblique angle.

In section 3.1 the lift off regime was described and illustrated (see figure 3.4). The images in figure 3.4 show that for a relatively thick layer only the upper part of the layer is lifted up. It is observed that on two occasions lateral fractures are formed. These lateral fractures are probably made in the same manner as the two fractures that eventually separate the part that is lifted up. However, they are formed so deep in the layer that the weight of the overlying material is too great for them to propagate toward the surface.

Table 4.1: *Morphology vs a*

Experiment	a	Morphology
H2	777	I
H2	389	I
H2	259	I
P	233	I
P	194	I
H1	194	I
H2	194	I
P	155	I
H2	129	I
P	116	I
H2	110	I
*	*	*
H1	97	I
H2	97	I
P	97	V
H2	86	I
P	78	V
H2	78	V
H2	71	V
H1	65	I
H2	65	I
*	*	*
H2	60	V
P	58	V
H1	49	V
P	39	V
H1	39	V
H1	32	V
H1	28	V
H1	24	V
H1	22	V
P	19	V
H1	19	V
P	10	V

Compaction waves

In figure 3.10 the velocities of the compaction waves are given. This figure shows that the velocity of the wave is depending neither on the height nor the pressure. This suggests that the wave velocity is determined by material properties, or is a material property by itself.

4.2 Comparing morphologies with quantitative results

By observation of the experimental images it can be seen that an experiment that has a lift off morphology will in general produce a few large fragments, whereas an experiment with channeling will produce many small fragments (see figure 3.3). This suggests that the fragmentation is dependent on the morphology.

P-series

In section 3.5 it was observed from figure 3.20 that the number of fragments increases with time for all experiments except the experiment with a pressure of $0.5 \cdot 10^4$Pa. The difference in this experiment can be explained by looking at the binary images produced by the image analysis. Two binary images from this experiment are presented in figure 4.1. These images show that for this experiment the pressure is too low to cause any fragmentation. Therefore, this experiment will not be considered in the quantitative analysis.

It was also observed that for all experiments with a pressure above or equal to $3 \cdot 10^4$Pa the number of fragments saturates in time. This means that the production of new fragments has stopped, and that all fragments are in the air and counted by the image analysis. The saturation level represents the total number of fragments produced in the experiment. By calculating the average value of number of fragments at the saturation level for each experiment it is possible to study the total number of fragments for varying pressures. The result of this is given in figure 4.2. For the experiments with no saturation ($1 \cdot 10^4$Pa and $2 \cdot 10^4$Pa) the total number of fragments can be estimated from the peak in number of fragments, see figure 3.20. This last assumption can be justified since it was observed in

(a) t = 0.1sec

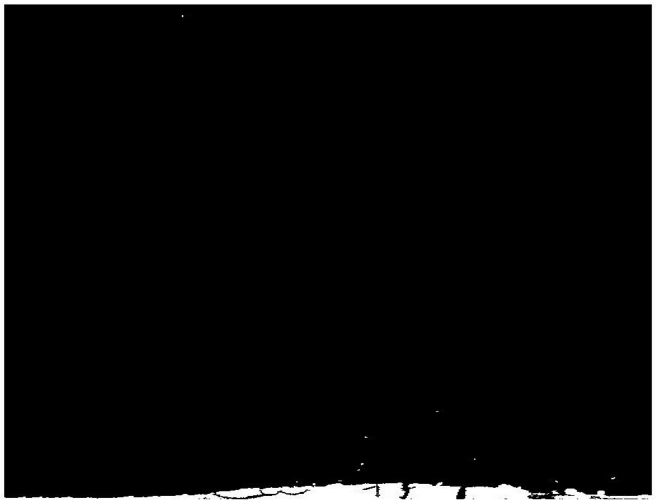

(b) t = 0.25sec

Figure 4.1: *Binary image of experiment with a pressure of* $0.5 \cdot 10^4 Pa$. *Only few fragments are produced. This shows that the pressure in this experiment is too low to cause any fragmentation, and a quantitative analysis of this is meaningless.*

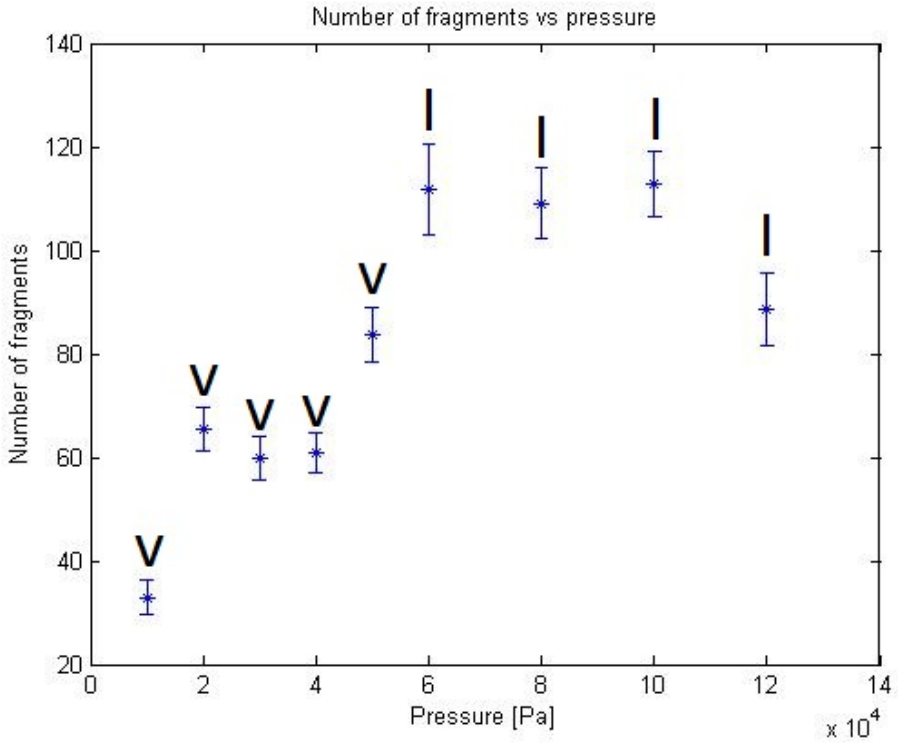

Figure 4.2: *Total number of fragments compared with initial pressure in the tank estimated from the saturation levels from figure 3.20. The error bars represents the standard deviation of the spread around the average value at the saturation level. Above each point the morphology of that experiment is superimposed, V represents liftoff and I represents channeling.*

section 3.5 that this peak corresponds to the point where all the fragments produced are still in the air, and the fall afterwards was due to the fragments falling back down onto the surface of the layer.

Figure 4.2 shows that the total number of fragments initially increases with increasing pressure, for pressures above $6 \cdot 10^4$Pa the number of fragments is more or less constant except for the highest pressure ($12 \cdot 10^4$Pa) where the number of fragments has decreased somewhat.

Comparing the total number of fragments given in figure 4.2 for each experiment with its morphology it can be observed that for the experiments within the lift off regime the number of fragments increases with increasing

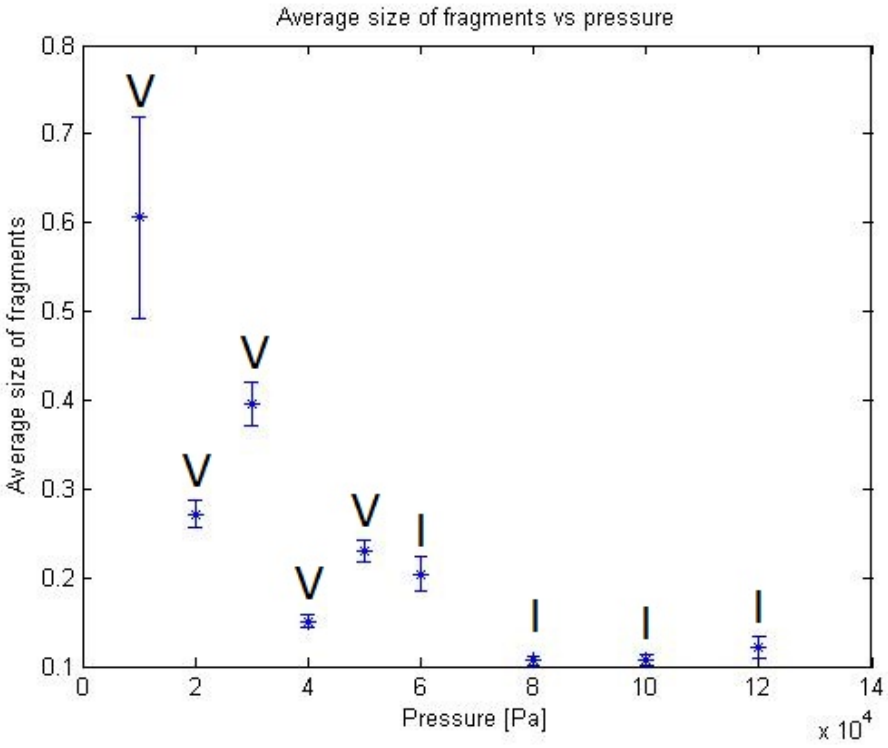

Figure 4.3: *Final average size of fragments (in cm^2) estimated from the saturation level in figure 3.21. The error bars represent the standard deviation of the spread around the average value at the saturation level. Above each point the morphology of that experiment is superimposed, V represents liftoff and I represents channeling.*

pressure, while for experiments that are within the channeling regime the production of fragments is more or less constant.

Similar to the number of fragments the average size of fragments shows a saturation in time (see figure 3.21). Therefore, the final average size from an experiment, can be estimated from the saturation level. In figure 4.3 the final average size is presented in comparison with the pressure used in the experiments, in addition the morphology of the experiment is superimposed. This figure shows that the average size of fragments decreases with increasing pressure. For pressures equal or above $8 \cdot 10^4$Pa the average size is more or less constant.

By comparing the final average size as presented in figure 4.3 and the morphologies, no clear relationship can be seen. Even though the experiments with the three highest pressures ($8 \cdot 10^4$Pa, $10 \cdot 10^4$Pa and $12 \cdot 10^4$Pa) seem to have a more or less constant average size, the first experiment showing channeling ($6 \cdot 10^4$Pa) has a larger average size than the one with $4 \cdot 10^4$Pa, even though this is in the lift off regime.

Figures 4.2 and 4.3 show that the number of fragments increases and the final average size of fragments decreases with increasing pressure. This observation may not be that surprising, since increasing pressure represents a higher energy input which means that more surface can be created. However, it can be seen that the production of fragments does not go above 120 fragments, even though the pressure is increased. This apparent maximum of number of fragments is likely to be the result of the resolution of the images, this is discussed in more detail below.

If we consider the average size of fragments and the observation that there is a maximum of 120 fragments, it can be observed that the average size is not constant once this number of fragments is achieved. This means that even though the same number of fragments are produced, the sizes of those fragments are smaller. This can especially be seen in the experiment with $12 \cdot 10^4$Pa, where the number of fragments is even less than the maximum of 120 but the average size is small. This suggests that the sizes of the fragments decrease with increasing pressure, even though the number of fragments apparently does not increase.

H1-series

In figure 3.23 the number of fragments through time for the H1-series was presented. Similar to the experiment of the P-series with a pressure of $0.5 \cdot 10^4$Pa the experiments with a height of 6.0cm and 8.0cm in the H1-series show almost no fragmentation, and a quantitative analysis is therefor meaningless. These experiments will therefore be ignored in this section.

Even though it was observed in section 3.5 that there was no systematic saturation in time for the H1-series, the total number of fragments can be estimated by the peaks in the plots in figure 3.23. This assumption should not cause any problems since the peaks represent the point where all the fragments produced are in the air. The decrease of fragments after the peak is again caused by the fragments falling back to the surface. The result of this analysis is given in figure 4.4.

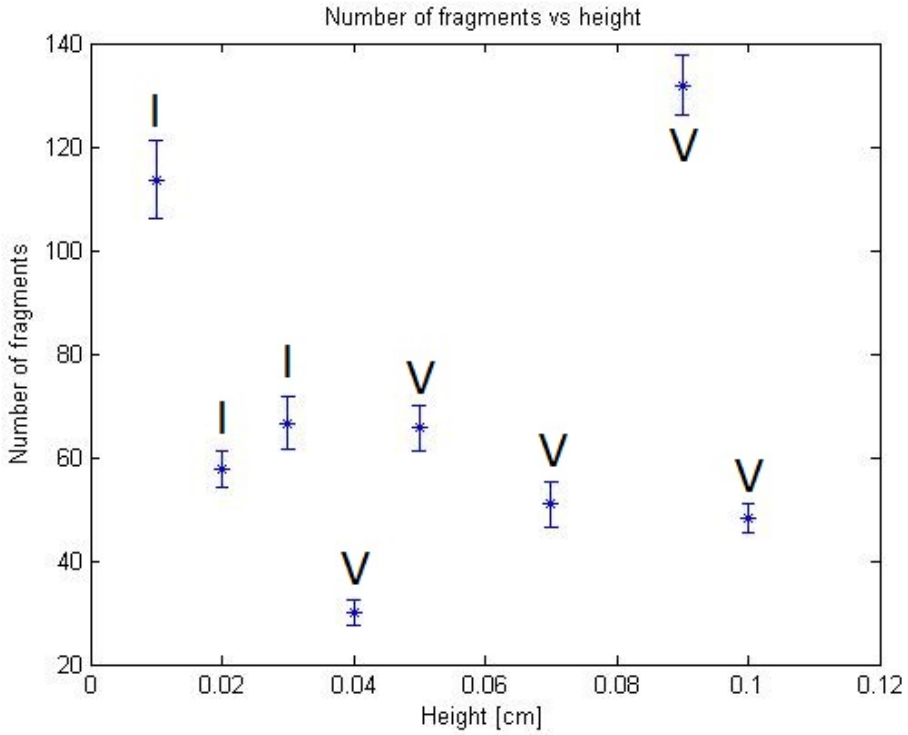

Figure 4.4: *Total number of fragments compared with height of powder estimated from the saturation levels from figure 3.23. The error bars represent the standard deviation of the spread around the average value at the saturation level. Above each point the morphology of that experiment is superimposed, V represents liftoff and I represents channeling.*

Figure 4.4 show that the number of fragments is more or less random compared with the height.

A similar analysis can also be done for the average size of the fragments. The result is given in figure 4.5. The figure shows that there is a tendency for the average size to increase with increasing height of the layer. However, the layer-thickness of 9cm is an exception as it shows an average size smaller than for layer-thickness 7cm and 10cm. There is no correlation between the average size and the morphology.

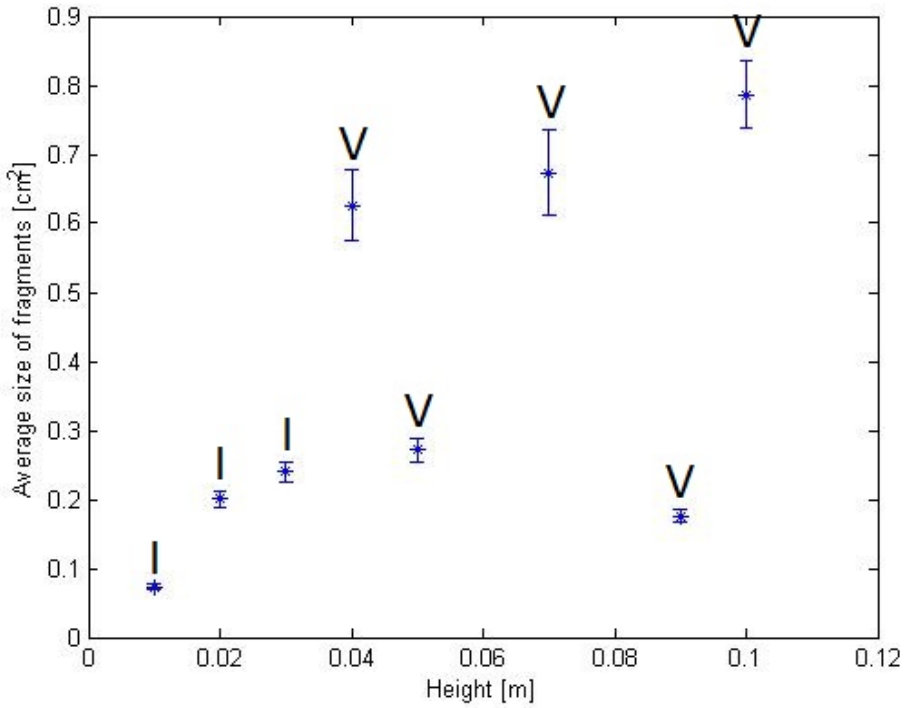

Figure 4.5: *Final average size of fragments compared to the height of powder estimated from the saturation levels from figure 3.25. The error bars represent the standard deviation of the spread around the average value at the saturation level. Above each point the morphology of that experiment is superimposed, V represents liftoff and I represents channeling.*

H2-series

It is not possible to do a meaningful analysis for the H2-series. This is because the camera was placed closer to the cell during these experiments, which caused the fragments to leave the frame before the production of fragments was finished, so that no saturation can be seen. The lower limit for the number of fragments can be estimated, see figure 4.6.

This data set does not show the total number of fragments produced in the experiment. However, a remarkable large number of fragments can be observed. Especially the three experiments with the highest height (11cm, 12cma and 13cm) produced ca. 200 to 250 fragments. By observing fig-

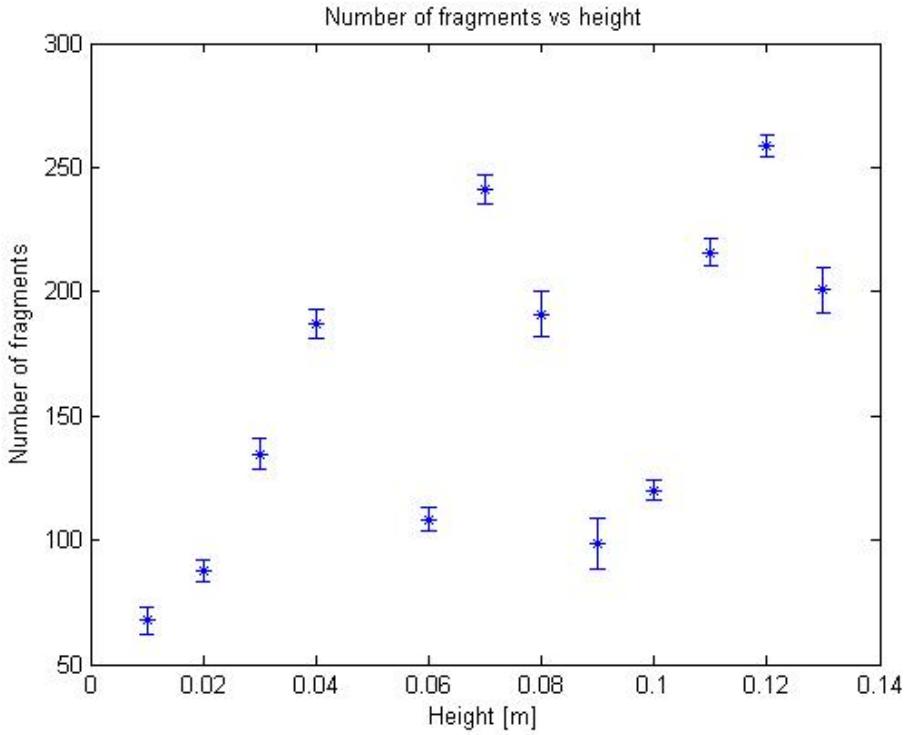

Figure 4.6: *Lower limit for the number of fragments in H2-series. The data in this plot should be considered with care since it is not the total number of fragements.*

ure 3.24, where the number of fragments is plotted through time, all these three experiments have a linear increase in time. This means that even more fragments may have been produced if the experiments were allowed to continue.

It was suggested above that the maximum level for the number of fragments for the P-series was an effect of the resolution of the images. It is therefore interesting that for the H2-series, where the camera is placed closer to the cell, the number of fragments is higher. The resolution of the images can be expressed as the size of a pixel in cm. For P and H1 series the pixel size is $(0.056cm)^2$ whereas for the H2-series pixel size is $(0.035cm)^2$. If I count the number of fragments that are smaller than $(0.056cm)^2$ in the H2-series and subtract this number from the data in figure 4.6, I get the

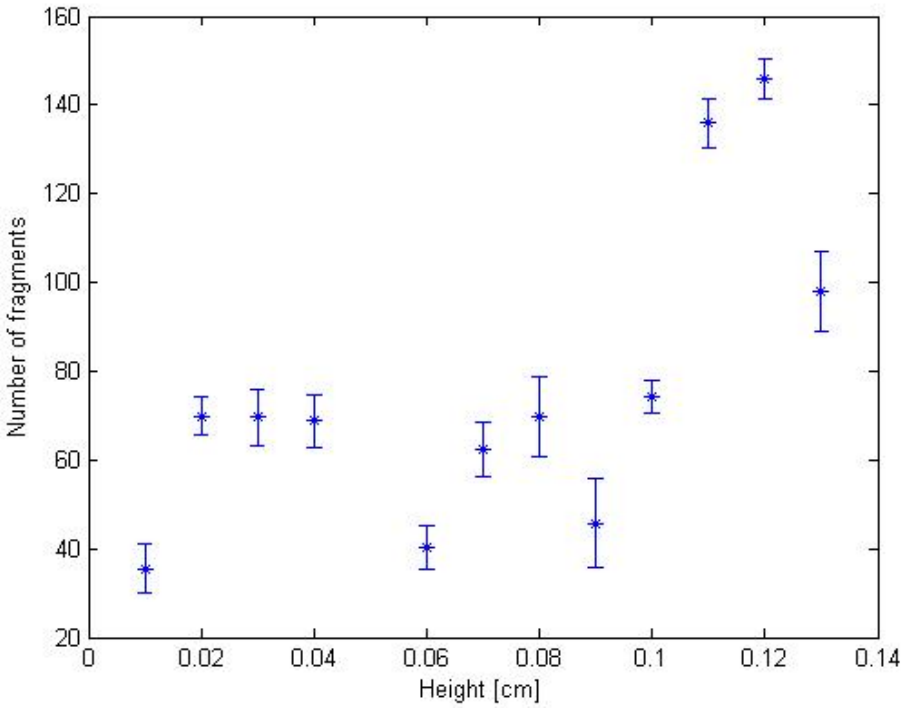

Figure 4.7: *Number of fragments in H2-series when fragments smaller than the smallest fragments in P and H1 series are subtracted. It is observed that the number of fragments is now much lower and is closer to the maximum observed for P-series.*

plot given in figure 4.7. In this plot it can be observed that the maximum number of fragments is similar to the apparent maximum seen in figure 4.2. This observation suggests that the maximum observed is an effect of the resolution of the images. Also, it suggests that there is a trade off between the resolution and the size of the frame. This means that there is an optimal distance between the camera and the cell that can give a high enough resolution and a large enough frame so that fragments do not leave the frame too early.

Different dynamics for different morphology?

It is shown above that the total number of fragments measured is depending on the resolution of the images. This means that the apparent saturation of total number of fragments in figure 4.2 for channeling-experiments might just be an effect of the resolution. It is therefore not possible to decipher if this saturation is a result of different dynamics or an effect of the resolution.

4.3 Repeatability of the experiments

A stability analysis was performed by conducting experiments with the same pressures and height several times. The experiments that were performed were 5x($P = 2 \cdot 10^4$Pa, $h = 2$cm), 2x($P = 2 \cdot 10^4$Pa, $h = 3$cm), 3x($P = 8 \cdot 10^4$Pa, $h = 4$cm) and 5x($P = 8 \cdot 10^4$Pa, $h = 5$cm). Further referred to as S1, S2, S3 and S4, respectively.

S1

This series of experiments uses a pressure of $2 \cdot 10^4$Pa and a height of 2.0cm. The ratio a, from equation 4.2, for these experiments is 97. Comparing this value with the value in table 4.1 it can be seen that this corresponds to the transition regime (a-value for experiments that can result in either morphology). Experimental images showing the morphology of the experiments are presented in figure 4.8. It is difficult to determine the morphology from the experiments, except for the experiment in figure 4.8a, which is clearly channeling. The other experiments show some resemblance to both lift off and channeling. This observation suggests, as already discused in section 4.1, that there is no abrupt change in regime but that the change is continuous.

In figure 4.9 the number of fragments through time is given. As expected, the number of fragments increases with time for all of the experiments. There is, however, a difference in shape of the distribution-pattern. The first plot from the left (S1.1) has the same shape as the plots 4 and 5 (S1.4 and S1.5) and shows saturation over time. The other two however do not show any saturation.

By a similar analysis as was done in section 4.2 it is possible to study the total number of fragments. The result of this can be seen in figure 4.10. The total number of fragments is more or less random, 3 of the experiments have similar numbers of fragments, but the other two differ. This is not so

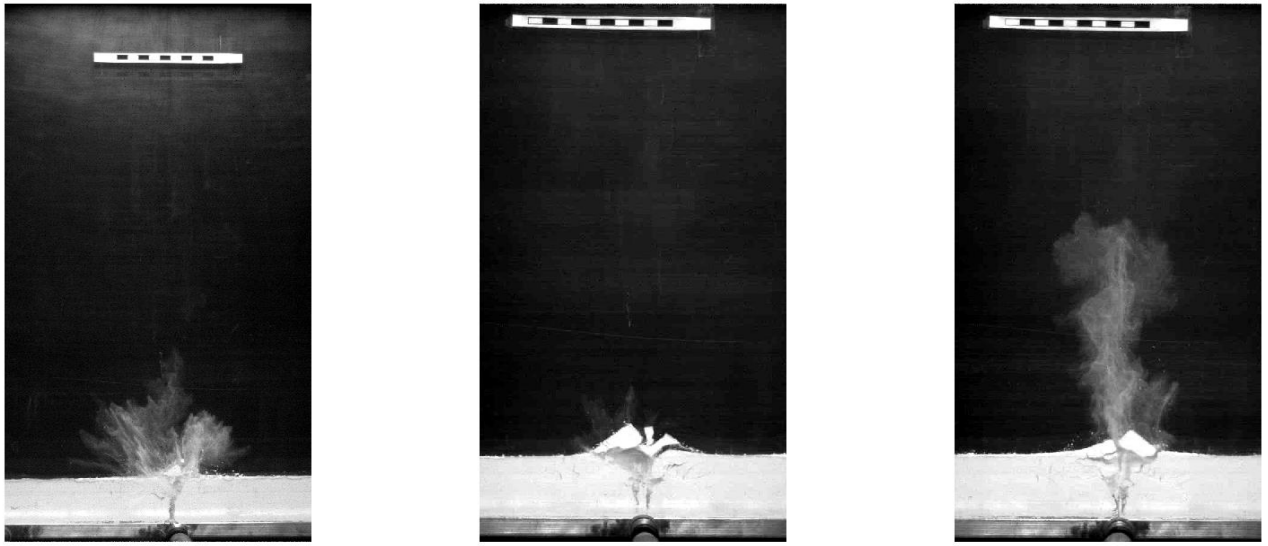

(a) S1.1 **(b)** S1.2 **(c)** S1.3

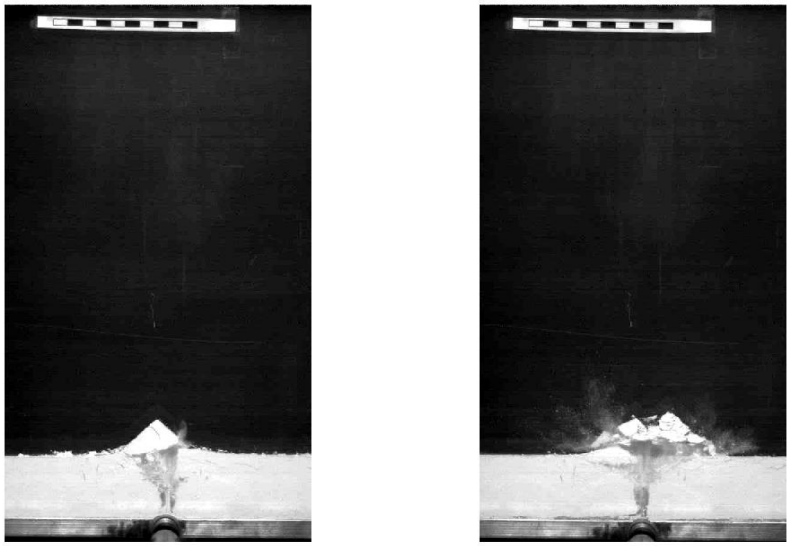

(d) S1.4 **(e)** S1.5

Figure 4.8: *Experimental image showing the morphology of S1. It is difficult to determine the morphology of the different experiments. Except for (a), which is clearly within a channeling-regime, the morphologies can be both channeling and lift off.*

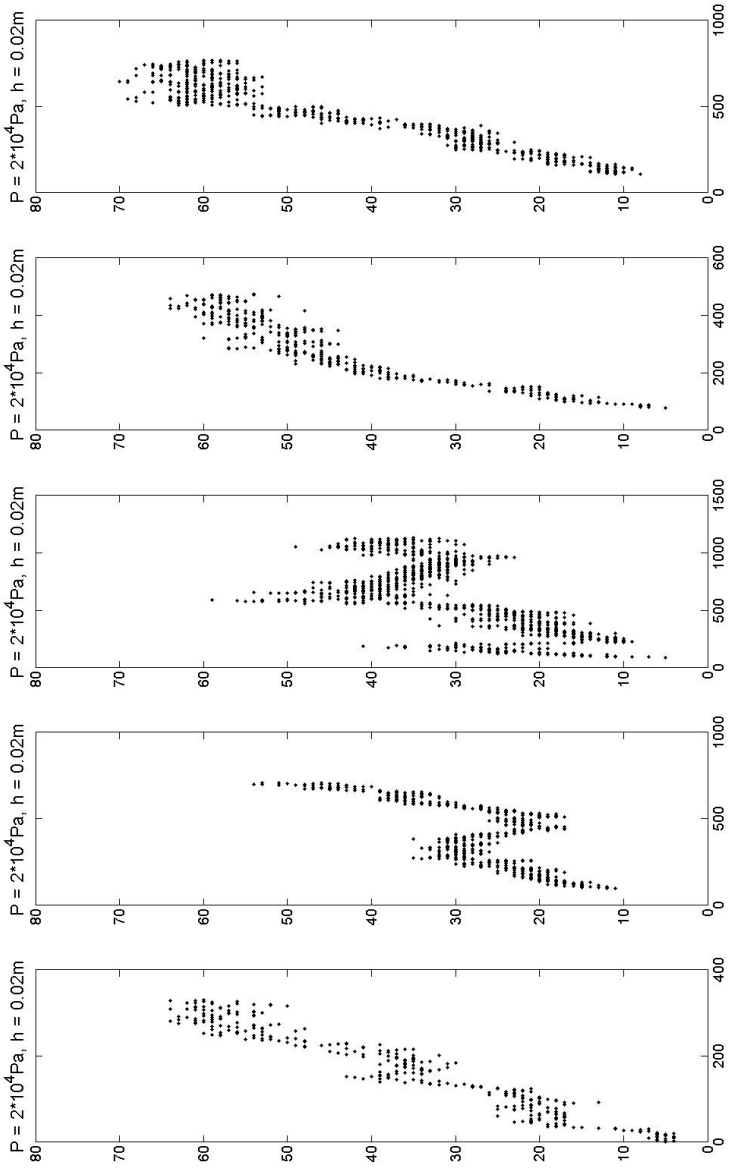

Figure 4.9: *Number of fragments through time for S1. The experiments are named S1.1, S1.2, S1.3 S1.4 and S1.5, respectively, starting from the left.*

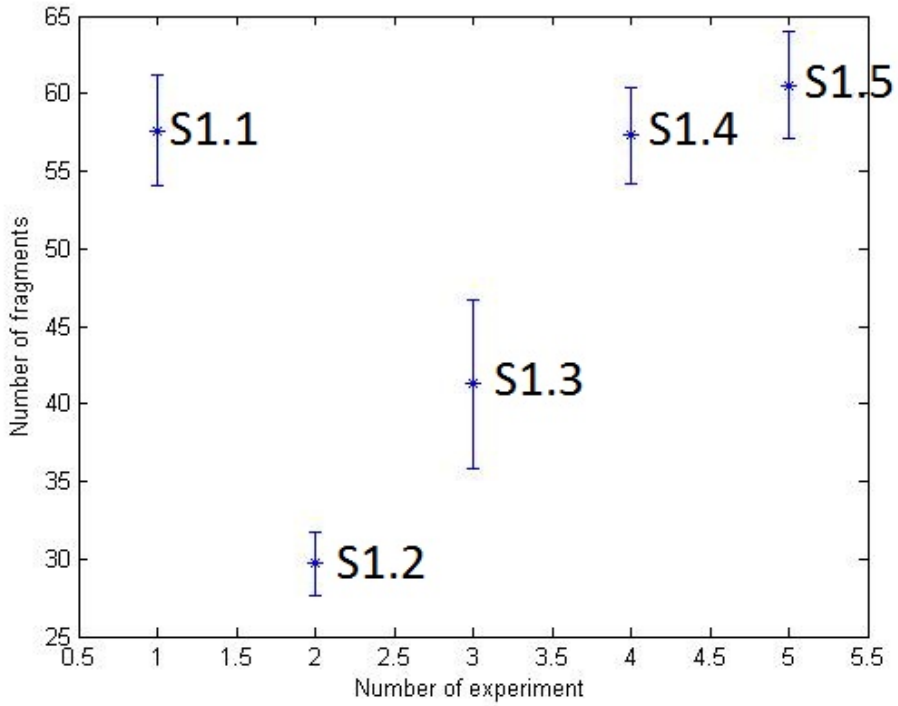

Figure 4.10: *Total number of fragments in S1. This shows that S1.1, S1.4 and S1.5 approximately the same total number of fragments, whereas the other two have fewer fragments.*

surprising, since the experiments are in the transition phase between lift off and channeling. From this stability analysis it becomes clear that the data for experiments in this transition phase should be considered with care.

The average size through time for S1 is given in figure 4.11. It also shows a difference in the shape of the data distribution for the different experiments. The final average sizes have been calculated, and are given in figure 4.12. This figure shows that the average size seems more robust than the number of fragments. Even though there is a spread in value, the difference from the smallest to the largest is only $0.09cm^2$, which is less than the change in value for different pressures in figure 4.3.

The D-value can also be studied for S1, the D-value is plotted in figure 4.13. For four of the experiments it can be observed that the D-value is

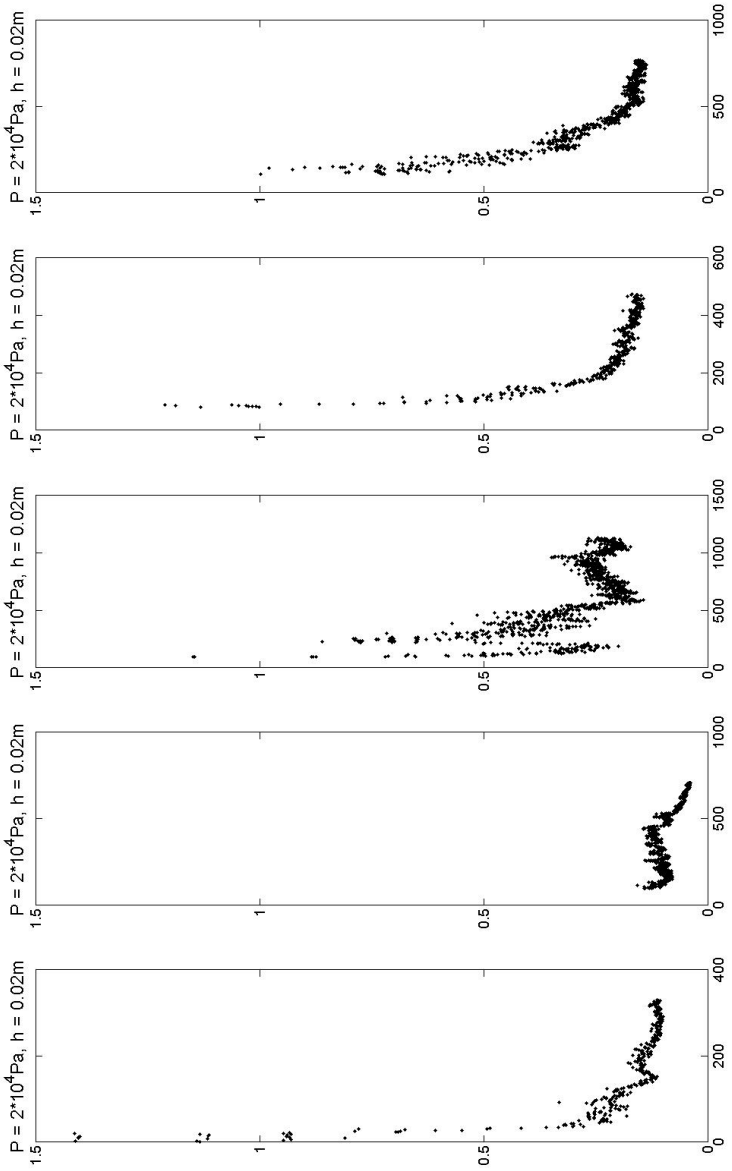

Figure 4.11: *Average size of fragments through time. The number on the y-axis are given in* cm^2

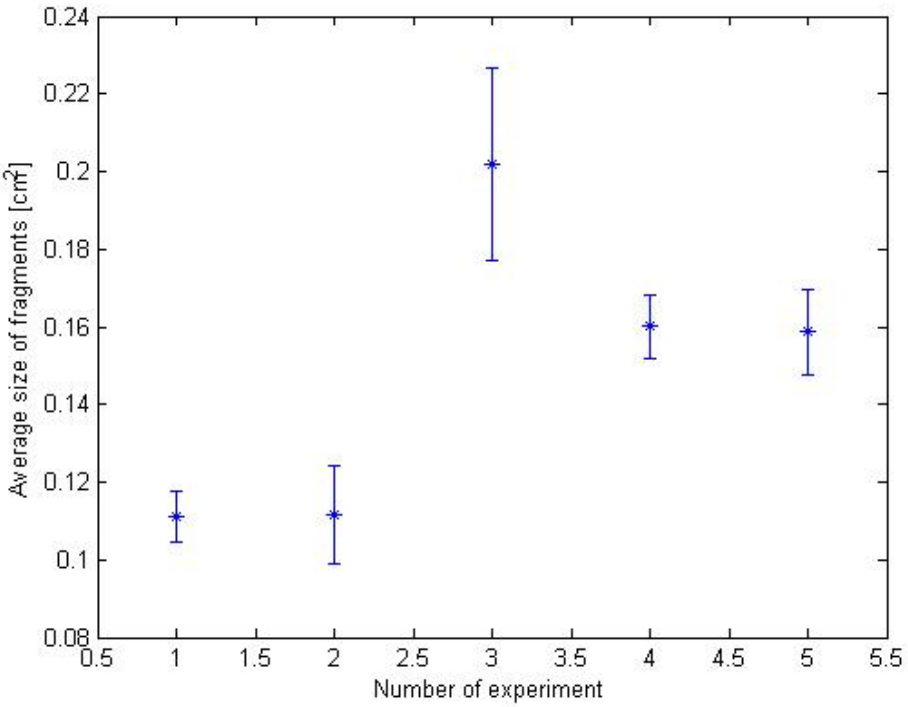

Figure 4.12: *Final average size for S1. The variation in average size is small. The absolute difference between the largest and the smallest average size is* $0.09cm^2$

more or less constant, but one experiment has a value higher than these.

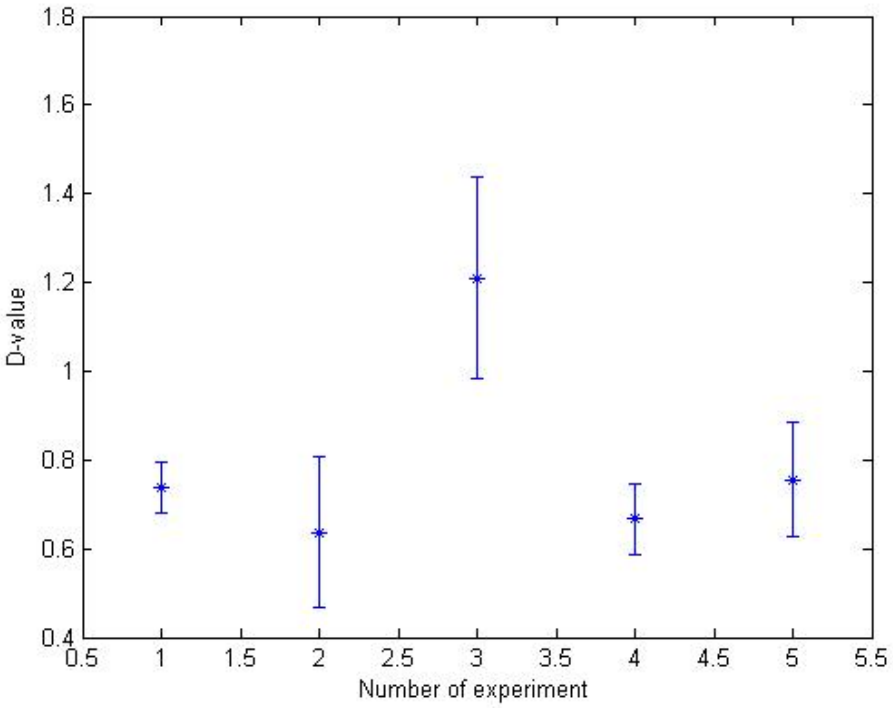

Figure 4.13: *Absolute value of D for S1. It can be observed that for S1.1, S1.2, S1.4 and S1.5 have a more or less constant value, but S1.3 has a much higher value than the these.*

S2

In S2 two experiments were performed with a pressure of $2 \cdot 10^4$Pa and a height of 3cm. The ratio a for these experiments is 65, which puts them into the transitional phase. In figure 4.14 the total number and final average size of the fragments are presented. The values are calculated in the same way as before.

The plots in figure 4.14 show that there is a large difference in both the total number and the final average size. This is not surprising since the a-ratio suggests that the experiments are within the transitional phase between the two regimes.

In figure 4.15 the D-values for S2 are plotted. This figure shows that the D-values have very similar values.

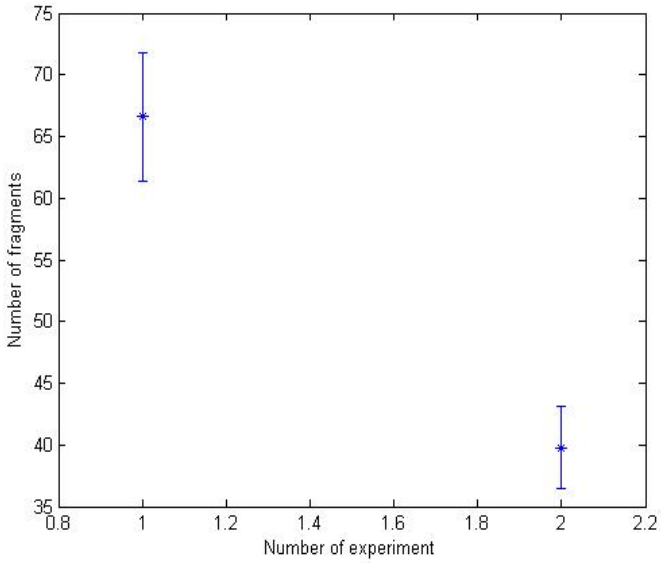

(a) Number of fragments (S2)

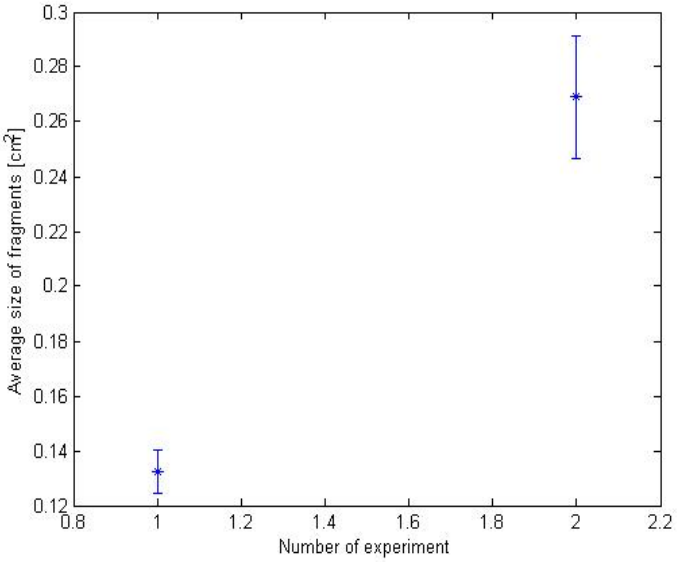

(b) Average size (S2)

Figure 4.14: *Total number and final average size of the fragment for S2*

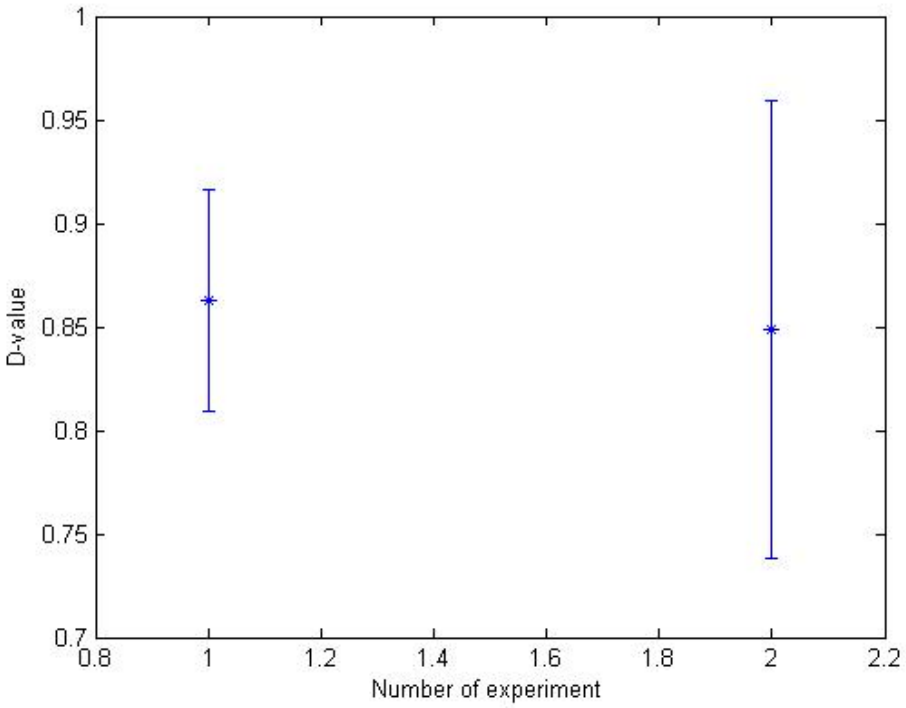

Figure 4.15: *Absolute value of D for S2 series. The values are more or less constant.*

S3

In S3 three experiments were performed with a pressure of $8 \cdot 10^4$Pa and a height of 4cm. The ratio a for these experiments is 194. This ratio suggests that these experiments are within the channeling regime. In figure 4.16 the total number and the final average size of the fragments are presented.

The total number of fragments presented in figure 4.16 shows little stability, even though this experiments according to the a-ratio should give more stable results. The average size does however give more stable results, where the difference between the largest and the smallest is $0.08cm^2$.

The D-values in S3 are plotted in figure 4.17. The difference between the largest and the smallest value for these are 0.078.

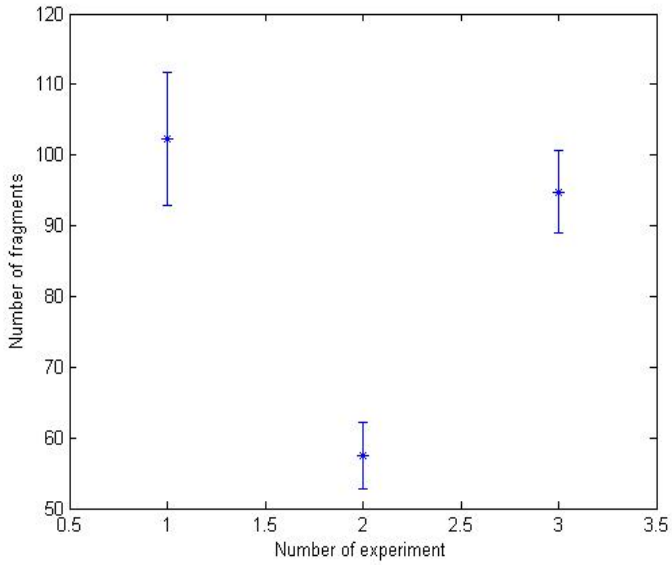

(a) Number of fragments (S3)

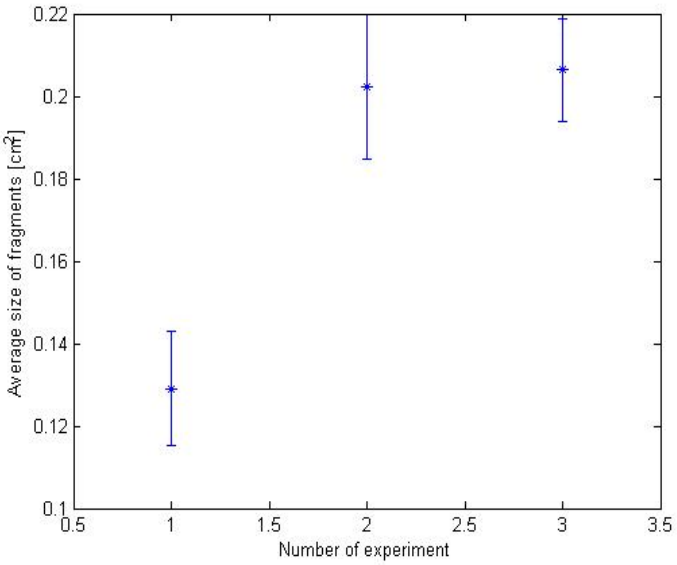

(b) Average size (S3)

Figure 4.16: *Total number and final average size of fragment for S3.*

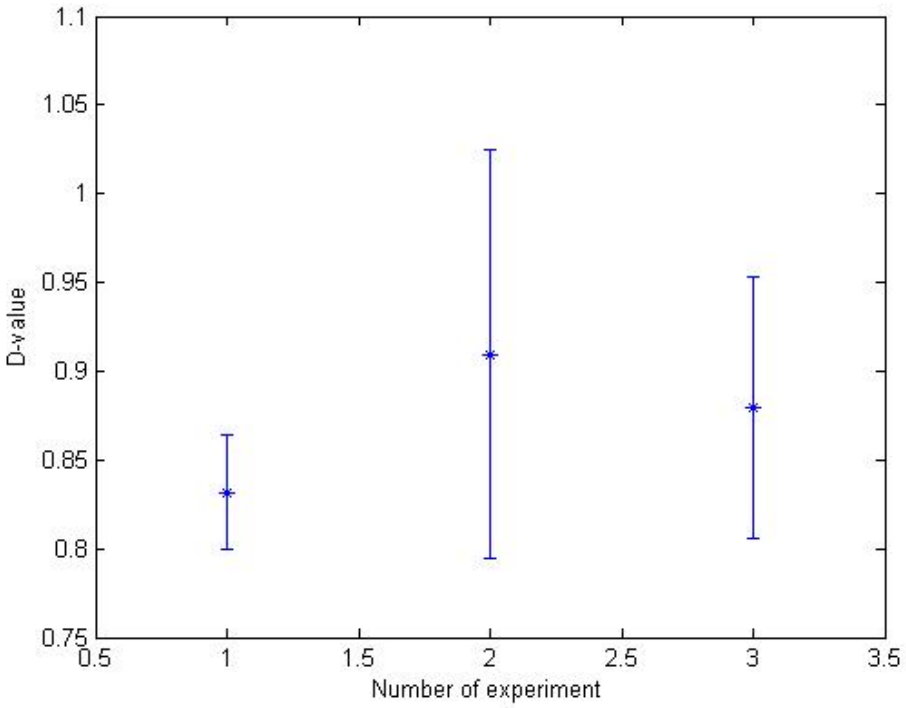

Figure 4.17: *Absolute value of D for S3*

S4

In S4 five experiments with a pressure of $8 \cdot 10^4$Pa and a height of 5cm were performed. This means that these experiments have a a-ratio of 155, which puts the experiments into the channeling regime according to table 4.1. The total number and final size of the fragments are presented in figure 4.18

This figure shows again that the total number of fragments in the experiments is not very stable. The average size is more stable, however, with a difference from the largest to the smallest of $0.07cm^2$.

In figure 4.19 the D-value for S4 is given. This figure shows that the D-value for these experiments are not stable, with a difference from the largest to the smallest of 0.34.

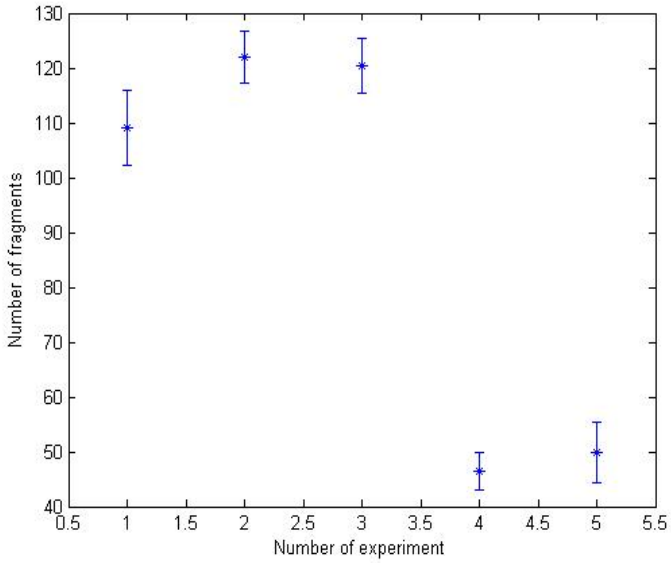

(a) Number of fragments (S4)

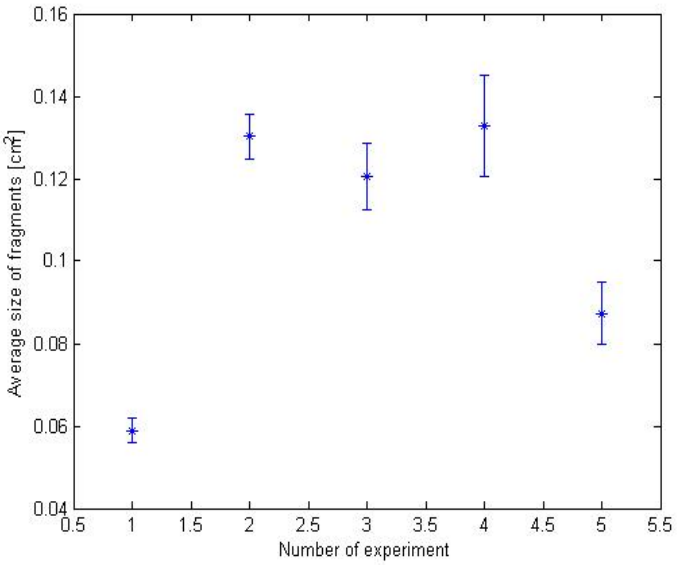

(b) Average size (S4)

Figure 4.18: *Total number and final average size of fragment for S4.*

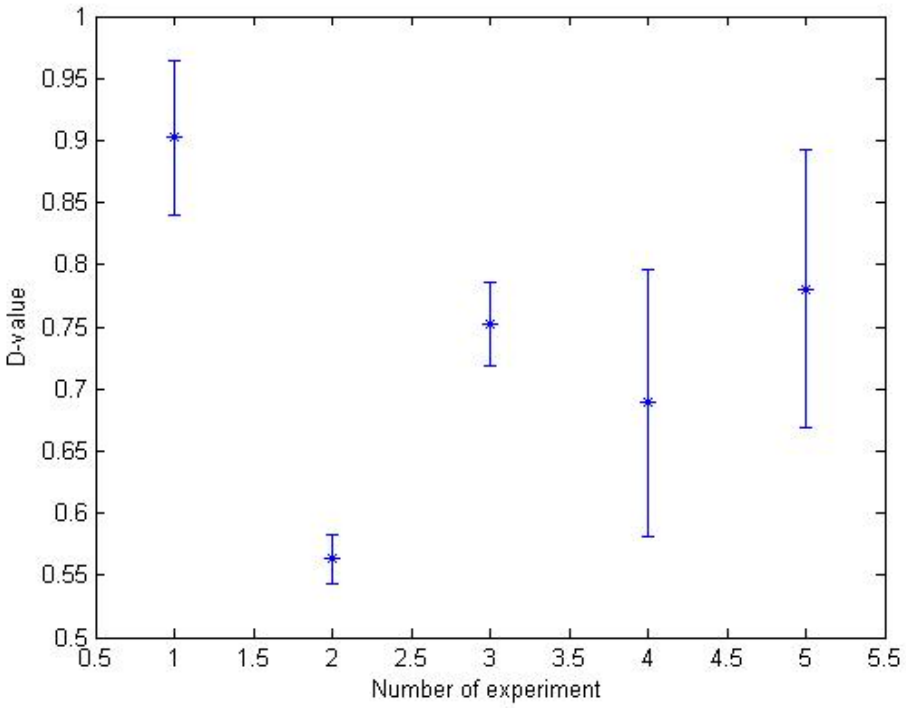

Figure 4.19: *Absolute value of D for S4*

Stability of experiments

The stability analysis has shown that the total number of fragments and D-values are more random than what was expected. The average size seems to be more stable, with a absolute error $< 0.1cm^2$, this error is lower than the change in average size for different pressure given in figure 4.3.

Experiments from S3 and S4 show a surprising distribution of the total number of fragments. Even though the data is not consistent it does seem to be some system to it. For S3 two of the experiments have approximately 100 fragments and one experiments has approximately 55. For S4 three of the experiments have a total number of fragments of 110-120, and two experiment have 50. This could of course be coincidental, but if the data was truly random such results would not be expected.

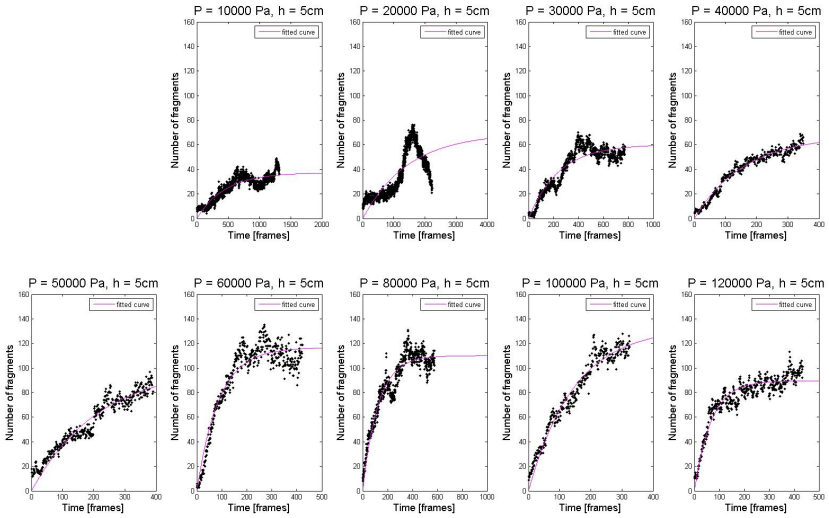

Figure 4.20: *Number of fragments through time for each experiment. A function* $a_{nmb}(1 - e^{-b_{nmb}t})$ *has been fitted to the plots. The coefficient* a_{nmb} *would then represent the total number of fragments.*

4.4 Time evolution of fragmentation

In section 4.2 an estimate for the total number and final average size of fragments was presented by manually calculating the saturation levels from figure 3.20, 3.23 and 3.24. In this section I will derive a mathematical description of the time evolution of the number of fragments, and I will derive expressions for the final average size of fragments and the D-values with respect to the pressure.

P-series

Starting with the number of fragments, an expression for the time evolution can be derived by observing that the plots in figure 3.20 have, for some experiments, a very similar shape. It can be observed that the plots resemble exponential functions. In figure 4.20 a function $a_{nmb}(1 - e^{-b_{nmb}t})$, where a_{nmb} and b_{nmb} are coefficients, has been fitted to the data in figure 3.20 using the Matlab-function *fit*.

The *fit*-function returns the coefficients a_{nmb} and b_{nmb} for each fit, i.e. for each experiment (see figure 4.20). The dependence of the coefficients on the pressure can be studied by plotting the value for each fit in figure 4.20 in a loglog-plot (plot with logarithmic axes). If the data fall on a line in the loglog-plot it means that

$$x \propto P^{\alpha} \tag{4.3}$$

Where x is the parameter of interest, P is the pressure and α is a constant. The constant α can be determined by fitting a line to the data in the loglog-plot, then the slope of the line is α.

A loglog plot of a_{nmb} and b_{nmb} againts the pressure is presented in figure 4.21. Note that the point for the experiment with $P = 2 \cdot 10^4$Pa has been neglected in these plots due to the poor fit.

This shows that $a_{nmb} \propto P^{0.47} \approx \sqrt{P}$ and $b_{nmb} \propto P^{0.67} \approx P^{2/3}$, which leads to

$$N(t, P) = A_{nmb}\sqrt{P}(1 - e^{-B_{nmb}P^{2/3}t}), \tag{4.4}$$

where $N(t, P)$ is the number of fragments and A_{nmb} and B_{nmb} are constants. Since the number of fragments is a dimensionless quantity the constant A_{nmb} needs to have the unit $\sqrt{\frac{m^2}{N}}$, and since the exponent also needs to be dimensionless the constant B_{nmb} need to have the unit $(\frac{m^2}{N})^{2/3}s^{-1}$

The same analysis can be used to get an expression for the average size of fragments with time. This means that by finding a suitable function to fit the data given in figure 3.21 I can derive a mathematical expression for the average size. Such a function can be $a_{avg} + b_{avg}e^{c_{avg}t}$, where a_{avg} would represent the final average size. The average size for each experiment and the fitted line is given in figure 4.22 From this figure it can be observed that the experiments with pressure of $1 \cdot 10^4$Pa and $2 \cdot 10^4$Pa has a poor fit, therefore these experiments will be neglected in this analysis.

To find the dependence of a_{avg}, b_{avg} and c_{avg} on the pressure loglog-plots have been made, and a line has been fitted through these points. However, this linear fit is so poor that no reasonable result can be obtained (see figure 4.23).

This analysis is not applicable for the D-value, as too few of the data points plotted in figure 3.22 show similarities.

Since it is not possible to use the method of fitting a function to the average size and the D-values the dependence of these parameters on the pressure needs to be calculated manually, without considering the time.

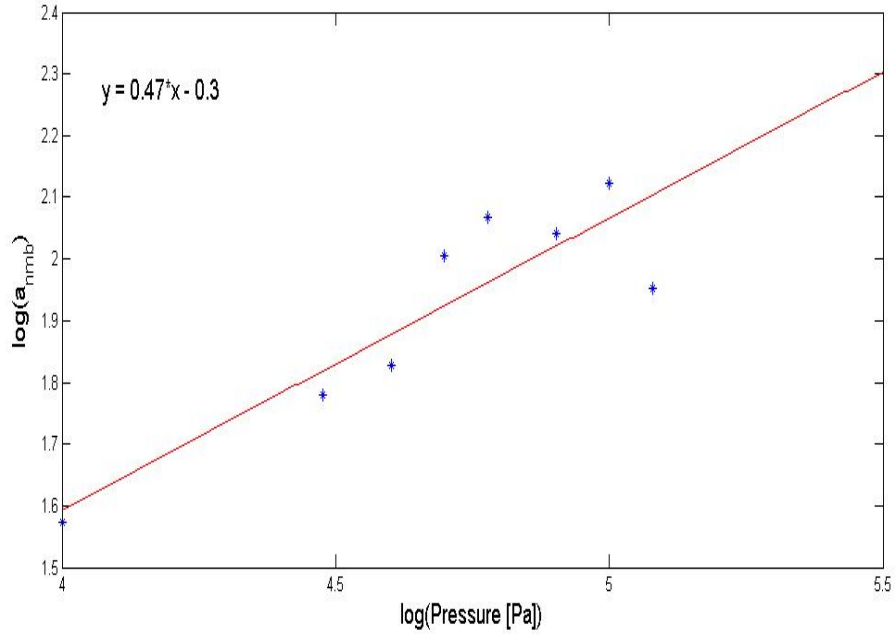

(a) a_{nmb}

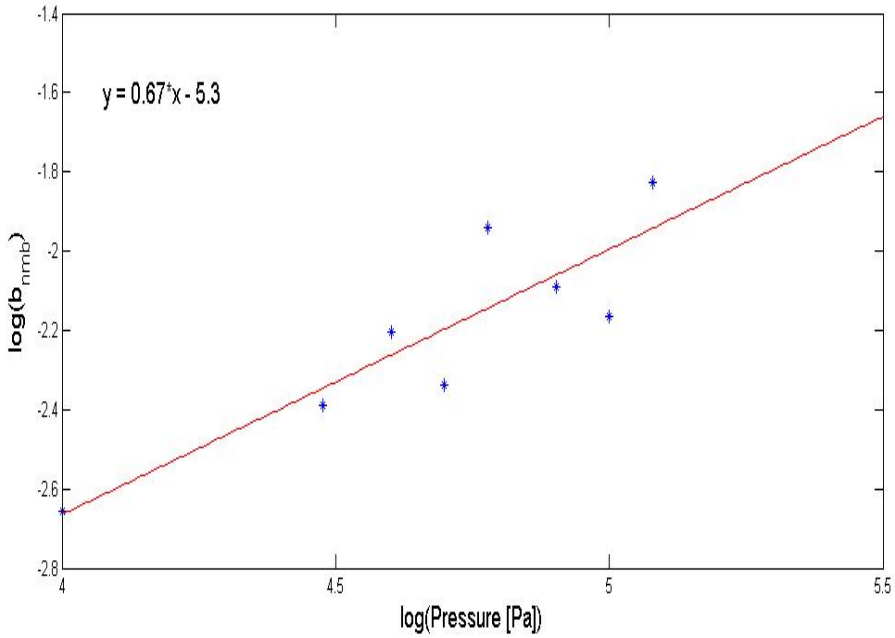

(b) b_{nmb}

Figure 4.21: *loglog-plots of the value of the coefficients a_{nmb} and b_{nmb} derived by fitting the function $a_{nmb}(1 - e^{-b_{nmb}t})$ to the data in figure 3.20.*

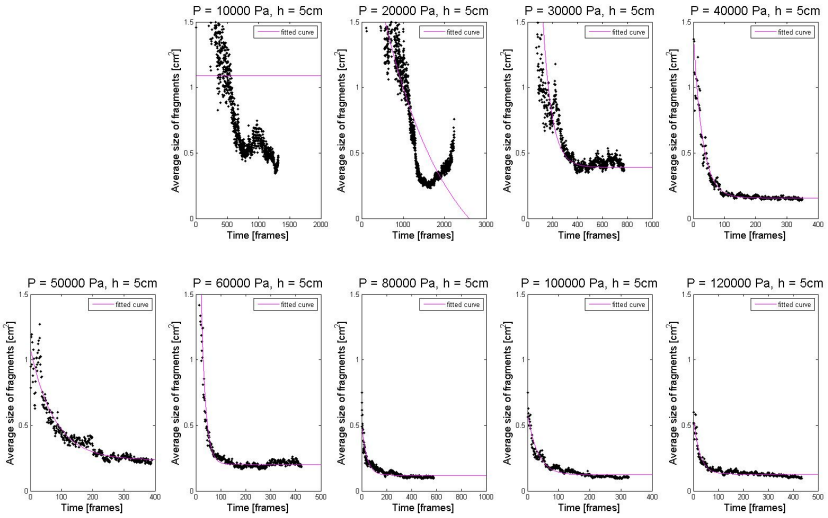

Figure 4.22: *The average size of fragments with time for each experiment. A function $a_{avg} + b_{avg}e^{c_{avg}t}$ has been fitted to the data points. Note that the experiments with pressure of $1 * 10^4 Pa$ and $2 * 10^4 Pa$ have a poor fit, and are neglected.*

This means finding expression for the final average sizes and the final D-values. This has, however, already been done in figure 4.3 for the final average sizes.

How the average size of fragments is depending on the pressure can be studied in a similar way as above for the coefficients. A loglog-plot of the data in figure 4.3 is given in figure 4.24. From this figure it can be seen that

$$A(P) \propto P^{-0.68} \Rightarrow A(P) \propto P^{-2/3} \tag{4.5}$$

In figure 3.22 the exponent, D, of the size distribution was plotted against time. It was observed that in many of the experiments the D-value saturated with time. This means that it is possible to calculate the average value around the saturation level, and this value would represent the final D-value. The result of this analysis is given in figure 4.25a.

There seems to be an increase in the D-value with increasing pressure, though this is not always the case, since for instance the D-value for $4 \cdot 10^4$Pa is much lower than the others. A loglog-plot of the data in figure 4.25a is

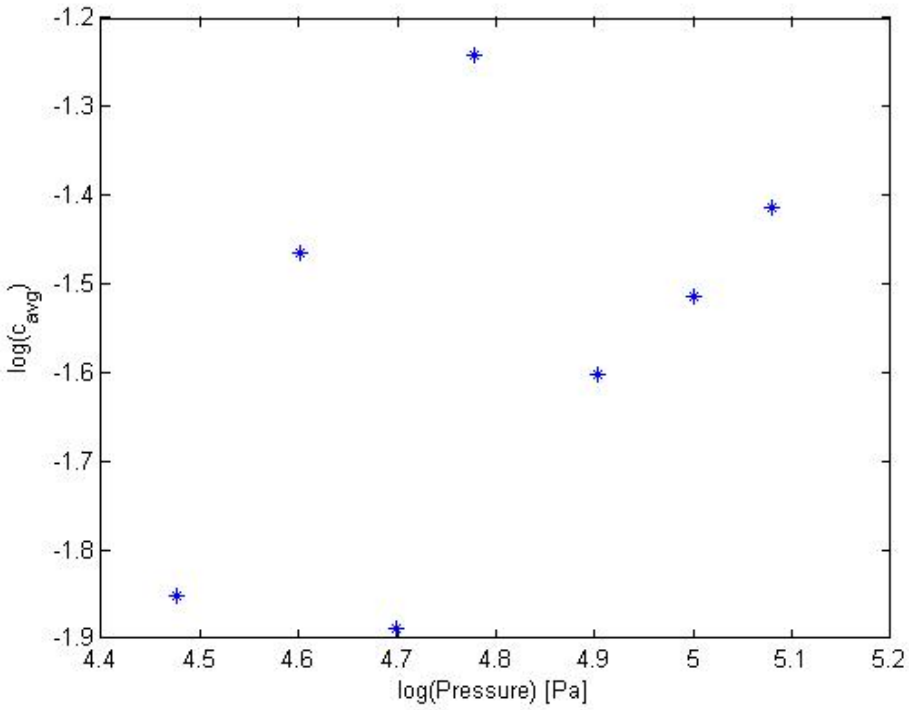

Figure 4.23: *loglog-plot of c_{avg} (the exponent in the fitting function) versus the pressure. It is observed that there is too uch spread in the value to do use this method to find an expression*

given in figure 4.25b. This shows that

$$D(P) \propto P^{0.2} = P^{1/5}. \tag{4.6}$$

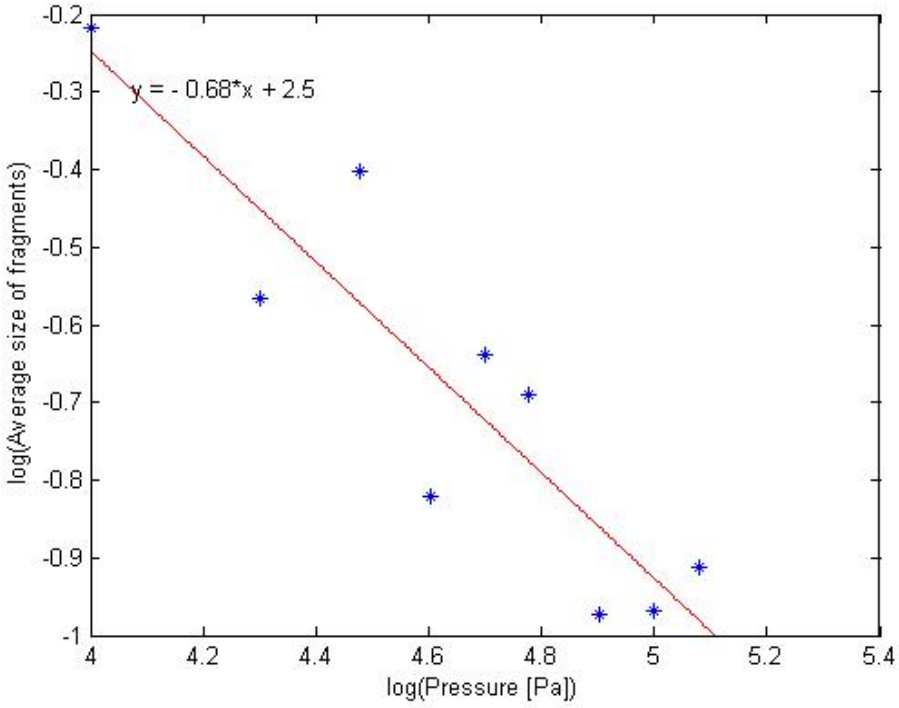

Figure 4.24: *loglog-plot of the final average size for each experiments in the P-series (data from figure 4.3). The slope of the line give* $\alpha = -0.68$.

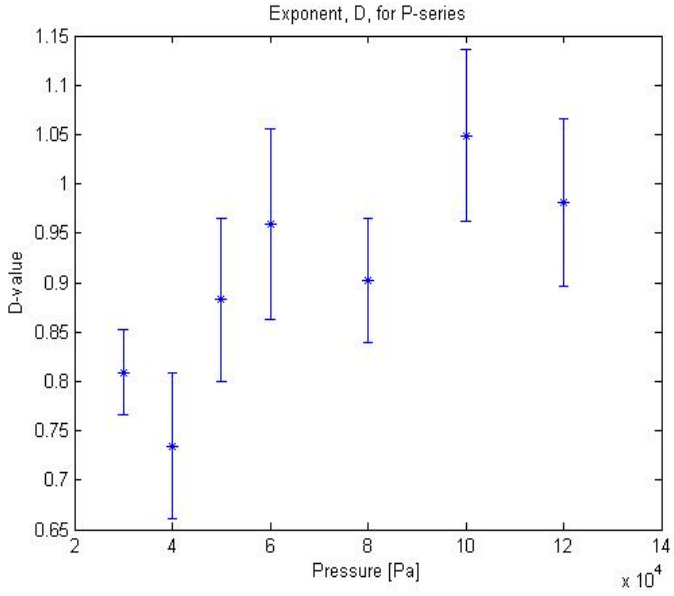

(a) Final D value

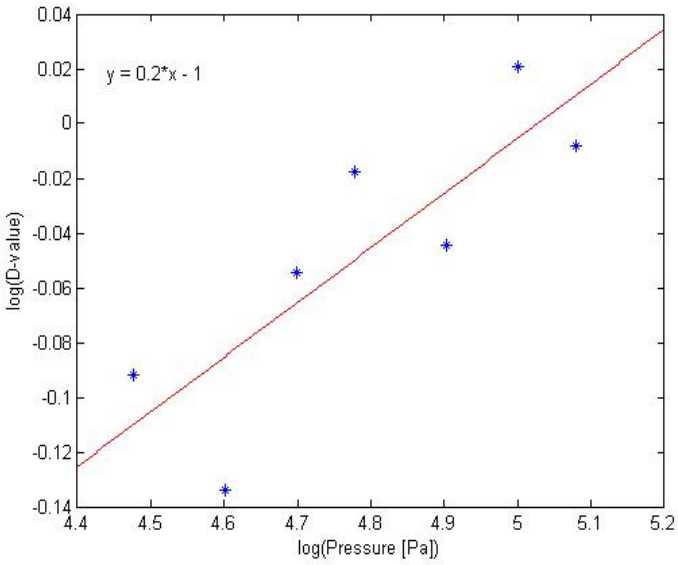

(b) loglog-plot of final D value

Figure 4.25: *(a) Plot of the values at the saturation level for the D-value given in figure 3.22. Only the experiments that show saturation in time have been analyzed. There seems to be a tendency that the D-value increases with increasing pressure. (b) loglog-plot of D-value from figure 4.25a. A line has been fitted to the data with a slope of 0.2.*

H1 and H2 series

As can be observed in figure 4.4, 4.5 and 4.6 there is no clear relation between the number of fragments and height or average size of fragments and height. Therefore a similar analysis as done above is not possible for the H1 and the H2 series.

4.5 Comparison between former work and my experiments

In this section I will discuss and compare my experimental results with the results found through fieldwork, earlier experiments and theory.

Field work

My experiments resemble a phreatic eruption in nature, since a phreatic eruption is an explosion due to sudden volume change inside the rock. This means that I can compare my experimental piercement structures with hydrothermal vents (piercement structures from a phreatic eruption). Since it was shown in section 2.1 that the shape of a maar-diatreme systems (piercement structures from phreatomagmatic eruptions) is very similar to hydrothermal vents, I can also compare my experimental piercement structures with maar diatreme systems.

A sketch of a hydrothermal vent and a maars-diatreme system is presented in figure 4.26 in comparison with an image from my experiments. From this figure a clear similarity between the two natural system and my experiments can be seen. All examples show at the lowest part a pipe/diatreme and at the top a V-shape structure. However, in the two natural systems the piercement structures are filled with brecciated rocks. This is not seen in the experiments, where the material in general is ejected out and only parts of it falls back into the pipe.

There is no sign of creation of a maar after the experiment is over. A maar is a collapse crater, [Lorenz, 1985], which means that the walls collapse into the pipe. The material in my experiment stays the same, and no collapses occur, i.e. I have an open pipe after an experiment. This is probably due to the high cohesion of the silica powder. By increasing the

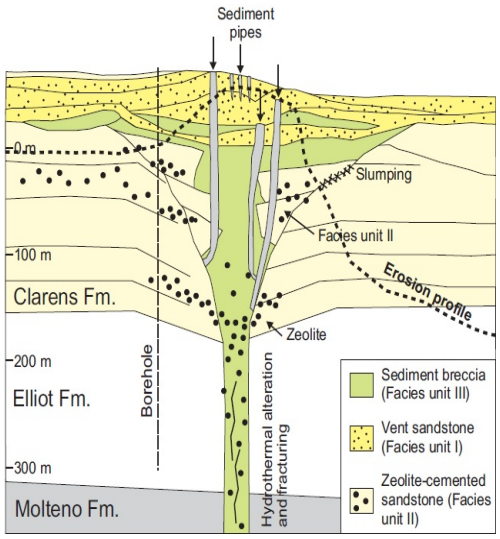

(a) Hydrothermal vent

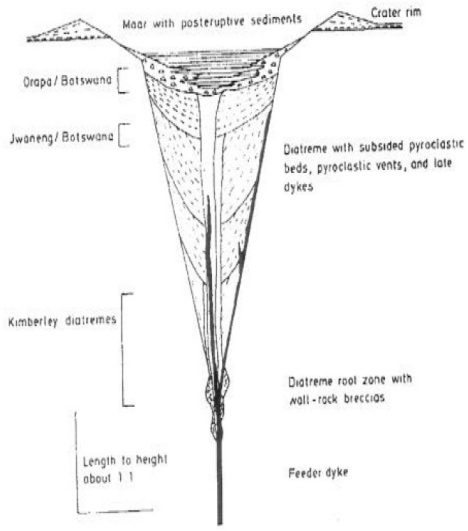

(b) Maar-diatreme

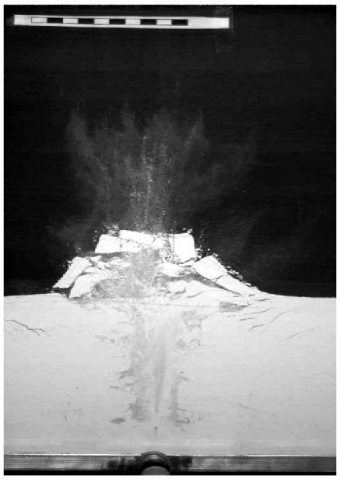

(c) Experimental image

Figure 4.26: *(a) Sketch of hydrothermal vent. Figure from [Svensen et al., 2006]. (b) sketch of a maar-diatreme volcano. Figure from from [Lorenz, 1985]. (c) Experimental image with* $P = 8 * 10^4 Pa$ *and* $h = 10cm$

height of the powder above what I tested in my experiments the creation of maars might be seen.

It is important to notice, however, that the my experiments are not properly scaled towards an actual eruption. Therefore, these observation are only suggestions due to the similarity between the structures.

In section 2.1 it was stated that fragment size distributions measured in the field reveal a power law distribution. My experimental results also show a power law distribution (figure 3.18). Though, the D-values in my experiment is far below that from the field where the D-values are often above 3 (and even higher for phreatic eruptions). There are two explanation for the low D-values in my experiments. First, I measure the fragment size distributions from images, which is a 2 dimensional analysis. It might therefore be expected that my D-values should be lower than an analysis in 3 dimensions. Another explanation is that the volcanic deposits have experienced a far more extensive fragmentation, for instance through transport. Kaminski and Jaupart [1998] showed that during an eruption there is an initial D-value, caused by the eruption and that the D-value can increase during transport.

Notice that the fragment size distributions presented in section 2.1 are from magmatic eruptions. Since my experiments model a phreatic or a phreatomagmatic eruption this comparison is not entirely justified.

Jébrak [1997] suggested that the D-value from a brecciation process depends on the amount of energy. This is also observed in my experiments, where the D-value is seen to increase with increasing pressure.

Experiments

In section 2.2 the MFCI-experiments was described. In the MFCI experiment the ejection of the material from the crucible is not controlled. My experiment can serve as an analogue to this part with less complexity and more controlled parameters.

In a MFCI experiment it is difficult to relate the fragmentation process with the energy released through evaporation of the water. Studying the fragment size distribution from such an experiment has little reliability. With my experiment, I am able to show that the number of fragments will increase and the average size of the fragments will decrease for increasing pressure. In addition my experiments suggests that the D-value will increase

with increasing pressure. This means that these parameters can serve as a measure of the pressure in the MFCI experiments.

The experiment by Gilvarry and Bergstrom [1961] showed that depending on the *a priori* distribution of flaws within the material the outcome of the fragment size distribution may vary. This might explain why, for some of my results, there is a certain randomness in D-value, see figure 4.25a.

The experiments of Oddershede et al. [1993] showed that the fragment size distribution was depending on the geometry. This can also be seen in my experiments. When the height is varied the geometry changes, resulting in a difference in fragment size distributions. My results do not, however, show a systematic change in fragment size distributions for varying heights.

Similar to the experiments by Kadono and Arakawa [2002], I see that the D-value increase with time. In addition, my experiments show that the D-values saturates in time. Showing that the fragment size distribution is depending on time.

Theory and simulations

One of the advantages with my experiments is that I am able to observe a fragmentation process as it occurs. This enables me to discriminate between different models. In figure 4.27 an example of a fragment size distribution from an experiment is given. Some theoretical distributions have been fitted to the experimental data. From this figure it can be observed that the best fits are the power law distribution and the sequential fragmentation distribution. The other two distributions, Geometric distribution and Åström's have a poorer fit.

The geometric fragmentation theory described in section 2.3 simulates a fragmentation process by randomly separating an area or a mass. From observation of my experimental images this model does not seem to be applicable for my experiments. In my experiment the fractures are propagating in time, with different velocities and a finite amount of energy, meaning that one fracture can not be regarded separately from the other fractures. These arguments shows that the geometric fragmentation model is not applicable for describing the transient behavior of fragmentation. It could, however, be possible that the geometric fragmentation theory is able to predict the final fragment size distribution. This is not the case, from figure 4.27 I see a clear power law correlation, and not an exponential distribution as is suggested by the geometric fragmentation theory.

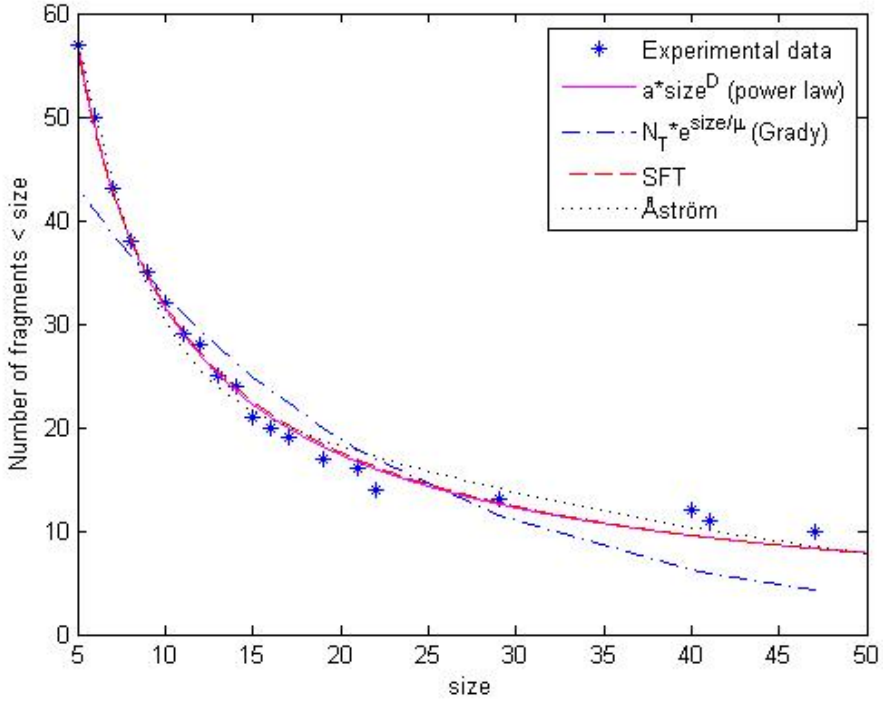

Figure 4.27: *Plot of the fragment size distribution for an experiment with a pressure of* $8 \cdot 10^4$ *Pa and a height of* 5.0 *cm at time* 289 *frames. Theoretical distributions have been fitted to the experimental data. (–) Power law distribution, (-·-) Geometric fragmentation (Grady's distribution), (- -) Sequential fragmentation distribution (eq. 2.8) and (· · ·) Åströms distribution (eq. 2.11)*

Another model presented in section 2.3 is the sequential fragmentation model, which assumes that the fragmentation process occurs sequentially. This assumption seems to be appropriate also for my experiments. In my experiments it can be observed that the fragmentation occurs due to fractures propagating and sequentially separating the material (see figure 3.7). Though, the time resolution in my experiments is high enough not to consider these events as discrete events. So that the assumption that fragmentation is a sequential process seems to be true for my experiments. To look at each fragmentation event as a discrete event is a simplification. This model does predict a power law form on the size distribution, which fits well with my experimental result, see figure 4.27.

The last model presented in section 2.3 was what I called the Åström model. An important assumption in this model is that it considers the branches that appear on a main fracture. On three occasions (see figure 3.4), branches that propagate perpendicular to the main fracture can be observed, highlighted by arrows in the figure. Though in Åströms model the branches are assumed to cause small fragments. The examples of branches given in figure 3.4 are branches with a relative large penetration depth and are therefore not likely to produce small fragments. However, since the branches, discussed by Åström, would likely be below the resolution of my images I am not able to tell if they exist in my experiments. The Åström model predicts a fragment size distribution with both a power law term and an exponential term, From figure 4.27 it can be observed that this model does not fully capture my experimental data.

Some the theories presented in section 2.3 have an exponential form of the fragment size distributions (geometric fragmentation and Åströms model[1]). This is in contrast to the natural data, where, in general, a power law distribution is found. The exponential part of the theoretical expressions come from the assumption that fractures are nucleated according to a Poisson process. If a theoretical expression should have a closer similarity with a power law distribution the derivation would need to consider another nucleation process than a Poisson.

From my experimental data I find that the D-value increase with time until it saturates. the question remains if this saturation level is caused by the end of the process, meaning that this is the final value, or if it is some point at which the D-value can not increase further. This question

[1]Though only for large fragments, see section 2.3

might be answered by looking at the number of fragments through time. Since the production of fragments also saturates in time, it is possible that the fragmentation process is finished and that the reason for saturation in D-value is that we measure a non-changing system.

4.6 Recent simulations and my experiments

Recently Gisler [In prep. 2012] performed numerical simulations of the eruption of a volatile-rich magma column with a very similar setup as used in my experiments. The simulations are performed in a 2D domain. The varying parameters are the pressure and the yield stress of the host material. The height of the overlying material is set to 2km. A phase diagram from the simulations is presented in figure 4.28. Similar to what is seen in my experiments two phases can be observed. The phases have the same morphology as lift off and channeling described above for my experiments. Similar to my experiments, lift off is achieved for low pressures and channeling for high pressures.

The two simulations ,EaDb and EaFd (see figure 4.28), may appear to be channeling, but they are in fact propagating at a lower speed, and with a meander. They can therefore not be classified as channeling.

There is a remarkable similarity between my experiments and the simluations by Gisler [In prep. 2012].

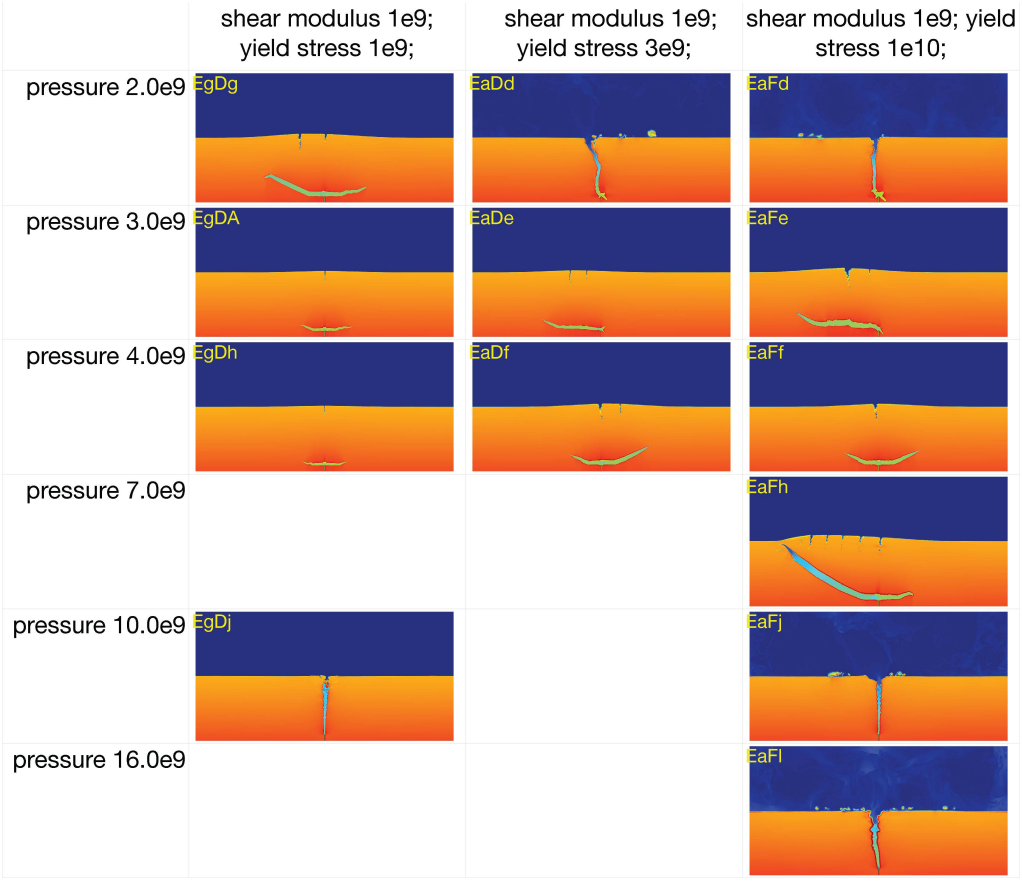

Figure 4.28: *Phase diagram from numerical simulations of a volatile-rich magma column [Gisler, In prep. 2012]. Similar to my experiments there are observed two phases which depend on the pressure. In addition the yield stress of the overlying material have been varied. There is a remarkable similarity between these simulations and my phase diagram, figure 3.6.*

Chapter 5

Conclusion

In this thesis an experimental setup allowing for the observation of fragmentation processes through time has been presented. The experiments have shown the existence of two morphologies, and that these are determined by the ratio

$$a = \frac{P}{\rho g h} \tag{5.1}$$

where for large ratio $a > 110$ there is a channeling regime and for $a < 60$ there is a lift off regime. For $65 < a < 97$ there is a transition between the two morphologies.

Compaction waves are observed, which are independent of the pressure and the height of the layer.

An image analysis program has been developed that is able to perform a quantitative analysis of the experiments. From this analysis the number of fragments, the average size of fragments and the fragment size distribution is found for each image in each experiment. Thereby giving a quantitative analysis through time. It has been shown that the number of fragments increases and the average size of fragments decreases with time. Both saturate after some time.

A study of the total number and the final average size of fragments was performed showing that the total number increases and the finale average size decreases with increasing pressure. The height of the layer is shown to not influence any of these parameters in a systematic way. For the P-series it was suggested that the number of fragments is depending on the morphologies of the experiment.

The fragment size distributions are found to be similar to power laws, and a study of the power law exponent, D, was performed. This study shows that there might be an increase of the D-value for increasing pressure and that the height of the layer does not influence the D-value in a systematic way.

Expressions for the dependence of the final average size of the fragments and the D-value on the pressure was suggested (equation 4.5 and 4.6, respectively). Also an expression giving the number of fragments as a function of time and pressure was proposed (see equation 4.4).

A stability analysis of the experiments was performed. This showed a limited reproducibility of the experiments. However, for experiments in a channeling regime there seems to be two distinct values possible for the number and average size of the fragments.

The experiments show similarities of the diatrems (see figure 4.26). No production of maars can be observed, though by increasing the height of the layer in the experiments it is suggested that this may be found. The fragment size distributions in my experiments are found to be power laws, similar to that from the field work on explosive volcanism. The value of the exponent is, however, much smaller than what is found in the field.

Comparing my experiments with the former experiments presented in section 2.2, it is suggested that my experiments represent an analogue to the ejection phase of a MFCI experiment. The different D-values for H1-series can be explained by the fact that the geometry changes, [Gilvarry and Bergstrom, 1961]. Similar to the experiments of Kadono and Arakawa [2002] I see that the D-value increase with time.

In my experiments it can be observed that the fragmentation occurs sequentially as predicted by the sequential fragmentation theory. Branches can also be observed, as predicted by Åströms model.

Bibliography

JA Åström. Statistical models of brittle fragmentation. *Advances in Physics*, 55(3):247–278, 2006.

W.K. Brown and K.H. Wohletz. Derivation of the weibull distribution based on physical principles and its connection to the rosin–rammler and lognormal distributions. *Journal of Applied Physics*, 78(4):2758–2763, 1995.

PRL Browne and JV Lawless. Characteristics of hydrothermal eruptions, with examples from New Zealand and elsewhere. *Earth-Science Reviews*, 52(4):299–331, 2001. ISSN 0012-8252.

R. Büttner and B. Zimanowski. Physics of thermohydraulic explosions. *Physical Review E*, 57(5):5726–5729, 1998. ISSN 1550-2376.

J. Fineberg and M. Marder. Instability in dynamic fracture. *Physics Reports*, 313(1):1, 1999.

O. Galland, P.R. Cobbold, E. Hallot, J. de Bremond d'Ars, and G. Delavaud. Use of vegetable oil and silica powder for scale modelling of magmatic intrusion in a deforming brittle crust. *Earth and Planetary Science Letters*, 243(3-4):786–804, 2006.

O. Galland, S. Planke, E.R. Neumann, and A. Malthe-Sørenssen. Experimental modelling of shallow magma emplacement: Application to saucer-shaped intrusions. *Earth and Planetary Science Letters*, 277(3-4): 373–383, 2009.

JJ Gilvarry. Fracture of brittle solids. i. distribution function for fragment size in single fracture (theoretical). *Journal of Applied Physics*, 32(3): 391–399, 1961.

JJ Gilvarry and BH Bergstrom. Fracture of brittle solids. ii. distribution function for fragment size in single fracture (experimental). *Journal of Applied Physics*, 32(3):400–410, 1961.

G. Gisler. Simulation of the eruption of a volatile-rich magma column. *In preparation*, In prep. 2012.

D.E. Grady. Local inertial effects in dynamic fragmentation. *Journal of Applied Physics*, 53(1):322–325, 1982.

D.E. Grady. Particle size statistics in dynamic fragmentation. *Journal of applied physics*, 68(12):6099–6105, 1990.

D.E. Grady. *Fragmentation of rings and shells: the legacy of NF Mott*. Springer Verlag, 2006.

D.E. Grady and M.E. Kipp. Geometric statistics and dynamic fragmentation. *Journal of applied physics*, 58(3):1210–1222, 1985.

U. Grunewald, B. Zimanowski, R. Büttner, LF Phillips, K. Heide, and G. Büchel. MFCI experiments on the influence of NaCl-saturated water on phreatomagmatic explosions. *Journal of Volcanology and Geothermal Research*, 159(1-3):126–137, 2007. ISSN 0377-0273.

K. Hilands. Smooth2.m. *Mathworks*, 2004.

M. Jébrak. Hydrothermal breccias in vein-type ore deposits: A review of mechanisms, morphology and size distribution. *Ore geology reviews*, 12 (3):111–134, 1997.

T. Kadono and M. Arakawa. Crack propagation in thin glass plates caused by high velocity impact. *Physical Review E*, 65(3):035107, 2002.

E. Kaminski and C. Jaupart. The size distribution of pyroclasts and the fragmentation sequence in explosive volcanic eruptions. *Journal of geophysical research*, 103(B12):29759–29, 1998.

CC Lienau. Random fracture of a brittle solid. *Journal of the Franklin Institute*, 221(6):769–787, 1936.

V. Lorenz. Maars and diatremes of phreatomagmatic origin: a review. *Verhandelinge van die Geologiese Vereniging van Suid-Afrika*, 88(2):459–470, 1985.

N.F. Mott. Ministry of supply report no. *AC3642, March*, 1943a.

N.F. Mott. Ministry of supply report no. *AC4035, May*, 1943b.

NF Mott and EH Linfoot. Ministry of supply report no. *AC3348, January*, 1943.

L. Oddershede, P. Dimon, and J. Bohr. Self-organized criticality in fragmenting. *Physical review letters*, 71(19):3107–3110, 1993.

P. Rosin and E. Rammler. The laws governing the fineness of powdered coal. *J. Inst. Fuel*, 7(31):29–36, 1933.

RSJ Sparks, L. Baker, RJ Brown, M. Field, J. Schumacher, G. Stripp, and A. Walters. Dynamical constraints on kimberlite volcanism. *Journal of Volcanology and Geothermal Research*, 155(1-2):18–48, 2006.

H. Svensen, B.U(. Jamtveit, S. Planke, and L. Chevallier. Structure and evolution of hydrothermal vent complexes in the karoo basin, south africa. *Journal of the Geological Society*, 163(4):671, 2006.

DL Turcotte. Fractals and fragmentation. *Journal of Geophysical Research*, 91(B2):1921–1926, 1986.

J.D.N. Winter. *An introduction to igneous and metamorphic petrology*, volume 697. Prentice Hall Upper Saddle River, NJ, 2001.

K. Wohletz and W. Brown. Particulate size distributions and sequential fragmentation/transport theory. *Rapport interne LA-UR*, pages 95–0371, 1995.

KH Wohletz, MF Sheridan, and WK Brown. Particle size distributions and the sequential fragmentation/transport theory applied to volcanic ash. *J. Geophys. Res*, 94(B11):15–703, 1989.

B. Zimanowski, G. Fröhlich, and V. Lorenz. Quantitative experiments on phreatomagmatic explosions. *Journal of Volcanology and Geothermal Research*, 48(3-4):341–358, 1991. ISSN 0377-0273.

B. Zimanowski, R. Büttner, and V. Lorenz. Premixing of magma and water in MFCI experiments. *Bulletin of Volcanology*, 58(6):491–495, 1997a. ISSN 0258-8900.

B. Zimanowski, R. Büttner, V. Lorenz, and H.G. Häfele. Fragmentation of basaltic melt in the course of explosive volcanism. *Journal of Geophysical Research*, 102(B1):803–814, 1997b. ISSN 0148-0227.

B. Zimanowski, K. Wohletz, P. Dellino, and R. Büttner. The volcanic ash problem. *Journal of Volcanology and Geothermal Research*, 122(1-2):1–5, 2003. ISSN 0377-0273.